P-ISSN 2525-2461 • E-ISSN 2615-9937

Vietnam Journal of Science, Technology and Engineering

SEPTEMBER 2020 • VOLUME 62 NUMBER 3

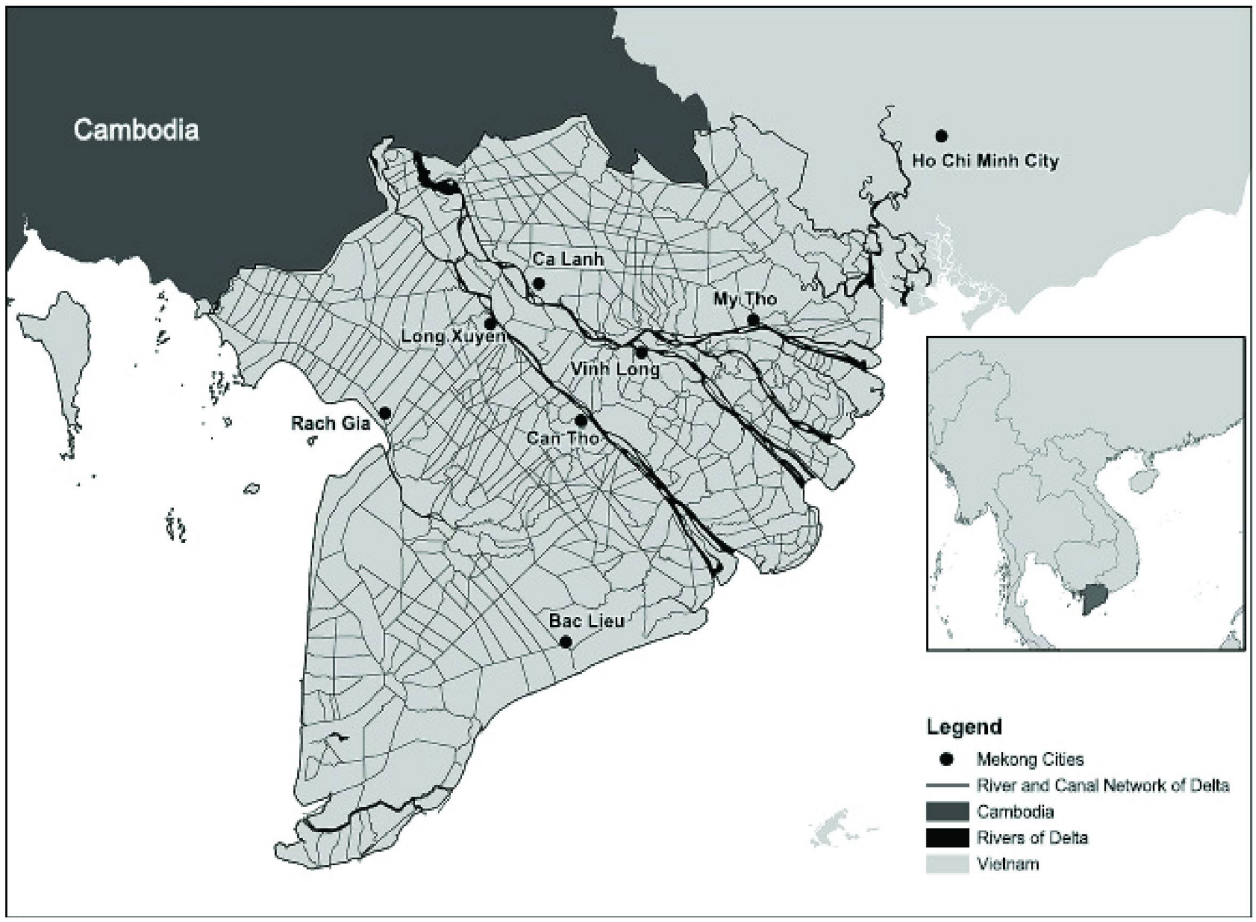

WATER BALANCE FOR AGRICULTURE PRODUCTION IN THE DRY SEASONS OF THE MEKONG RIVER DELTA IN VIETNAM

VIETNAM JOURNAL OF SCIENCE, TECHNOLOGY AND ENGINEERING * SEPTEMBER 2020 * VOLUME 62 NUMBER 3
vietnamscience.vn

Vietnam Journal of Science, Technology and Engineering (VJSTE) **is a quarterly double-blind peer-reviewed academic journal. VJSTE publishes research articles and review articles in all areas of science, technology and engineering with the focus on the life sciences and environmental sciences including the following topics:**

- **Agriculture**
- **Medicine**
- **Pharmacology**
- **Biology**
- **Biotechnology**
- **Ecology**
- **Climatology.**

CLASSIFICATION SCHEME

1. **Mathematics and Computer Science**
   - 1.1. Mathematics
   - 1.2. Computer Science
   - 1.3. Computational Science
2. **Physical Sciences**
   - 2.1. Physics
   - 2.2. Chemistry
   - 2.3. Engineering
3. **Life Sciences**
   - 3.1. Agriculture
   - 3.2. Medicine
   - 3.3. Pharmacology
   - 3.4. Biology
   - 3.5. Biotechnology
4. **Geosciences**
   - 4.1. Geography
   - 4.2. Geology
   - 4.3. Geophysics
   - 4.4. Oceanography
5. **Environmental Sciences**
   - 5.1. Ecology
   - 5.2. Climatology

CONTENTS

SEPTEMBER 2020 • VOLUME 62 NUMBER 3

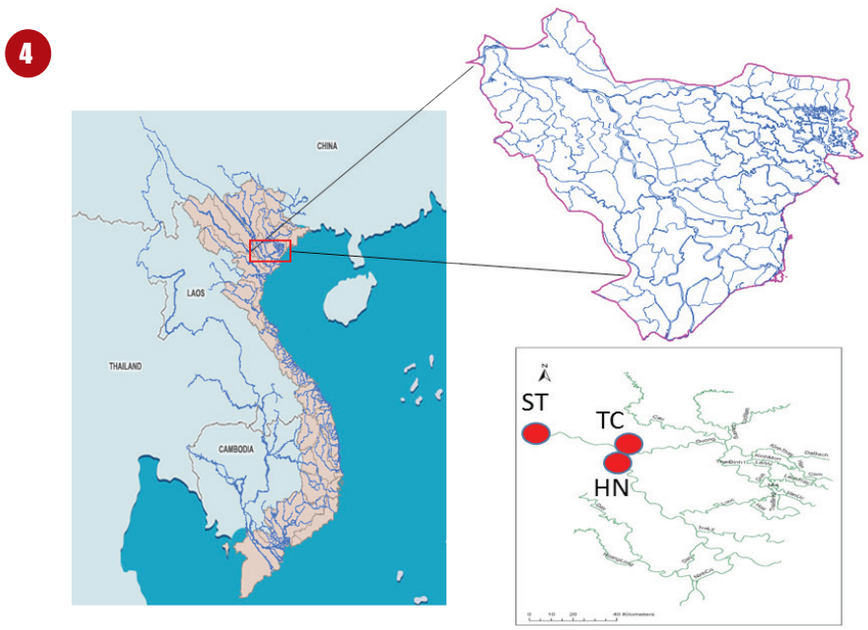

PHYSICAL SCIENCES

CONTENTS

SEPTEMBER 2020 • VOLUME 62 NUMBER 3

39

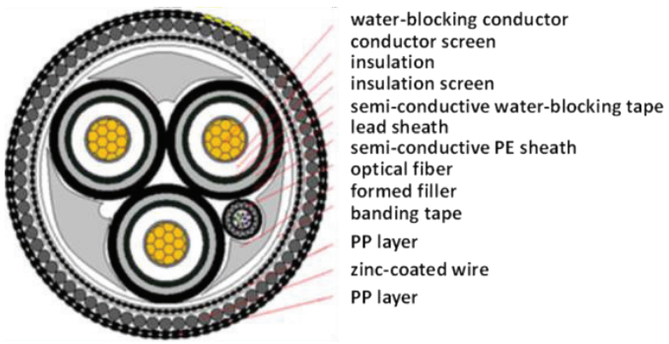

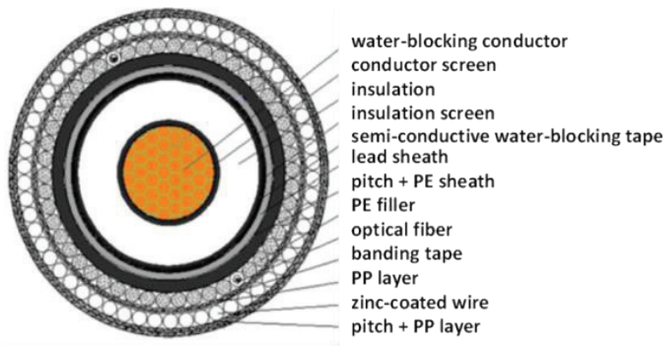

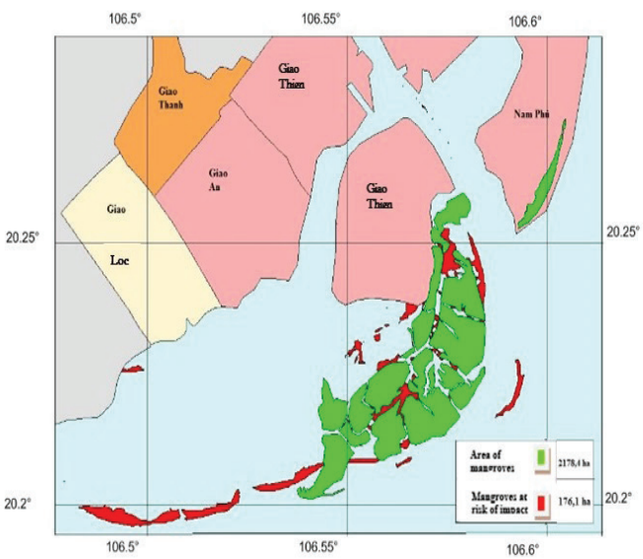

94

Potential use of satellite observations to detect suspended sediment in delta region: a case study of the Red river delta, Vietnam

Hue Thi Dao[1*], Tung Duc Vu[2]

[1]*Thuyloi University*

[2]*Vietnam Disaster Management Authority, Ministry of Agriculture and Rural Development, Vietnam*

Received 4 December 2019; accepted 2 April 2020

Abstract:

Building an integrated river delta basin and coastal management plan in the context of climate change requires suspended sediments data, which plays an important role and is the key component for understanding the hydrology regime in the delta region. Sediments are responsible for carrying a considerable amount of nutrients and contaminants. Most sediment discharge data is acquired by surveys/ data collection activities or by mathematical modelling. However, these methods are costly, time-consuming, and complex. Therefore, in this study, the authors investigate the potential use of satellite observations (MODIS reflectance) to detect suspended sediment flux in the Red river delta (RRD) of Vietnam. The relationships between discharge (Q), suspended sediment concentration (SSC), and total load (L) collected from the three in-situ stations Son Tay station (ST), Thuong Cat station (TC), and Hanoi station (HN) in the RRD are determined by regression analyses of reflectance data (R) obtained from MODIS bands 1-2 (250-m resolution). The results present a close connection between the monthly average of SSC and R and a good statistical relationship between the monthly average of Q and R in HN. At TC and ST, a lower correlation was found compared to HN because of the cloud cover and the position where data was collection in the river. The coefficient of determination ranged from 0.11 to 0.40 for the R-SSC and R-Q relationships. A method of estimating SSC and L at a single point along the river using data from Q and R was proposed based on the relationship correlation results.

Keywords: **delta region, discharge, MODIS, regression analysis, suspended sediment.**

Classification numbers: **2.1, 5.1**

Introduction

Suspended sediment, which includes organic and inorganic materials within the water flow, is a natural part of a river system. The primary sources of suspended sediment come from the erosion of soil, mass movements such as landslides, and riverbank erosion or human interventions on the landscape [1-3]. High amounts of suspended sediment in water can reduce the transmission of light, which not only affects the phytoplankton species in short term but also the entire ecosystem in the long term. Suspended sediment plays an important role in shaping the landscape, transporting nutrients to various species, and creating ecological habitats [4, 5]. Similarly, pollutants can adhere to suspended sediment while in transport and thus suspended sediment can influence pollutant movement. Suspended sediment is also an indicator of issues occurring in the river delta and coastal areas, which include water quality, ecological degradation, and soil and/or riverbank erosion. To develop a suitable river basin management strategy, frequent monitoring of suspended sediment is critical.

Despite the importance of suspended sediment, it is poorly gauged due to the lack of in-situ networks in many areas and especially in developing countries. We choose the RRD for this research because this region has several meteorological stations. However, they have not been operated for some time due to lack of budget and thus this region is considered to be ungauged basin. Moreover, the RRD is one of two largest and most important deltas in Vietnam; however, it has not received as much attention as the Mekong river delta. Thus, research in this area is central to the critical understanding of this important region.

Data quality is also a concern since monitoring suspended sediment depends on the number of stations, their locations, and the frequency of measurements [6]. There are some

*Corresponding author: Email: hue.dao89@gmail.com

methods to obtain suspended sediment information such as using empirical models, physically-based mathematical models, and field sampling. Recently, the use of satellite images to detect suspended sediment has captured the attention of researchers [7-9]. There are studies that use Moderate Resolution Imaging Spectroradiometer (MODIS) images or Landsat Thematic Mapper (TM) and Enhanced Thematic Mapper Plus (ETM+) imagery to characterize the spatial and temporal pattern of surface sediments [10-13] based on the very close relationship between R and suspended sediment concentration. Recent results show that satellite remote sensing technology is applicable and useful to obtain not only suspended sediment information but also other hydrological parameters of these ungauged areas [14].

This study aims to investigate the potential use of satellite observations (MODIS reflectance) to detect the seasonal change of suspended sediment flux in the RRD region. We first extract the satellite reflectance value at the location of the station and then apply simple regression analysis to the reflectance, discharge, suspended sediment, and total sediment load on the same day. The simple regression analysis used in this paper refers to the use of single variable (R) for one dependent variable (suspended sediment or discharge). We choose the simple regression analysis because of limitations in the available data and the objective of our research. Regression analysis performance is examined by the coefficient of determination. Only one band of reflection data was used to access the relationship with other hydrological factors. In future research, multi-band reflection data will be used to provide better results by using multi-regression analysis.

Materials and methods

Study area

The RRD is one of the largest deltas in Vietnam, the fourth largest delta in Southeast Asia in terms of delta plain size, and is also one of the chief deltas in Asia. The RRD lies in the northern part of Vietnam with a total delta area of 15000 km^2. The delta includes two large river systems: the Red river and Thai Binh river systems. The discharge in Red river is 120 km^3 of water annually and 130×10^6 ton/year of mean annual suspended sediment load. During the wet season from June to January, about 90% of the annual sediment supply is transported from a large number of distributaries. About 11.7% of the total amount of sediment goes through the Van Uc and Thai Binh river mouths, 37.8% passes through the Ba Lat mouth [15], 23.7% through the Day river mouth, and the remaining amount of sediment passes through the Tra Ly river mouth.

The climate in RRD is sub-tropical and formed by a summer monsoon from the South and a winter monsoon from the North-East. The two wet seasons account for 85-95% of the total rainfall per year [16]. The mean annual rainfall was 1590 mm and mean annual potential evapotranspiration ranged from 880 to 1150 mm per year [17].

To explore the relationship between Q-SSC, R-Q, R-SSC, and L-Q, three locations in this delta were taken into account, namely, ST, TC, and HN. ST is located upstream of the Red river and TC and HN are located at the Duong river and Red river, respectively, as shown in Fig. 1.

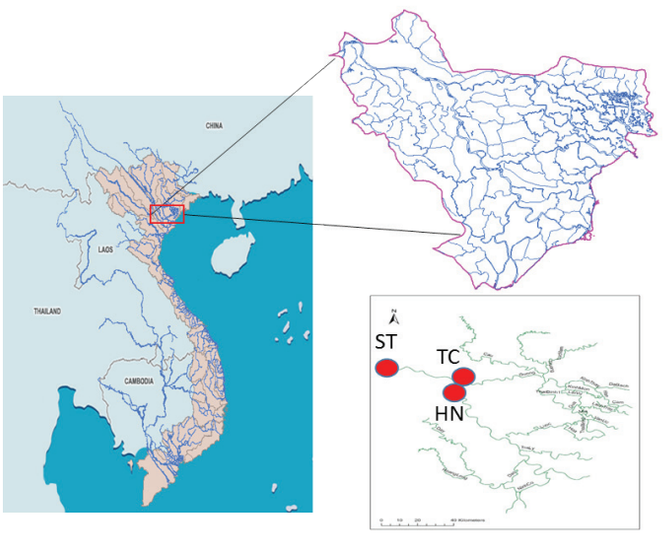

Fig. 1. Study area and location of the three stations.

Data

Table 1. Location, date, and sources of data in 3 stations in RRD.

Station	Longitude	Latitude	Data product	Date (month-day-year)	Source
ST	21.15	105.50	Daily discharge	1/1/2012-12/31/2013	VAWR
			Daily suspended sediment	1/1/2012-12/31/2013	VAWR
			Daily MODIS band 1	1/1/2012-12/31/2013 (182 scenes)	LP DAAC
TC	21.06	105.86	Daily discharge	1/1/2012-12/31/2013	VAWR
			Daily suspended sediment	1/1/2012-12/31/2013	VAWR
			Daily MODIS band 1	1/1/2012-12/31/2013 (171 scenes)	LP DAAC
HN	21.01	105.85	Daily discharge	1/1/2012-12/31/2013	VAWR
			Daily suspended sediment	1/1/2012-12/31/2013	VAWR
			Daily MODIS band 1	1/1/2012-12/31/2013 (171 scenes)	LP DAAC

Table 1 shows the location, date, and sources of all data from the three stations used in this study. The daily discharge and daily suspended sediment concentration data from the three stations were obtained from the Vietnam Academy for Water Resources (VAWR) over the course of two years: 2012 and 2013. Basically, they are measured in the middle of the river at 0.5 m, 1 m, and 3 m from the water's surface then the average values are taken. Moreover, one specific objective is to explore the relationship between R and other hydrological factors that do not depend on time, thus the period of 2012-2013 is suitable for this study. On the other hand, the reflectance data was extracted from MODIS Surface Reflectance (code: MOD09). In general, MOD09 is a seven-band product computed from MODIS level 1B land bands 1 (620-670 nm), 2 (841-876 nm), 3 (459-479 nm), 4 (545-565 nm), 5 (1230-1250 nm), 6 (1628-1652 nm), and 7 (2105-2155 nm). Most satellite data processing systems recognise five distinct levels of processing. Level 0 data is raw satellite feeds. Level 1 data has been radiometrically calibrated but not otherwise altered. Level 2 data is level 1 data that has been atmospherically corrected to yield a surface reflectance product. Level 3 data is level 2 data that has been gridded into a map projection and usually has also been temporally composited or averaged. Finally, level 4 data are products that have been put through additional processing. Due to the available data and the objective of our research, the images from MODIS Terra band 1 (620-670 nm, 250-m resolution and Surface Reflectance daily level 2 global (MOD09GQ)) is downloaded from USGS freely, then this data was input and extracted by ArcGIS software for retrieval of R from the pixel of the station's location. In this study, only the reflectance on a cloud-free day with less than 0.2 cloud fraction are acquired at the observation point of the gauged station and used for regression analysis. In total, 167 Terra MODIS images were acquired over two years for assessing the reflectance in TC and 171 images and 182 images were downloaded to use for HN and ST, respectively, from the beginning of 2012 to the end of 2013.

Methods

To estimate the possible relationship between Q-SSC, R-SSC, R-Q, and L-Q, we apply the single regression analysis to the reflectance values, observed Q, and observed SSC on the same day the MODIS images were taken. The total sediment load is calculated by the multiplication of Q and SSC as shown in Eq. (1):

$$L=Q*SSC \quad (1)$$

The performance of the regression model was checked by the coefficient of determination.

Results and discussion

Time series analysis of Q, SSC, L and R

The temporal change in Q, SSC, and L are described in Figs. 2, 3, and 4. In general, the trends of Q and SSC during the time are similar to all stations, that is, increasing during the first half of the year and decreasing during the remaining time. From Fig. 2, because ST is positioned upstream, Q in ST is equal to the sum of Q in TC and HN due to water balance of the river system. In addition, Q at all 3 stations had a similar pattern; increasing from the beginning of the year and reaching a peak of about 9000 m^3/s in September, then a decrease to just over 1000 m^3/s until the end of the year.

From Fig. 3, each station had a different temporal pattern of SSC change. The SSC in TC was highest compared to other stations although it is located in the distributary and ST is in the upstream of the river network system.

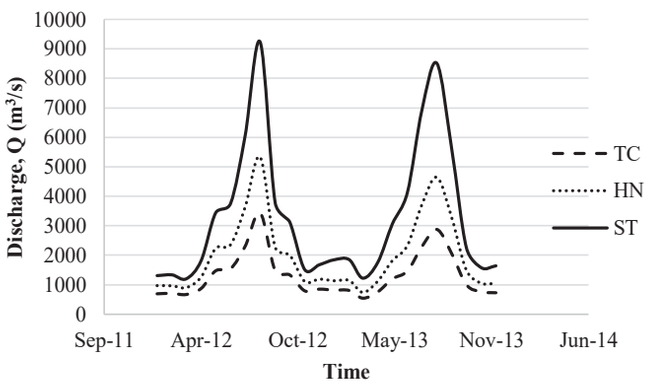

Fig. 2. Temporal change in discharge, Q, at the three stations TC, HN, and ST.

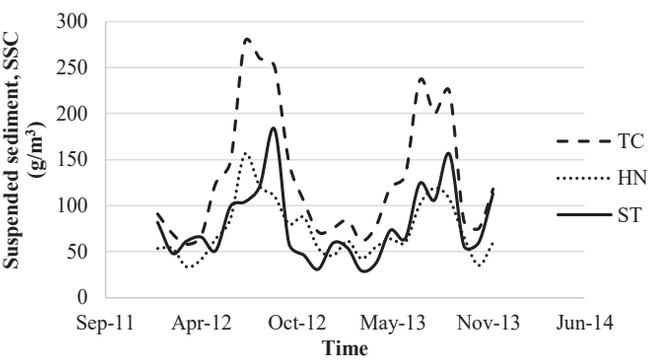

Fig. 3. Temporal change in suspended sediment, SSC, at the three stations TC, HN, and ST.

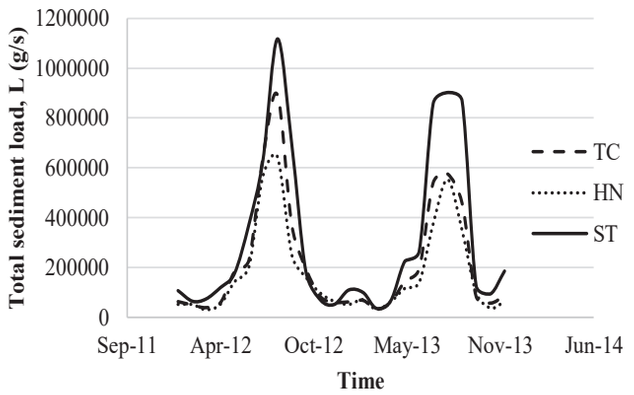

Fig. 4. Temporal change in total load, L, at the three stations TC, HN, and ST.

As shown in Eq. (1), the total load, L, (Fig. 4) is the product of discharge, Q, (Fig. 2) and suspended sediment, SSC (Fig. 3). The discharge at TC, on average, makes up approximately 45% of Q at ST. However, the total load, L, at TC is about 78% of L at ST during 2012 due to a dramatic increase in SSC at TC (Fig. 3). It is noted that SSC does not follow the balance term because of bank erosion or landslides along the river. However, the total sediment load seems to satisfy the general principle of mass balance: L at ST is equal to the sum of L at TC and L at HN. Moreover, the load of suspended sediment was higher in the rainy season than in the dry season.

Regression analysis

Due to the effects of clouds on the reflectance value, we eliminated several points at each station for a total of 24 data points over 2 years for monthly regression analysis. Fig. 5 through Fig. 8 show scatter plots of the relationships between L-Q, Q-SSC, R-Q, and R-SSC. The results of the relationship equations and performances of the regression analyses are represented in Table 2. The best fit results for all the relationships in our study followed a power function.

From Table 2, a significant overall relationship between total load, L, and discharge, Q, was observed with a high value of R^2 that was greater than 0.8 at all stations. The fit parameters of the three fit equations, in this case, were also similar. For example, the scaling factor and exponent parameters ranged from 0.23 to 1.26 and 1.49 to 1.86, respectively. Thus, in future studies, the relationship between L and Q can be defined by a single equation for the three stations.

The fit results also showed a very close connection between Q and SSC at the TC station while HN and ST had a lower performance regression compared to TC. However, the scaling factors found from the three relationship equations were very different from each other with the smallest value of 19.87 and largest value of 116.53 due to a wide range of both Q and SSC at each location (see Figs. 2 and 3). In contrast, there was only a slight difference in the value of the exponent in the relationship equation of Q-SSC.

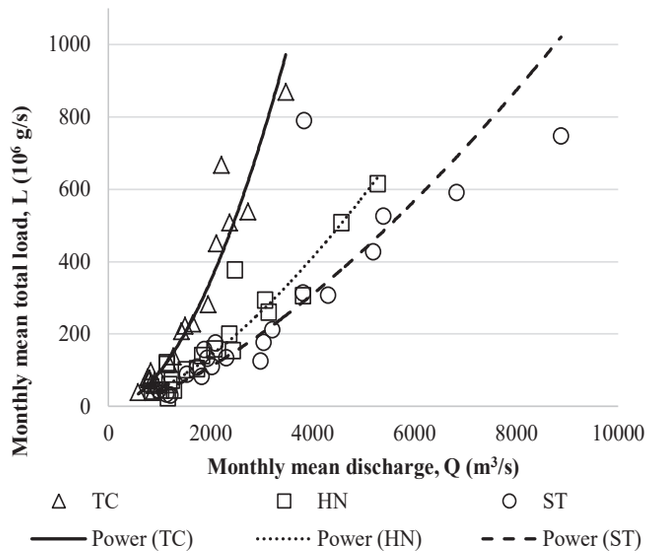

Fig. 5. Scatter plots of monthly mean total load, L, and monthly mean discharge, Q, at the three stations TC, HN, and ST.

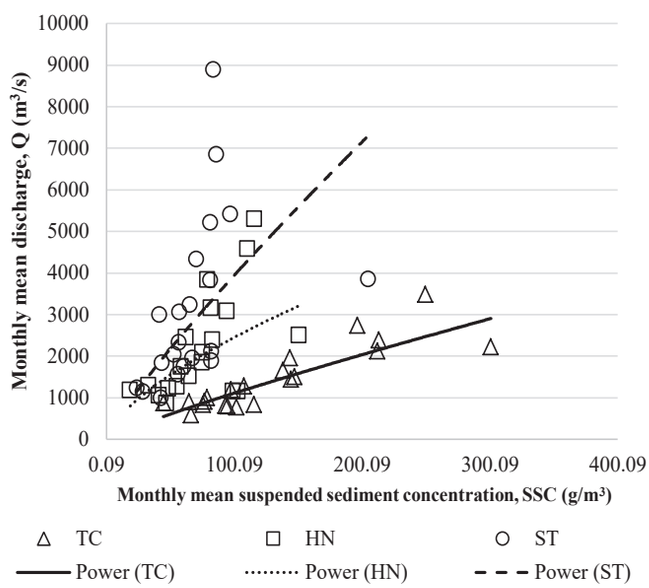

Fig. 6. Scatter plots of monthly mean discharge, Q, and monthly mean suspended sediment concentration, SSC, at the three stations TC, HN, and ST.

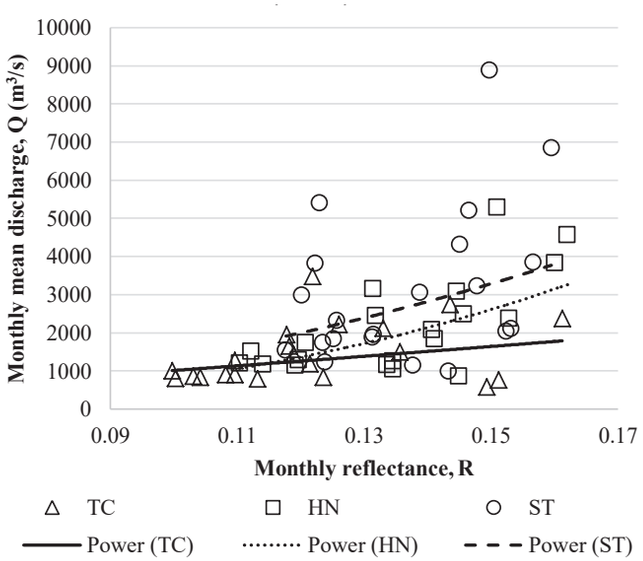

Fig. 7. Scatter plots of monthly reflectance, R, and monthly mean discharge, Q, at the three stations TC, HN, and ST.

A close relationship between R-Q and R-SSC were recorded at the HN station. The R^2 value was 0.40 and 0.33 for R-Q and R-SSC, respectively, for this station. However, TC and ST had smaller correlation results than HN. An interesting point in these results is that using the reflectance value to predict SSC is better than predicting Q by R. Both the scaling factors and exponents in the R-SSC equations were not much different for the three stations, but they did vary significantly in case of the R-Q relationship equations. The R-SSC relationship (see Fig. 8) displayed a similar trend for all stations, but there were more outlier points in TC than in HN and ST.

One possible reason to explain the outlier points is the effect of clouds. The cloud cover is different at each station and it influences the reflectance value of the pixel where the observation data was taken.

Inter-relationship between regression parameters

As shown in Figs. 5, 6, and 7, the relationship of L-Q, R-SSC, and R-Q can be expressed as

$$L=aQ^b \quad (2)$$

$$SSC=\alpha R^\beta \quad (3)$$

$$Q=\gamma R^\delta \quad (4)$$

Substituting Eq. (2) and Eq. (3) into Eq. (1) reveals

$$aQ^b = Q*\alpha R^\beta \quad (5)$$

Then,

$$Q = \left(\frac{\alpha}{a}\right)^{\frac{1}{b-1}} R^{\frac{\beta}{b-1}} \quad (6)$$

Comparing Eq. (6) with Eq. (4) gives

$$\gamma = \left(\frac{\alpha}{a}\right)^{\frac{1}{b-1}} \quad (7)$$

and

$$\delta = \frac{\beta}{b-1} \quad (8)$$

Depending on Eq. (7) and Eq. (8), it is possible to estimate the parameters for one of the three equations (Eq. (2) Eq. (3), or Eq. (4)) from the parameters of the other equations. For example, if we observed Q at a specific point of river section, we can correlate Q with satellite-observed R and then γ and δ parameter in Eq. (4) could be obtained. In addition, the parameters a and b could be possibly estimated from hydro-geological characteristics and land cover in the upstream area using a regionalization scheme [18]. Once the parameters γ, δ, a, and b are identified through the above procedure, α and β in Eq. (3) can be obtained from Eqs. (7) and (8) without using observed SSC data. Then, Eq. (3) could be applied for near-real-time SSC monitoring using satellite observed water-surface reflectance, R, and identified parameters α and β.

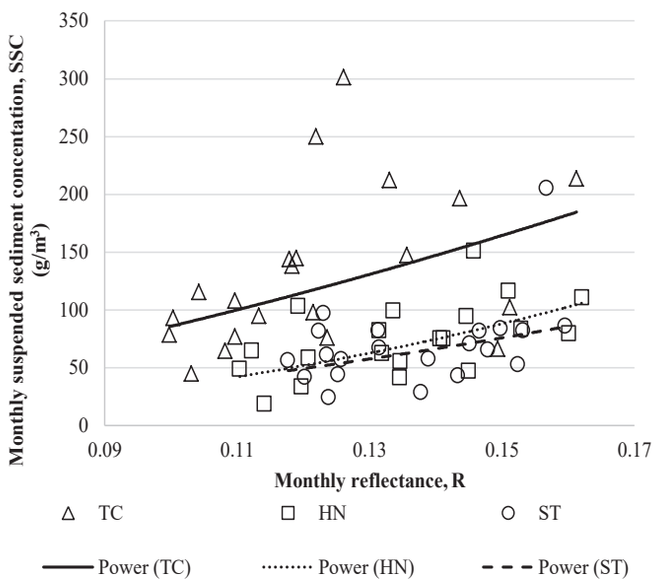

Fig. 8. Scatter plots of the monthly mean suspended sediment concentration, SSC, and monthly reflectance, R, at the three stations TC, HN, and ST.

Table 2. Relationship equation and performance of regression of L-Q, Q-SSC, R-Q, R-SSC at the three stations.

Correlation	Station	Relationship equation	R^2
L-Q	TC	$L=0.23Q^{1.86}$	0.94
	HN	$L=1.03Q^{1.55}$	0.82
	ST	$L=1.26Q^{1.49}$	0.87
Q-SSC	TC	$Q=19.87SSC^{0.87}$	0.76
	HN	$Q=116.53SSC^{0.66}$	0.37
	ST	$Q=75.42SSC^{0.86}$	0.43
R-Q	TC	$Q=1575R^{1.19}$	0.11
	HN	$Q=64678R^{2.90}$	0.40
	ST	$Q=22716R^{2.23}$	0.13
R-SSC	TC	$SSC=3427.1R^{1.60}$	0.21
	HN	$Q=7926.8R^{2.38}$	0.33
	ST	$Q=2927R^{1.92}$	0.18

Conclusions

This study explored the possibility of detecting a seasonal change of suspended sediment flux by using remotely sensed reflectance of MODIS imagery. At first, we extracted R from MODIS (band 1, 250-m resolution, Surface Daily L2G Global) and then analysed the relationship between R-SSC and R-Q. We also estimated the relationship between L-Q and Q-SSC.

The results indicate a significant relationship in L-Q and Q-SSC and a possible connection in R-SSC and R-Q. Although there were some error sources that affected the accuracy of the suspended sediment and discharge estimation, the results showed a potential of using MODIS satellite reflectance to detect SSC in the delta region. A set of equations that calculate the sediment depending on Q and R was built in this study. This set has a potential for application in other study areas where the change in Q and R corresponds to the characteristics of each area.

The approach introduced here illustrates the possible use of satellite images and the information of Q in SSC monitoring in a data-poor basin. One limitation in this study is using only R extracted from satellites, which cannot exactly detect the value of suspended sediment without Q data. However, a combination of other satellite observations such as the EOMAP (Earth Observation and Environmental Services) water quality monitoring services and R from MODIS images can solve the problem of monitoring suspended sediment in ungauged river basins in future research. Moreover, using hydrological results obtained from remote sensing can be used in combination with a numerical model for a deeper understanding about the basin.

ACKNOWLEDGEMENTS

The authors would like to acknowledge the University of Yamanashi, Ministry of Education, Culture, Sports, Science and Technology, Japan (MEXT) for supporting this study; and Vietnam Academy for Water Resources (VAWR), Ministry of Agriculture and Rural Development (MARD) for providing data and information.

The authors declare that there is no conflict of interest regarding the publication of this article.

REFERENCES

[1] K. Fryirs (2013), "(Dis) Connectivity in catchment sediment cascades: a fresh look at the sediment delivery problem", *Earth Surf. Process. Landf.*, **38(1)**, pp.30-46, DOI: 10.1002/esp.3242.

[2] R.P.C Morgan (2005), "Soil Erosion & conservation", *European Journal of Soil Science*, **56**, pp.681-687, DOI: 10.1111/j.1365-2389.2005.0756f.x.

[3] V. Kim, R.C. Grabowski, R.J. Rickson (2017), "Suspended sediment transport dynamic in rivers: multi scale drivers of temporal variation", *Earth-Science Reviews*, **166**, pp.38-52, DOI: 10.1016/j.earscirev.2016.12.016.

[4] D.J. Dean, D.J. Topping, J.C. Schmidt, R.E. Griffiths, T.A. Sabol (2016), "Sediment supply versus local hydraulic controls on sediment transport and storage in a river with large sediment loads", *J. Geophys. Res. Earth Surf.*, **121(1)**, pp.110-182, DOI: 10.1002/2015JF003436.

[5] A.J. Koiter, P.N. Owens, E.L. Petticrew, D.A. Lobb (2013), "The behavioural characteristics of sediment properties and their implications for sediment fingerprinting as an approach for identifying sediment sources in river basins", *Earth-Science Reviews*, **125**, pp.24-42, DOI: 10.1016/j.earscirev.2013.05.009.

[6] E. Robert, M. Grippa, L. Kergoat, S. Pinet, L. Gal, G. Cochonneau, J.M. Martinez (2016), "Monitoring water turbidity and surface suspended sediment concentration of the Bagre reservoir (Burkina Faso) using MODIS and field reflectance data", *International Journal of Applied Earth Observation and Geoinformation*, **52**, pp.243-251, DOI: 10.1016/j.jag.2016.06.016.

[7] R.L. Miller, B.A. McKee (2004), "Using MODIS terra 250 m imagery to map concentration of total suspended matter in coastal waters", *Remote Sensing of Environment*, **93**, pp.259-266.

[8] Z. Chen, C. Hu, K.F. Muler (2007), "Monitoring turbidity in Tampa bay using MODIS/Aqua 250-m imagery", *Remote Sensing of Environment*, **109**, pp.207-220.

[9] A.I. Dogliotti, K.G. Ruddick, B. Nechad, D. Doxaran, E. Knaeps (2015), "A single algorithm to retrieve turbidity from remotely-sensed data in all coastal and estuarine waters", *Remote Sensing of Environment*, **156**, pp.157-168.

[10] N.E. Kilham, D. Roberts (2011), "Amazon river time series of surface sediment concentration from MODIS", *International Journal of Remote Sensing*, **32(10)**, pp.2659-2679, DOI: 10.1080/01431161003713044.

[11] J.E. Min, J.H. Ryu, S. Lee, S. Son (2012), "Monitoring of suspended sediment variation using Landsat and MODIS in the Saemangeum coastal area of Korea", *Marine Pollution Bulletin*, **64(2)**, pp.382-390, DOI: 10.1016/j.marpolbul.2011.10.025.

[12] E. Park, E.M. Latrubesse (2014), "Modelling suspended sediment distribution patterns of the Amazon river using MODIS data", *Remote Sensing of Environment*, **147**, pp.232-242, DOI: 10.1016/j.rse.2014.03.013.

[13] M. Zhang, Q. Dong, T. Cui, C. Xue, S. Zhang (2014), "Suspended sediment monitoring and assessment for Yellow river estuary from Landsat TM and ETM+ imagery", *Remote Sensing of Environment*, **146**, pp.136-147, DOI: 10.1016/j.rse.2013.09.033.

[14] K. Hashimoto, K. Oki (2013), "Estimation of discharges at river mouth with MODIS image", *International Journal of Applied Earth Observation and Geoinformation*, **21**, pp.276-281, DOI: 10.1016/j.jag.2012.06.008.

[15] J.D. Milliman, C. Rutkowski, M. Meybeck (1995), *River Discharge to the Sea: a Global River Index*, LOICZ Core Project Office, Texel, Netherlands, DOI: 10.13140/RG.2.1.2119.8565.

[16] V.D. Vinh, S. Ouillon, T.D. Thanh, L.V. Chu (2014), "Impact of the Hoa Binh dam (Vietnam) on water and sediment budgets in the Red river basin and delta", *Hydrology and Earth System Sciences*, **18(10)**, pp.3987-4005, DOI: 10.5194/hess-18-3987-2014.

[17] T.P.Q. Le, J.A. Garnier, G. Billen, S. Thery, V.M. Chau (2007), "The changing flow regime and sediment load of the Red river, Viet Nam", *Journal of Hydrology*, **334(1)**, pp.199-214, DOI: 10.1016/j.jhydrol.2006.10.020.

[18] S. Heng, T. Suetsugi (2015), "Regionalization of sediment rating curve for sediment yield prediction in ungauged catchments", *Hydrology Research*, **46(1)**, pp.26-38, DOI:10.2166/nh.2013.090.

DOI: 10.31276/VJSTE.62(3).10-14

Development of a device based on the respirometric principle for long-term monitoring of BOD and pH: a novel approach in wastewater characterisation

Thanh Dam Nguyen[1], My Linh Hoang[1], Hong Anh Duong[1], Hung Viet Pham[1*], Anh Tuan Do[2], Jean-Luc Vasel[3]

[1]Key Laboratory of Analytical Technology for Environmental Quality and Food Safety Control, University of Science, Vietnam National University, Hanoi, Vietnam

[2]Institute of Information Technology Vietnam Academy of Science & Technology, Vietnam

[3]EcoService Company, Libramont, Belgium

Received 3 February 2020; accepted 31 March 2020

Abstract:

Biochemical oxygen demand (BOD) and pH are two important parameters in environmental analysis that allow the assessment of water quality. Although the long-term determination of BOD and pH can provide more useful information about the wastewater characteristics, present commercial BOD devices do not usually meet this demand. This research has successfully developed a novel BOD/pH device based on the respirometric principle, which can simultaneously and continuously monitor both BOD and pH of wastewater for about 20 days. The performance of the proposed device is evaluated in the laboratory by comparison to that of a commercial device (BOD Trak II, HACH). This solution not only follows the variation of BOD and pH over a long period of time, but also shows low cost and high potential for a wide variety of applications in Vietnam.

Keywords: **BOD, characterization, pH, respirometric, wastewater.**

Classification number: **2.2**

Introduction

BOD and pH are important parameters that assess water quality [1]. BOD tests can be considered as a miniature aerobic biological treatment process, in which microorganisms use organic compounds for food while consuming oxygen and producing CO_2 and H_2O [2]. Those metabolic reactions induce pH changes. While pH changes can be easily followed by a pH meter, BOD curves, which tally the cumulated oxygen consumption, is a complicated and time-consuming process that usually takes five days for a BOD_5 test.

In recent years, some studies have developed different methods to rapidly measure BOD [3, 4], however, long-term monitoring of BOD can bring interesting results about the kinetics of biodegradation [5, 6] and even odour [7]. Current commercial BOD measuring devices can be classified into two major categories: (1) the measurement of dissolved oxygen (DO) consumption in the liquid phase by an optical/DO sensor and (2) the determination of O_2 consumption in the gas phase by monitoring pressure depletion with a pressure sensor (manometry or respirometry) [8]. The biodegradation process takes place in the liquid phase, so the first type of BOD device may seem more favourable. However, the measurement of oxygen in the liquid phase is not suitable for long-term BOD monitoring because the electrodes consume a small amount of oxygen and that will cause compound errors if measured continuously. For this reason, the respirometric method is the preferred option for the purpose of long-term BOD measurement.

[*]Corresponding author: Email: phamhungviet@hus.edu.vn

The combination of BOD and pH data with mathematical models can be a novel approach to the characterization of wastewater for simulating and optimizing the treatment process. However, the requirement of continuous BOD and pH data (sampling frequency can be every 5 minutes) for a long time (about 20 days) is not met by current equipment. Therefore, in this study, a novel device has been developed based on the respirometric principle that is capable of simultaneous and continuous measurement of both BOD and pH.

Materials and methods

Chemicals and materials

To absorb CO_2 in all tests, solid KOH (Merck, Germany) was used. Besides, the pH buffers (4.01, 7.00, and 10.01 from HACH, USA) were used to calibrate the pH sensor of the device.

The BOD Trak II device (HACH, USA) was used as a reference to make the comparison between the developed BOD/pH device and the commercial BOD equipment.

The samples used in the test of the proposed BOD/pH device and BOD Trak II were real wastewater samples collected from a pig farm in Hanoi. The samples were taken in glass bottles at the location of the waste gate and then stored at 4°C before analysis.

Instrumentation

The development process of the BOD/pH device included defining its features, selecting its components, designing electronic circuits, assembling the equipment, and finally calibrating the device before applying it in practice. The electronic components that were used to build the device include a microcontroller (STMicroelectronics, USA), pressure sensors (TE connectivity, Switzerland), pH sensors (Rika, Taiwan), temperature sensors (Sensirion AG, Switzerland), an 8×2 LCD display screen (Newhaven Display Intl, USA), 64 KB ROM storage memory (Adesto Technologies, USA), and a 12 VDC power supply unit.

The principal circuit of the components used in the BOD/pH device were designed on OrCAD software. The printed circuit board (PCB) to connect the components was designed with PADS2015 software. After assembly, the device was calibrated by measuring the signal of the standard values for pressure and pH, establishing a calibration curve and feeding the microcontroller.

Software

Software was developed for graphical displays, BOD calculation, online data acquisition, and other calculations. The BOD data logger software, which was developed in C#, has two main parts:

(A) In the first part (tab Setup), the users provide parameters like information COM port (name, baud rate, etc.), sample description (volume of bottle, volume of liquid phase, range of BOD), maximum time for taking readings, time interval between readings, and output file name to the software. This form has four command buttons i.e. Open, Close, Start, and Exit. By pressing the Open button, the program opens the COM port that connects to the device through a USB interface. By pressing the Start button, the program starts acquiring data from the device.

(B) The second part (tab BOD data) provides users with the values of the date and time, pressure, temperature, pH, as well as BOD value. All these data are saved in the file that the users assign in the first part.

BOD and pH monitoring

To confirm the operation of the device in practice, BOD and pH data of wastewater samples were monitored by both BOD/pH and BOD Trak II devices. In the experiment, the sample was diluted 5 times (BOD after dilution in the range of 0-350 mg/l) with deionized water. BOD values were continuously monitored for 20 days on the BOD/pH device and 10 days on BOD Trak II device (10 days is the maximum period of measurement on this device) with the frequency of 3 measuring points/hour. On the BOD/pH device, the pH values were recorded with the same frequency. The obtained results were processed in Microsoft Excel.

Result and discussion

System design and operation

The principal circuits for the components of the BOD/pH device were designed by OrCAD software, including the ports of supply, algorithm amplifier (if needed), and the connection to the microcontroller. The PCB circuit was designed on PADS2015 to ensure the components are arranged harmoniously, the connection signals are not overlapping, and to reduce noise. The principal circuit of the pressure sensor, pH sensor, and PCB is shown in Fig. 1.

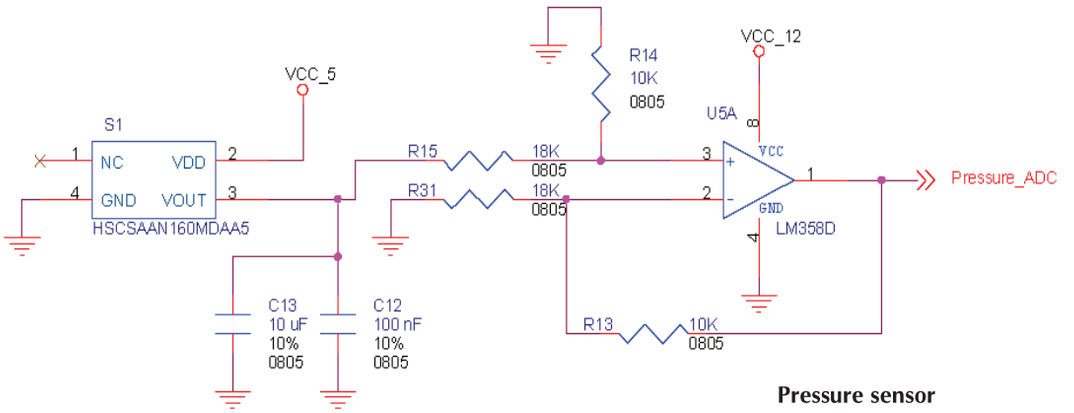

(A)

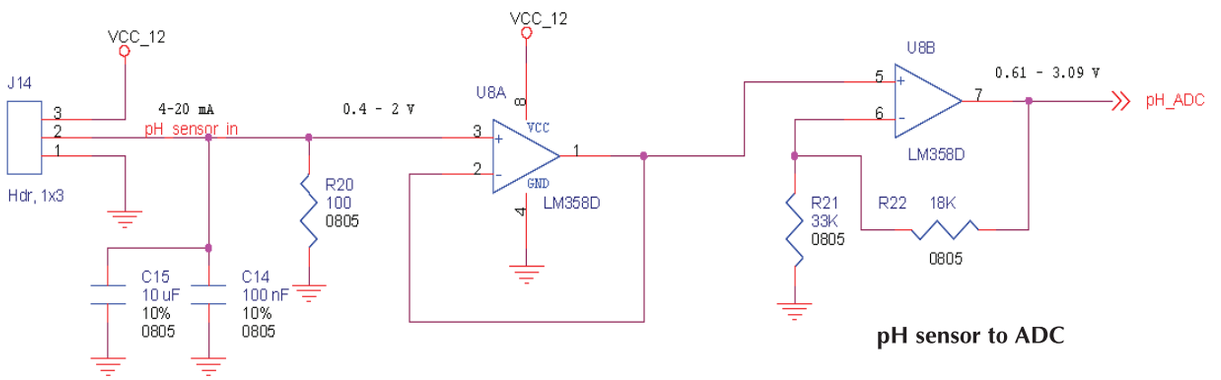

(B)

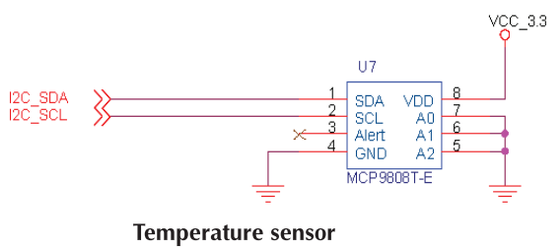

(C)

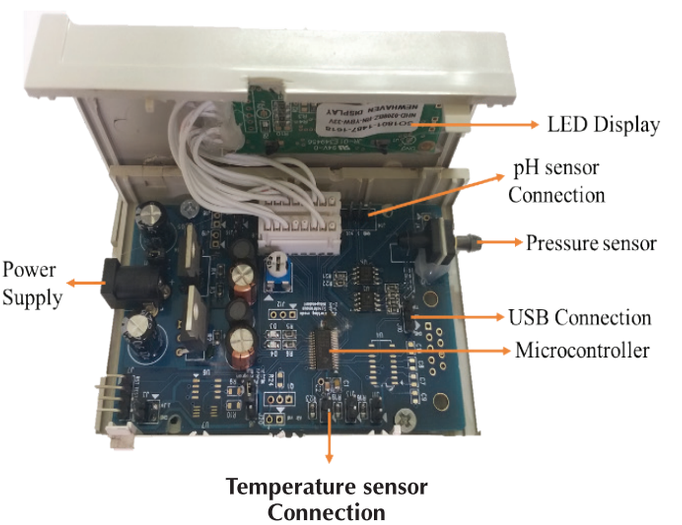

(D)

Fig. 1. Design of principal circuit and PCB of BOD/pH device. (**A**) Circuit for the current power supply and amplifier of the pressure sensor; (**B**) Receiving circuit for the pH sensor; (**C**) Circuit to connect temperature sensor; and (**D**) Electronic circuit of the BOD/pH device.

The cap of the bottle was specially designed by lathing a Teflon block to ensure that it can fit to other components in the device and remain airtight. Fig. 2 shows the 3D design and real photos of the cap.

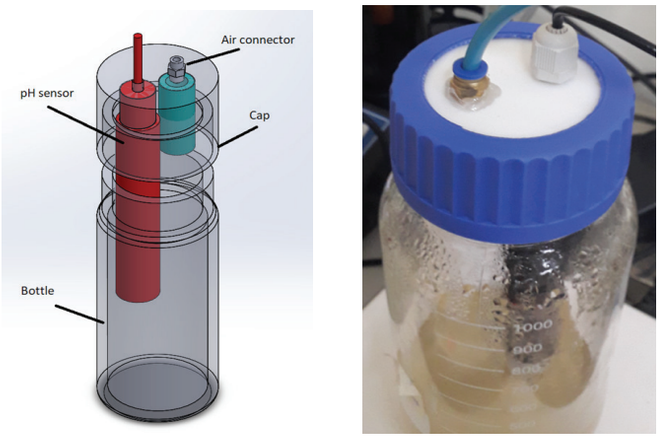

Fig. 2. 3D design and photo of the bottle in BOD/pH device.

After fabrication, the BOD/pH device is calibrated by obtaining the linear equation between the measured signal (the values from the analog-to-digital converters i.e. ADC) and the pressure as well as pH values (Figs. 3 and 4). The results show that there are good linear correlations between the signal obtained from the sensors and the values of BOD and pH as the correlation coefficients of the two calibration curves are both 0.9999.

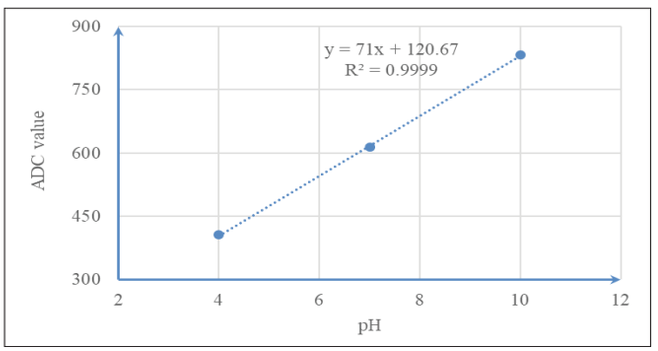

Fig. 3. Calibration curve of pH measured by BOD/pH device.

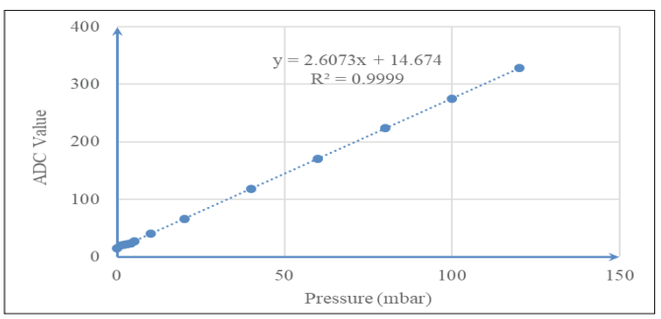

Fig. 4. Calibration curve of pressure measured by BOD/pH device.

BOD and pH monitoring

After calibrating the device and building the data logger software, the BOD/pH device was applied to continuously monitor the BOD and pH in a wastewater sample collected from a pig farm. The results obtained on the BOD/pH device and the BOD Trak II device are shown in Fig. 5.

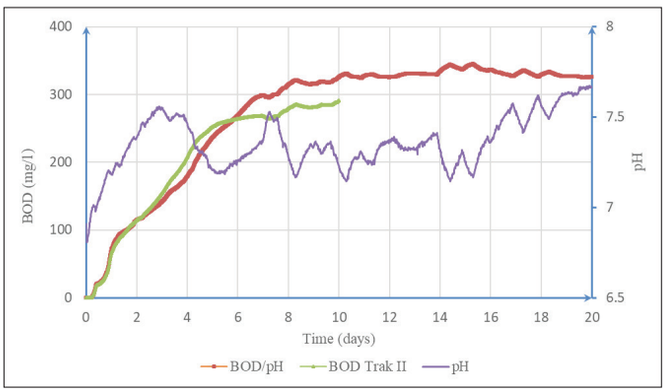

Fig. 5. Comparing results between the prototype BOD/pH device and commercial device (BOD Trak II, HACH).

The results show that the BOD/pH device has good reliability as the BOD values obtained between this device and the commercial device are almost identical during the test and the errors do not exceed 15% during the measurement period. Besides, it can be seen that HACH's equipment could only monitor BOD continuously for 10 days while the device developed in this study can monitor 20 days or more.

In this case the pH of the sample changed slightly between 7.0 and 8.0, which is a suitable range for the growth of bacteria [9, 10]. Some decreases of pH can be associated with the nitrification process in the bottle, and this will be verified in a future study. These results show that the BOD/pH device can operate efficiently and reliably for a long time period with a high frequency of sampling.

Conclusions

In this study, a novel BOD/pH device based on the respirometric principle that is capable of long-term monitoring both BOD and pH was successfully developed. The fabrication process included steps to define its features and select its components, design of its electronic circuit, calibration, and testing. The data logger software was built in C#. The cross-check with a BOD Trak II equipment (HACH) on a wastewater sample from the pig farm showed that the developed BOD/pH could work stably for up to 20 days and the results obtained from the device are reliable given its similar values to the commercial equipment.

ACKNOWLEDGEMENTS

This research was financed by Vietnam National University, Hanoi (VNU-Project QG.17.18) and Wallonie Bruxelles International (Project No. 15).

The authors declare that there is no conflict of interest regarding the publication of this article.

REFERENCES

[1] S.P. Gorde, M.V. Jadhav (2013), "Assessment of water quality parameters: a review", *Journal of Engineering Research and Applications*, **3(6)**, pp.2029-2035.

[2] N. Horan (2003), "Suspended growth processes", *The Handbook of Water and Wastewater Microbiology*, pp.351-360.

[3] U. Latif, F.L. Dickert (2015), "Biochemical oxygen demand (BOD)", *Environmental Analysis by Electrochemical Sensors and Biosensors*, pp.729-734.

[4] S. Jouanneau, L. Recoules, M.J. Durand, A. Boukabache, V. Picot, V. Primault, A. Lakel, M. Sengelin, B. Barillon, G. Thouand (2014), "Methods for assessing biochemical oxygen demand (BOD): a review", *Water Research*, **49**, pp.62-82.

[5] N. Basant, S. Gupta, A. Malik, K.P. Singh (2010), "Linear and nonlinear modeling for simultaneous prediction of dissolved oxygen and biochemical oxygen demand of the surface water-a case study", *Chemometrics and Intelligent Laboratory Systems*, **104(2)**, pp.172-180.

[6] I.S.A. Abeysiriwardana-Arachchige, N. Nirmalakhandan (2019), "Predicting removal kinetics of biochemical oxygen demand (BOD) and nutrients in a pilot scale fed-batch algal wastewater treatment system", *Algal Research*, **43**, DOI: 10.1016/j.algal.2019.101643.

[7] G. Onkal-Engin, I. Demir, S.N. Engin (2005), "Determination of the relationship between sewage odour and BOD by neural networks", *Environmental Modelling & Software*, **20(7)**, pp.843-850.

[8] M.S. Rahman, M.A. Islam (2015), "A simple cost-effective manometric respirometer: design and application in wastewater biomonitoring", *Applied Water Science*, **5(3)**, pp.241-252.

[9] A.W. Alattabi, C. Harris, R. Alkhaddar, A. Alzeyadi, M. Abdulredha (2017), "Online monitoring of a sequencing batch reactor treating domestic wastewater", *Procedia Engineering*, **196**, pp.800-807.

[10] J. R. Taricska, Y.T. Hung, K.H. Li (2008), "Advances in aerobic systems for treatment of food processing wastewater", *Handbook of Water and Energy Management in Food Processing*, pp.720-754.

DOI: 10.31276/VJSTE.62(3).15-18

Chemical constituents isolated from stems of *Maesa membranacea*

Nguyen Thanh Le[1*], Huu Giap Tran[1], Thi Kim Oanh Vu[1], Thuy Duong Pham[2], Ngoc Thuc Dinh[3], Anna Stojakowska[4], Bich Ngan Truong[1]

[1]*Institute of Marine Biochemistry, Vietnam Academy of Science and Technology, Vietnam*
[2]*College of Science and Engineering, Texas Christian University, USA*
[3]*Department of Science and Technology Management, Hong Duc University, Vietnam*
[4]*Institute of Pharmacology, Krakow, Poland*

Received 16 March 2020; accepted 8 June 2020

Abstract:

***Maesa membranacea* A. DC. (Myrsinaceae) has been traditionally used for the treatment of fever and hepatitis. The phytochemical investigation of *Maesa membranacea* stems has led to the isolation of six compounds including kaempferol (1), (-)-epicatechin (2), betulinic acid (3), *p*-hydroxybenzoic acid (4), vanilic acid (5), and protocatechuic acid (6). The chemical structures of these compounds have been determined by nuclear magnetic resonance (NMR), mass spectrometry (MS) data, and by comparison with previously reported works. This is the first report of a chemical study on *Maesa membranacea* as compounds 1-6 listed above were found from the *Maesa* genus for the first time.**

Keywords: **flavonoids, *Maesa membranacea*, phenolic acids, triterpene.**

Classification number: **2.2**

Introduction

Maesa membranacea A. DC. (Myrsinaceae) is an evergreen shrub that grows in China, Vietnam, and Cambodia. In Vietnam, the leaves and roots of this species have been used as traditional medicine for the treatment of fever and hepatitis [1]. Many *Maesa* plants have also been used as a folk remedy in African and Asian countries. Previous chemical studies on the *Maesa* species have revealed the presence of quinone, saponin triterpenoid, and flavonoid compounds [2-5]. The plant's extracts and chemical constituents have displayed various pharmacological properties such as anticancer, antimicrobial, antiviral, and anti-leismania activity [2-5]. However, until now, no chemical study has been reported on *Maesa membranacea*. In this paper, we report the isolation and structure elucidation of six compounds including kaempferol (**1**), (-)-epicatechin (**2**), betulinic acid (**3**), *p*-hydroxybenzoic acid (**4**), vanilic acid (**5**), and protocatechuic acid (**6**) from the stems of *Maesa membranacea*. The structures of these compounds have been determined by NMR, MS analysis, and comparison with previously reported studies.

Experimental design

Plant materials

The stems of *Maesa membranacea* were collected from the Kontum province, Vietnam, in 2012 and were taxonomically identified by Dr. Nguyen Quoc Binh of the Vietnam Museum of Nature - VAST. A voucher specimen (VN-2292) was provided to the Institute of Marine Biochemistry.

[*]*Corresponding author: Email: lethanh@imbc.vast.vn*

General experimental procedures

The NMR spectra were obtained by a Bruker AM500 FT-NMR spectrometer using TMS as an internal standard. The electrospray ionisation mass spectra (ESI-MS) were obtained on an Agilent 1260 LC/MS system. Column chromatography (CC) was performed on silica gel (Merck, 230-400 mesh), reversed phase silica gel (Merck, RP-C18), or Sephadex LH-20. Precoated silica gel plates (Merck 60 F_{254}) were used for thin layer chromatography. The compounds were detected by a UV lamp or by spraying with 10% sulfuric acid.

Extraction and isolation

The stems of *M. membrancea* (2.0 kg) were extracted with MeOH (10 l × 4 times, 1 day/time) at room temperature. The MeOH solvent was evaporated *in vacuo*. The residue (170 g) was suspended in H_2O and was successively extracted with *n*-hexane and ethyl acetate (3 times x 500 ml/time). The organic solvents were removed *in vacuo* to obtain *n*-hexane (2.8 g) and ethyl acetate residue (18 g), respectively. The water fraction was subjected to a Diaion HP-20 column, eluted with water-MeOH (100:0-0:100) to give a MeOH fraction (6 g).

The ethyl acetate residue (18 g) was subjected to a silica gel column, eluted with a gradient solvent mixture of *n*-hexane-EtOAc (100:0-0:100) to give 16 fractions (E1-E16). Fraction E10 (200 mg) was purified by Sephadex CC and eluted with CH_2Cl_2/MeOH (1/9) to give five sub-fractions denoted as E10.1-E10.5. The sub-fraction E10.3 was fractionated by silica gel CC, eluted with CH_2Cl_2/MeOH (95/5), to yield compound **4** (12 mg) and compound **5** (6 mg). Sub-fraction E10.5 was subjected to Sephadex CC, eluted with CH_2Cl_2/MeOH (2/8) to yield compound **1** (3 mg). Fraction E13 (0.5 g) was separated by Sephadex CC and eluted with CH_2Cl_2/MeOH (2/8) to afford four sub-fractions E13.1- E13.4. Fraction E13.4 (50 mg) was further purified by Sephadex CC using CH_2Cl_2/MeOH (1/9) as mobile phase to afford compound **6** (6 mg). Fraction E15 (0.54 g) was chromatographed on Sephadex CC and eluted with CH_2Cl_2/MeOH (2/8) to afford three sub-fractions E15.1- E15.3. Compound **2** (6 mg) was obtained from sub-fraction E15.3 (60 mg) by crystallisation in acetone/water.

The MeOH fraction (6 g) was separated by reversed phase silica gel CC and eluted with a gradient solvent of water-MeOH (80:20-0:100) to give 15 fractions (E1-E15). Fraction E13 (145 mg) was purified by silica gel CC and eluted with *n*-hexane/acetone (7/3) to yield compound **3** (8 mg).

Kaempferol (**1**): yellow solid; ESI MS *m/z* 287 $[M+H]^+$. ^1H NMR (500 MHz, CD_3OD) δ (ppm): 8.11 (2H, d, *J*=9 Hz, H-2′, 6′), 6.93 (2H, d, *J*=9 Hz, H-3′, 5′); 6.42 (1H, d, *J*=2 Hz, H-8), 6.20 (1H, d, *J*=2 Hz; H-6). ^{13}C NMR (125 MHz, CD_3OD) δ (ppm): 177.3 (C-4), 165.5 (C-7), 162.5 (C-5), 160.5 (C-4′), 158.3 (C-9), 148.1 (C-2), 137.1 (C-3), 130.6 (C-2′,6′), 123.7 (C-1′), 116.3 (C-3′,5′), 104.5 (C-10), 99.2 (C-6), 94.4 (C-8).

(-)-Epicatechin (**2**): white powder, $[\alpha]^{20}_D$-70.50 (*c* 0.20, MeOH), ESI MS (*m/z*): 291 $[M+H]^+$. ^1H NMR (500 MHz, CD_3OD) δ (ppm): 6.99 (1H, d, *J*=1.5 Hz, H-2′), 6.83 (1H, dd, *J*=2.0, 8.0 Hz, H-6′), 6.77 (1H, d, *J*=8.0 Hz, H-5′), 5.96 (1H, d, *J*=2.0 Hz, H-8), 5.94 (1H, d, *J*=2.0 Hz, H-6), 4.83 (1H, br s, 7.5 Hz, H-2), 4.19 (1H, m, H-3), 2.88 (1H, dd, *J*=17.0, 4.5 Hz, H-4a), 2.75 (1H, dd, *J*=16.5, 2.5 Hz, H-4b). ^{13}C NMR (125 MHz, CD_3OD) δ (ppm): 158.0 (C-9), 157.7 (C-7), 157.4 (C-5), 145.9 (C-4′), 145.8 (C-3′), 132.3 (C-1′), 119.4 (C-6′), 115.9 (C-5′), 115.3 (C-2′), 100.1 (C-10), 96.4 (C-6), 95.9 (C-8), 79.8 (C-2), 67.5 (C-3), 29.2 (C-4).

Betulinic acid (**3**): white solid, ESI MS: *m/z* 455 $[M-H]^-$. ^1H NMR (500 MHz, $CDCl_3$) δ (ppm): 4.72 (1H, d, *J*=2.0 Hz, Ha-29), 4.59 (1H, br s, Hb-29), 3.19 (1H, m, H-3), 1.67 (3H, s, H-30), 0.97 (3H, s, H-27), 0.96 (3H, s, H-23), 0.94 (3H, s, H-26), 0.82 (3H, s, H-25), 0.75 (3H, s, H-24). ^{13}C NMR (125 MHz, $CDCl_3$) δ (ppm): 178.9 (C-28), 150.4 (C-20), 109.5 (C-29), 78.6 (C-3), 55.9 (C-17), 55.1 (C-5), 50.4 (C-9), 48.9 (C-18), 46.7 (C-19), 42.1 (C-14), 40.4 (C-8), 38.5 (C-4), 38.5 (C-1), 37.9 (C-13), 36.9 (C-10), 36.8 (C-22), 34.0 (C-7), 32.0 (C-16), 30.4 (C-21), 29.4 (C-15), 27.8 (C-23), 27.1 (C-2), 25.3 (C-12), 20.7 (C-11), 19.0 (C-30), 18.1 (C-6), 15.9 (C-25), 15.6 (C-26), 15.1 (C-24), 14.4 (C-27).

***p*-Hydroxybenzoic acid** (**4**): white solid. ESI MS *m/z* 139 $[M+H]^+$. ^1H NMR (500 MHz, CD_3OD) δ (ppm): 7.89 (2H, d, *J*=9.0 Hz, H-2,6), 6.84 (2H, d, *J*=8.0 Hz, H-3,5). ^{13}C NMR (125 MHz, CD_3OD) δ (ppm): 170.1 (COOH), 163.3 (C-4), 133.0 (C-2,6), 122.7 (C-1), 116.0 (C-3,5).

Vanilic acid (**5**): white solid. ESI MS *m/z* 169 $[M+H]^+$. ^1H NMR (500 MHz, CD_3OD) δ (ppm): 7.58 (1H, d, *J*=1 Hz, H-2), 7.56 (1H, dd, *J*=2.0, 8.0 Hz, H-6), 6.85 (1H, d, *J*=8.5 Hz, H-5), 3.91 (3H, s, OMe). ^{13}C NMR (125 MHz, CD_3OD) δ (ppm): 168.0 (COOH), 151.5 (C-3), 147.6 (C-4), 124.1 (C-1), 123.0 (C-6), 116.7 (C-2), 114.7 (C-5), 55.4 (OCH_3).

Protocatechuic acid (**6**): white solid. ESI MS *m/z* 155 $[M+H]^+$. ^1H NMR (500 MHz, CD_3OD) δ (ppm): 7.46 (1H, d, *J*=2 Hz, H-2), 7.44 (1H, dd, *J*=2.0, 8.0 Hz, H-6), 6.81 (1H, d, *J*=8.0 Hz, H-5). ^{13}C NMR (125 MHz, CD_3OD) δ (ppm): 169.2 (C-7), 150.4 (C-4), 144.9 (C-3), 122.8 (C-6), 122.0 (C-1), 116.6 (C-5), 114.6 (C-2).

Results and discussion

Compound 1 was isolated from the ethyl acetate extract as a yellow solid. The ESI MS spectrum showed a *quasi*-molecular ion peak with *m/z* 287 $[M+H]^+$, which suggests the molecular formula of **1** is $C_{15}H_{10}O_6$ (M=286). The ^1H NMR spectrum showed signals of a flavonol with two proton signals at δ_H 6.42 (1H, d, *J*=2 Hz, H-8) and 6.20 (1H, d, *J*=2 Hz, H-6), proton signals of an A_2B_2 system at δ_H 8.11 (2H, d, *J*=9 Hz, H-2′, 6′) and 6.93 (2H, d, *J*=9 Hz, H-3′, 5′).

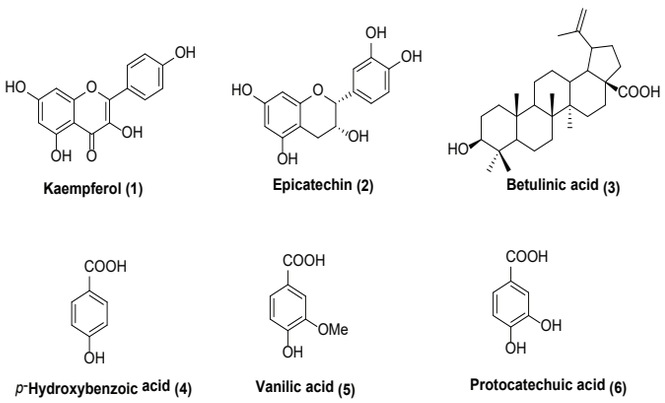

Fig. 1. Chemical structures of compounds 1-6.

The ^{13}C NMR spectrum of **1** revealed 15 carbon signals including a carbonyl signal at δ_C 177.3 (C-4), 5 oxy-bonded carbons at δ_C 165.5 (C-7), 162.5 (C-5), 160.5 (C-4′), 158.3 (C-9), and 148.1 (C-2), and 2 double peaks at δ_C 130.6 (C-2′, 6′) and 116.3 (C-3′, 5′). The structure of compound **1** was assigned as kaempferol. The NMR data of **1** are in agreement with the values published [6].

Compound **2** yielded as a white solid. The ESI MS showed a *quasi*-molecular ion peak of *m/z* 291 $[M+H]^+$,that corresponds to a molecular formula of $C_{15}H_{14}O_6$ (M=290). The ^1H NMR spectrum revealed typical signals of a flavanol including the three aromatic protons in an ABX system at δ_H 6.99 (1H, d, *J*=1.5 Hz, H-2′), 6.83 (1H, dd, *J*=2.0, 8.0 Hz, H-6′), 6.77 (1H, d, *J*=8.0 Hz, H-5′), 2 aromatic proton at δ_H 5.96 (1H, d, *J*=2.0 Hz, H-8), 5.94 (1H, d, *J*=2.0 Hz, H-6). The proton signals of the pyran unit were displayed at δ_H 4.83 (1H, br s, 7.5 Hz, H-2), 4.19 (1H, m, H-3), 2.88 (1H, dd, *J*=17.0, 4.5 Hz, H-4a), and δ_H 2.75 (1H, dd, *J*=16.5, 2.5 Hz, H-4b). The H-2 and H-3 protons were observed as broad peaks, which suggested that these protons were on the same side. The ^{13}C NMR spectrum of **2** showed 15 carbon signals. Based on the spectral analysis and optical rotation data, **2** was identified as (-)-epicatechin. The NMR data of **2** agree with previously reported literature [7].

Compound **3** was obtained from the MeOH fraction as a white solid. The ESI MS showed a *pseudo*-molecular ion peak of *m/z* 455 $[M-H]^-$ and the suggested molecular formula of **3** is $C_{30}H_{48}O_3$ (M=456). The ^1H NMR spectrum revealed the typical signals of a lupan-type structure with 2 olefinic peaks at δ_H 4.72 (1H, d, *J*=2.0 Hz, Ha-29) and 4.59 (1H, br s, Hb-29), and six singlet signals of methyl groups at δ_H 1.67 (3H, H-30), 0.97 (3H, H-27), 0.96 (3H, H-23), 0.94 (3H, H-26), 0.82 (3H, H-25), and 0.75 (3H, H-24). In addition, the signals from the oxymethine group were found at δ_H 3.19 (1H, m, H-3). The ^{13}C NMR and distortionless enhancement by polarization transfer (DEPT) spectra of **3** showed 30 carbon signals including a signal from the carboxylic group at δ_C 178.9 (C-28), peaks of 2 olefinic carbons at δ_C 150.4 (C-20) and 109.5 (C-29), and signals from 6 methyl groups at δ_C 27.8 (C-23), 19.0 (C-30), 15.9 (C-25), 15.6 (C-26), 15.1 (C-24), and 14.4 (C-27). Therefore, compound **3** was determined as betulinic acid. The NMR data of **5** agrees with those from the reported work of [8].

Compounds **4-6** were determined as *p*-hydroxybenzoic acid, vanilic acid, and protocatechuic acid, respectively, by comparison of the NMR data with reported literatures [9, 10] (Fig. 1).

Conclusions

A phytochemical investigation of *M. membranceae* stems led to the isolation of six known compounds identified as kaempferol (**1**), (-)-epicatechin (**2**), betulinic acid (**3**), *p*-hydroxybenzoic acid (**4**), vanilic acid (**5**), and protocatechuic acid (**6**). This is the first chemical study on the *Maesa membranceae* plant. All of the isolated compounds were found from *Measa* genus for the first time.

ACKNOWLEDGEMENTS

This research is funded by Vietnam Academy of Science and Technology under grant number QTPL01.01/19-20.

The authors declare that there is no conflict of interest regarding the publication of this article.

REFERENCES

[1] V.V. Chi (2012), *Dictionary of Vietnamese Medicinal Plants*, Medical Publisher, **1**, pp.963-964.

[2] J.O. Midiwo, L.M. Arot (1996), "New dialkyl benzoquinones from fruits of *Myrsine africana* L and *Maesa lanceolata*, Forsk", *Natural Product Letters*, **8(1)**, pp.11-14.

[3] K. Koike, M. Kudo, Z. Jia, T. Nikaido, Y. Ide, T. Sakura (1999), "New triterpenoid saponins from *Maesa japonica*", *Journal of Natural Products*, **62(2)**, pp.228-232.

[4] L.O.A. Manguro, P. Lemmen, I. Ugi, W. Kraus (2002), "Flavonol glycosides of *Maesa lanceolata* leaves", *Nat. Prod. Sci.*, **8(3)**, pp.77-82.

[5] N. Germonprez, L. Van Puyvelde, L. Maes, M. Van Tri, N. De Kimpe (2004), "New pentacyclic triterpene saponins with strong anti-leishmanial activity from the leaves of *Maesa balansae*", *Tetrahedron*, **60(1)**, pp.219-228.

[6] Y.L. Li, J. Li, N.L. Wang, X.S. Yao (2008), "Flavonoids and a new polyacetylene from *Bidens parviflora* Willd", *Molecules*, **13(8)**, pp.1931-1941.

[7] H.V.T. Nguyen, B.C. Pham, I.T. Cam, P.L. Doan, T.T. Le, T.Q. Tran, L.Q. Pham (2019), "Flavonoids isolated from the flowers of *Camellia chrysantha*", *Vietnam Journal of Science and Technology*, **57(3)**, pp.287-293.

[8] S. Khaliq, F.J. Volk, A.W. Frahm (2007), "Phytochemical investigation of *Perovskia abrotanoides*", *Planta Medica*, **73(1)**, pp.77-83.

[9] G.Y. Chen, C.Y. Dai, T.S. Wang, C.W. Jiang, C.R. Han, X.P. Song (2010), "A new flavonol from the stem-bark of *Premna fulva*", *Arkivoc.*, **2**, pp.179-185.

[10] S.W. Chang, K.H. Kim, I.K. Lee, S.U. Choi, S.Y. Ryu, K.R. Lee (2009), "Phytochemical constituents of *Bistorta manshuriensis*", *Nat. Prod. Sci*, **15**, pp.234-240.

DOI: 10.31276/VJSTE.62(3).19-25

Comparison and applicability of Agilent EMR-Lipid and Captiva EMR-Lipid Sorbents in QuEChERS method for food analysis

Quang Hoang Hanh Le[1], Nguyen Ngoc Chau Tran[1], Thi Cam Tuyen Nguyen[1], Huong Giang Nguyen[2], Kien Trieu Lac[2], Thi Anh Pham[3] and Pham Ngoc Son Chu[3*]

[1]TSL Hi-Tech Training and Research Center
[2]Ho Chi Minh City Centre for the Quality Control of Food, Drug and Cosmetics
[3]Chemical Society of Ho Chi Minh City

Received 12 May 2020; accepted 11 August 2020

Abstract:

Agilent's innovative EMR-Lipid and Captiva EMR-Lipid sorbents efficiently replace the traditional QuEChERS d-SPE clean-up products in selective lipid removal from fatty matrices, thus improving instrumental analytical reproducibility, reliability, and long-term use. These products have dual functionality; a hydrophobic interaction between the sorbent with long aliphatic lipid chains of the matrices, which allows for complete lipid retention, and a size exclusion property that does not retain analytes, thus this maximizes, in principle, analyte recovery in any sample. As most of the analytes under study were polar or not highly nonpolar and had a relatively large size, the examination of small-sized nonpolar or less polar compounds is necessary to check for partial retention by the sorbents and if any, further precautions should be taken when using these sorbents. These queries are answered in our present communication concerning the analytes Trifluralin (logP: 5.27), Fipronil (logP: 4.0), and Clenbuterol (logP: 2.63).

Keywords: **Captiva EMR-Lipid, EMR-Lipid Sorbents, size exclusion and hydrophobic interaction with fatty materials, food analysis.**

Classification number: **2.2**

Introduction

The QuEChERS method has been widely adopted in sample preparation not only for pesticides but for other analytes as well. For fatty samples, Agilent replaced the traditional d-SPE products in the QuEChERS clean-up step with two new sorbents: the Enhanced Matrix Removal for lipids known as EMR-Lipid (2015) and the Captiva EMR-Lipid (2017). These nanosorbents have two similar functions; a hydrophobic interaction with long aliphatic chains allowing the selective removal of fatty materials from matrices and a size exclusion property preventing the retention of analytes [1, 2]. For optimum performance, the EMR-Lipid must be activated with water (3-5 ml of water per 1 g of sorbent) while the Captiva EMR-Lipid requires an organic extract containing 20% water by volume (Fig. 1).

The attractive pass-through for a Captiva EMR-Lipid cartridge version requires less manual work, which allows for easy and effective clean-up of the analyte without clogging, this is especially important in case of biological fluids. This feature constitutes a major advantage over the EMR-Lipid powder presentation. For example, the EMR-Lipid has been applied to the analysis of veterinary drugs in bovine liver (30 different drugs at concentrations of 2, 10, 50, 150, 250, and 750 ng/g with recoveries between 60-120%) [3], PAH in salmon (15 PAH at concentrations of 25, 100, and 500 ng/g with recoveries between 62-98%) [4], pesticides in avocado (23 pesticides at a concentration 50 ng/g with absolute recoveries without using deuterated internal standards between 60-110%, however it was below 50% with aldrin and DDT) [5]. EMR-Lipid was also used by our group in 2016 for the analysis of ethoxyquin in feedstuffs, where no matrix effect was detected and the recovery was almost quantitative [6]. Captiva EMR-

*Corresponding author: Email: cpnson@gmail.com

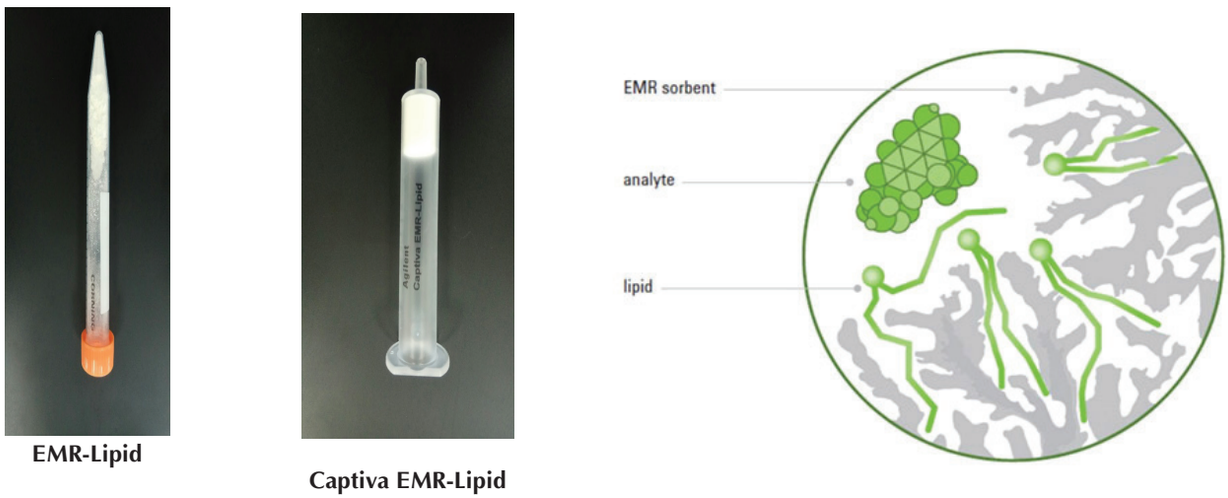

Fig. 1. EMR-Lipid, Captiva EMR-Lipid cartridges and schematic of the mechanism of action [1].

Lipid has also been applied to the analysis of mycotoxins in cheese [7]. For example, from parmesan and blue cheeses with mycotoxin concentrations of 1, 5, and 10 ng/g, the recoveries ranged between 70-112% for AFB1, AFB2, AFG1, AFG2, Mycophenolic acid, Ochratoxin A, Sterigmatocystin, and zearalenone. In many applications of these Agilent products, the highly selective removal of fatty materials from matrices was always emphasized while the role of the size exclusion property was mentioned much less. Indeed, careful examination has shown that these analytes were not highly nonpolar (logP<5.5) and had a relatively large size, therefore, they were not retained by the sorbents through either the hydrophobic interaction or by retention due to size effect.

In view of these experimental results and with the aim to detect a possible interaction between sorbent and analyte that may influence the recovery, we studied a selection of compounds with decreasing hydrophobicity in the following order: Trifluralin (logP=5.27), Fipronil (logP=4.0) and Clenbuterol (logP=2.63). Trifluralin, a pre-emergence dinitroaniline herbicide that is quite toxic to aquatic life, was banned in Vietnam in 2010 and in 2013 the Japanese revised their maximum residue level (MRL) standard to be 0.5 mg/kg in seafood products. This herbicide was analysed in Basa catfish by our group using gas chromatography-mass spectrometry (GC-MS) coupled with the QuEChERS method for sample preparation. In that work, no matrix effect was found and the recovery was nearly quantitative [8]. Fipronil, a highly toxic phenylpyrazole insecticide (EU MRL: 5 ppb) [9], was detected in 2017 in eggs in Belgium, the Netherlands, and later on in many other countries, thus causing a recall of millions of eggs from human consumption. Clenbuterol is not allowed to be used as a growth-promoter for pork in Vietnam (Codex MRL: 0.2 µg/kg and 0.6 µg/kg, respectively, for meat and liver). According to the Vietnamese circular No.01/2016/TT-BNNPTNT [10] dated February 15, 2016, a quick strip test for Clenbuterol detection in pig urine gives a positive screening result if the residue is above 3 µg/l.

To serve our purpose, we performed the analysis of Trifluralin spiked in blank shrimp, Fipronil in blank egg, and the direct analysis of Trifluralin and Clenbuterol standard solutions after treatment with these Agilent sorbents in sample preparation.

Both the pre-spiked and post-spiked samples for Trifluralin and Fipronil were analysed to estimate the matrix effect and to determine their recoveries by comparison with the corresponding standard solutions used to prepare them. For Clenbuterol and Trifluralin, the direct treatment of standard solutions with the sorbents would allow the prediction of their applicability to the quantitation of these analytes in various matrices. Both sorbent functions were examined in relation to the hydrophobicity and the bulkiness of these analytes.

Materials and methods

Chemicals

Standards: Trifluralin (99.5%, Dr. Ehrenstorfer), Fipronil (98.7%, Dr. Ehrenstorfer), Clenbuterol (99.34%, Dr. Ehrenstorfer), Trifluralin-d14 (100 mg/l in acetone, Dr. Ehrenstorfer).

Reagents: acetonitrile (≥99.9%, LCMS grade, J.T. Baker), isooctane (≥99.8% GC grade, Merck), acetic acid (≥98% ACS, J.T. Baker), anhydrous sodium acetate (≥99%, AR, Xilong), anhydrous magnesium sulfate (≥99%, AR, Xilong), anhydrous sodium chloride (≥99.5%, AR, Xilong), anhydrous sodium sulfate (≥99% ACS, Scharlau). All anhydrous reagents were re-dried at 110°C for 5 h before use.

Sorbents: EMR-Lipid (1 g in 15 ml tube, Part number 5982-1010, Agilent). Captiva EMR-Lipid (3 ml tube, 300 mg, Part Number 5190-1003 or 6 ml tube, 600 mg, Part number 5190-1004, Agilent).

Sample preparation and GC-MS/MS or LC-MS/MS operating conditions

The following Figs. 2-4 describe the sample preparation process and Tables 1-2 provide the equipment's operating conditions.

Extraction	EMR-Lipid Cleanup	Captiva EMR-Lipid Cleanup
Pre-spiked sample		
1 g of blank shrimp + 50 µl of 1 ppm T + 100 µl of 1 ppm T-d14, vortex, let stand for 1 hr ↓ Classical QuEChERS with 10 ml ACN (1% AcOH) + 1 ml H_2O + (2.4 g $MgSO_4$ + 0.6 g NaOAc) ↓ Vortex, centrifugate and collect the supernatant A	Supernatant A loaded into 15 ml EMR-Lipid tube preactivated with 3 ml H_2O ↓ Vortex, centrifugate , collect supernatant B + 1 ml isooctane + sufficient 4% NaCl solution, vortex and allow separation of the mixture into 2 layers ↓ Collect isooctane layer, filter through 0.22 µm nylon filter → solution ready for GC-MS/MS analysis	(A + 2.5 ml H_2O) loaded into a 6 ml Captiva EMR-Lipid cartridge and allowed flowing through the cartridge by gravity ↓ Subsequently wash with solution (1.6 ml ACN + 0.4 ml H_2O) ↓ Collect the entire solution + 1 ml isooctane+ sufficient 4 % NaCl solution and proceed as described in case of EMR-Lipid cleanup to get the isooctane solution ready for analysis
Post-spiked sample		
Repeat the extraction as above described but with only 1 g of blank shrimp (no standard solution) → Collect supernatant C	Treat C exactly the same way as above described for pre-spiked sample with EMR-Lipid until getting the isooctane layer ↓ Take 850 µl isooctane + 50 µl of 1 ppm T + 100 µl of 1 ppm T-d14, vortex, filter to get solution ready for GC-MS/MS analysis	Treat C exactly the same way as above described for pre-spiked sample with Captiva EMR-Lipid until getting the isooctane layer ↓ Take 850 µl isooctane + 50 µl of 1 ppm T + 100 µl of 1 ppm T-d14, vortex, filter to get solution ready for analysis
Standard solution		
Solution of 50 µl of 1 ppm T + 100 µl of 1 ppm T-d14 + 10 ml ACN	Treat the standard solution exactly as above described for A with EMR-Lipid cartridge preactivated with 3 ml H_2O to get the isooctane solution ready for analysis	Treat the standard solution + 2.5 ml H_2O exactly as above described for pre-spiked solution until getting the isooctane ready for analysis

Fig. 2. Sample preparation for Trifluralin (T).

Extraction	EMR-Lipid Cleanup	Captiva EMR-Lipid Cleanup
Pre-spiked sample		
5 g of homogenized egg + 1 ml of 10 ppb F, vortex, let stand for 1 hr ↓ Add 3 ml H_2O + ceramic homogenizer, vortex ↓ Add 10 ml ACN, vortex, add slowly 4 g $MgSO_4$ + 1 g NaCl, vortex, centrifugate, collect supernatant D	5 ml D loaded into 15 ml EMR-Lipid tube preactivated with 3 ml H_2O,vortex, centrifugate ↓ Collect supernatant, dry under N_2, ↓ Redissolve residue in 1 ml of MeOH:H_2O (1:1) + filter through 0.22 µm nylon syringe filter ↓ Solution ready for LC-MS/MS analysis	(5 ml D + 1.25 ml H_2O) loaded into the 6 ml Captiva EMR-Lipid cartridge and allowed flowing through the cartridge by gravity Subsequently wash with 1 ml ACN:H_2O (4:1) ↓ Collect supernatant, dry under N_2, 60°C ↓ Proceed as described in case of EMR-Lipid clean-up to get the solution ready for analysis
Post-spiked sample		
5 g of homogenized egg ↓ Proceed exactly as above described without standard ↓ Collect supernatant E	Treat E exactly as above described for pre-spiked sample with EMR-Lipid until drying the supernatant under N_2, 60°C ↓ Redissolve residue in 1 ml of 5 ppb fipronil standard solution + filter to get the solution ready for analysis	Treat E exactly as above described for pre-spiked sample with Captiva EMR-Lipid cartridge until drying the supernatant under N_2, 60°C ↓ Proceed as described in case of EMR-Lipid clean-up to get the solution ready for analysis

Fig. 3. Sample preparation for Fipronil (F).

EMR-Lipid Cleanup	Captiva EMR-Lipid Cleanup
Add 30 µl of 100 µg/l clenbuterol standard to 10 ml of 1% AcOH solution in acetonitrile, vortex	
Load solution into a 15 ml EMR-Lipid cartridge, preactivated with 3 ml H_2O,vortex, centrifugate	- Mix with 2.5 ml H_2O - Load into the 6 ml Captiva EMR-Lipid column - Wash column by (1.6 ml ACN + 0.4 ml H_2O)
- Add 3 g anhydrous Na_2SO_4 vortex, centrifugate - Take the supernatant, evaporate by rotavaporization at 60°C under light vacuum - Redissolve in 1 ml of solution of [90% H_2O (0.1% HCOOH) + 10% ACN (0.1% HCOOH)], analyze on Shimadzu UPLC-MS/MS TQ 8050	

Fig. 4. Pre-treatment of Clenbuterol standard with Agilent sorbents.

Table 1. GC-MS TQ 8050 operating conditions for Trifluralin.

Equipment	GC 2010 Plus	MS TQ 8050
Shimadzu GC- MS/MS TQ 8050 equipped with Combi-Pal PTV	- Column: DB5 MS UI (30 m x 0.5 mm x 0.25 µm) - Injector temperature: 250°C - Mode: Splitless, Sampling time: 1 min - Flow rate: 1.5 ml/min - Temperature program: Rate (°C/min) / Final temperature (°C) / Hold time (min) - / 50 / 0 15 / 180 / 0 3 / 190 / 0 35 / 310 / 4	- Acquisition mode: EI - MRM - Emission current: 150 µA - Ion source temperature: 200°C - Transfer line temperature: 250°C - CID gas pressure: 180 kPa - MS Resolution: Q1 unit, Q3 unit - Detector: 1.11 kV - Precursor ion, *m/z*=306.00 - Quantifier ion *m/z*=264.00, CE: 9 ev - Qualifier ion: *m/z*=160.10, CE: 18 ev - Quantifier ion from precursor ion *m/z*=315.00 for Trifluralin-d14, *m/z*=267.10, CE: 9 ev

Table 2. Thermo scientific LC- tandem MS operating conditions for Fipronil and Clenbuterol.

Analyte		Fipronil	Clenbuterol
Equipment		Thermo Scientific LC-MS/MS (Ultimate 3000 HPLC-TSQ Quantum Access Max)	Shimadzu UPLC-MS/MS TQ 8050
HPLC	Column	Agilent Poroshell C18 (100 x 2.1 mm, 2.7 µm)	Phenomenex Poroshell C18 (150 x 2.1 mm, 1.7 µm)
	Column T°	40°C	40°C
	Flow rate	0.3 ml/min	0.2 ml/min
	Injection volume	2 µl	5 µl
	Mobile phase	A: MeOH; B: H_2O	A: H_2O (0.1 % HCOOH) B: ACN (0.1 % HCOOH)
	Gradient program	Time (min) / A (%) / B (%) 0 - 3 / 60 - 70 / 40 - 30 3 - 6.6 / 70 / 30 6.6 - 6.7 / 70 - 98 / 30 - 2 6.7 - 10 / 98 / 2 10 - 10.1 / 98 - 60 / 2 - 40 10.1 - 16 / 60 / 40	Time (min) / A (%) / B (%) 0.01 - 1 / 90 / 10 1.01 - 2.5 / 90 - 65 / 10 - 35 2.51 - 8.5 / 65 / 35 8.51 - 9 / 65 - 90 / 35 - 10 9.01 - 14 / 90 / 10
MS	MS mode	ESI (-)	ESI (+)
	Parameters	- Spray voltage: 3.000 V - Vaporizer temperature: 300°C - Sheath gas pressure (N_2): 35 - Auxiliary gas pressure (N_2): 10 - Capillary temperature: 270°C - Collision gas (Ar): 1.5 m Torr - Q1, Q3 Peak resolution: 0.7u	- Interface voltage: 4000 V - Interface t°: 300°C - Nebulizing gas flow: 2 l/min - Heating gas flow: 12 l/min - DL temperature: 250°C - Heat block temperature: 350°C - Drying gas flow: 4 l/min
	Precursor ion	*m/z*=435	*m/z*=277
	Quantifier ion	*m/z*=330, CE: 17 ev	*m/z*=203, CE: 16 ev
	Qualifier ion	*m/z*=250, CE: 27 ev	*m/z*=259, CE: 10 ev

Results and discussions

Table 3 summarizes the analytical results obtained with Trifluralin, Fipronil, and Clenbuterol.

Table 3. Analytical results for Trifluralin, Fipronil, and Clenbuterol.

Agilent sorbents	Samples	Average Recovery H% (n=5)			
		Trifluralin		*Fipronil*	*Clenbuterol Std Solution*
		STD (50 µg/l)	ISTD (100 µg/l)	STD (5 µg/l)	STD (5 µg/l)
EMR-Lipid	Standard	51.81	51.24	-	63.27
	Pre-spiked sample	27.11	25.65	75.50	-
	Post-spiked sample	104.30	103.00	101.40	-
Captiva EMR-Lipid	Standard	65.99	63.75	-	44.67
	Pre-spiked sample	31.75	31.40	72.10	-
	Post-spiked sample	102.10	101.60	96.40	-

For Trifluralin, the analytical results indicated no matrix effect as in the original QuEChERS method of sample preparation [8]. However, they also showed that it would be unsuitable to use EMR-Lipid and Captiva EMR-Lipid in sample preparation for Trifluralin analysis because of quite low recoveries in pre-spiked samples; this was also shown in the direct treatment of a Trifluralin standard with the sorbents.

For Fipronil, the results indicated also no matrix effect and the recoveries for pre-spiked samples on treatment with both Agilent sorbents were acceptable in view of the complexity of the egg matrix.

For Clenbuterol, the quite low recovery of a standard solution after treatment with EMR-Lipid and Captiva EMR-Lipid sorbents indicated that they would not be appropriate for this analyte in any matrix.

The analytical results showed therefore that Agilent sorbents could replace the well-known QuEChERS clean-up products for Fipronil [11]. However, for Trifluralin and Clenbuterol, both the Agilent EMR-Lipid and Captiva EMR-Lipid appeared not working properly. To our knowledge, no such information has been provided until now. Therefore, from our study and other previous works [3-5, 7] using these Agilent products for sample preparation, we propose an explanation of these effects that involve the analyte polarity, bulkiness, and the two functions of the sorbents.

Case of bulky and not highly nonpolar analytes

Almost all reported analytes that successfully used Agilent products were bulky and not highly hydrophobic (logP<5.5). Their bulkiness plays a somewhat more important role, which aids analytes from being retained by the sorbents because of the size exclusion property of the latter.

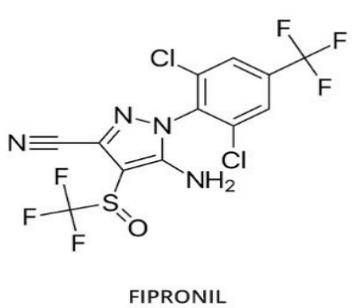

Fipronil

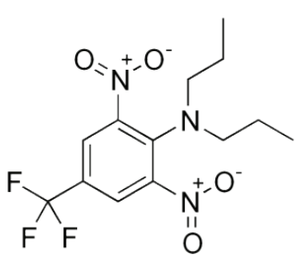

Trifluralin

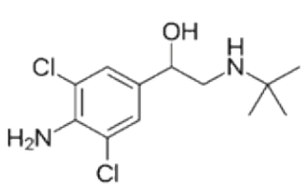

Clenbuterol

However, for a few nonpolar compounds (logP>6) such as permethrin (logP=6.1), aldrin (logP=6.50), and DDT (logP=6.91), their low recoveries (permethrin=63%, aldrin and DDT<50%) would probably be caused by the hydrophobicity of the sorbent EMR-Lipid, which partially retained the analytes through a nonpolar interaction during the clean-up step [5].

Case of small-sized compounds

There are a few small-sized compounds that could benefit from Agilent sorbents during sample preparation due to their strong polar character (i.e. the veterinary drug 2-thiouracil in bovine liver with logP=-0.28) or the presence of polar substituents around the nucleus (i.e. the veterinary drug clorsulon in bovine liver with logP=1.25 and the pesticide chlorothalonil in avocado with logP=2.94).

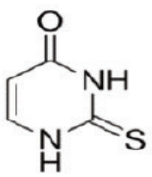

2-Thiouracil

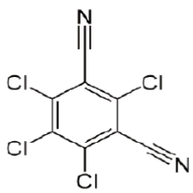

Chlorothalonil

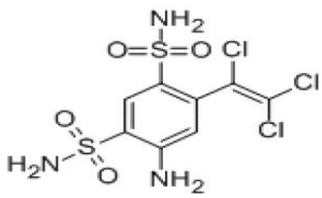

Clorsulon

Our case studies

In our case, Agilent sorbents may be used for Fipronil residue analysis (logP=4.0) because of its somewhat bulky structure with two rings and the presence of polar substituents on the pyrazole ring. Likewise, our previous work on the analysis of ethoxyquin (logP=4.01) in feedstuffs with EMR-Lipid (which had been made available since 2016), gave good analyte recoveries of 95.95-99.33% at concentrations ranging between 6-15 mg/kg of ethoxyquin [6]. This was probably due to the bulkiness of the analyte with two fused rings and the presence of the polar quinoline ring. At this point, we would like to note that in 2013 our study showed that the traditional QuEChERS method of sample preparation worked well in the analysis of ethoxyquin in shrimp (recovery better than 95%) [12].

For Trifluralin (logP=5.27), the hydrophobic character, the relatively small size of the analyte with only one ring structure, and the presence of two hydrophobic propyl groups would favour its partial attraction and retention by the sorbents. In 2010, however, we showed that the traditional QuEChERS clean-up worked well in the analysis of this analyte in Basa fish (no matrix effect and recoveries >91% for all samples) [8]. For Clenbuterol (logP=2.64), its insufficient polar character and less bulky structure would justify its partial retention through interaction of its nonpolar part with the Agilent sorbents.

Furthermore, results also showed that in the case of Trifluralin in shrimp, the low recoveries with a pre-spiked standard solution originated mainly from the incomplete recovery on the direct treatment of Trifluralin standard with the sorbents. Therefore, the direct treatment of an analyte standard with EMR-Lipid and Captiva EMR-Lipid would provide a simple way to quickly predict the applicability of these sorbents to the analyte in sample preparation. This was the case of Clenbuterol for example, showing that the use of these sorbents in sample preparation might not be appropriate.

Conclusion

Agilent EMR-Lipid and Captiva EMR-Lipid were applied to the analysis of Trifluralin in shrimp, Fipronil in eggs and Clenbuterol standard for the purpose to find any possible interaction of the sorbents with the analytes. In fact, we found that only Fipronil worked well. An explanation was proposed to understand any difference in comportment of the sorbents toward various analytes. In general, Agilent sorbents may be successfully used for polar analytes, bulky analytes and even small-sized analytes with polar substituents surrounding the nucleus. Agilent sorbents may not be correctly applied to highly nonpolar compounds or small-sized analytes bearing hydrophobic substituents. A quick way to evaluate the applicability of the sorbents for

an analyte is to perform the analysis by direct loading of a standard solution of the analyte into the sorbents.

The authors declare that there is no conflict of interest regarding the publication of this article.

REFERENCES

[1] D. Lucas, L. Zhao, B. Richter, J. Stevens and P. Wylie (2016), *Improving the Robustness of Multi-residue Resticides Analysis Through Enhanced Sample Matrix Removal,* Agilent Technologies, 11th European Pesticide Residue Workshop EPRW 2016. Poster PV 025.

[2] L. Zhao, D. Lucas (2017), *Efficiency of Biological Fluid Matrix Removal Using Agilent Captiva EMR-Lipid Cleanup,* Agilent Technologies, Inc., Application Note 5991-8006 EN, pp.1-10.

[3] L. Zhao, D. Lucas (2015), *Mutiresidue Analysis of Veterinary Drugs in Bovine Liver*, Agilent Technologies, Inc., Application Note 5991-6096 EN, pp.1-18.

[4] D. Lucas, L. Zhao (2015), *PAH Analysis in Salmon with Enhanced Matrix Removal*, Agilent Technologies, Inc, Application Note 5991-6088 EN, pp.1-8.

[5] L. Zhao, D. Lucas (2015), *Multiresidue Analysis of Pesticides in Avocado with Agilent Bond Elut Enhanced Matrix-Removal by GC/MS/MS*, Agilent Technologies, Inc, Application Note 5991-6097 EN, pp.1-16.

[6] Pham Thi Anh, Chu Pham Ngoc Son (2016), *Sample Preparation for Food Analysis*, Philippines Institute of Pure and Applied Chemistry PIPAC - Shimadzu Food Safety Seminar, Manila, Philippines.

[7] D. Lucas, L. Zhao (2017), *Multiclass Mycotoxin Analysis in Cheese Using Agilent Captiva EMR-Lipid Cleanup and LC/MSMS*, Agilent Technologies, Inc, Application Note 5991-8694 EN, pp.1-8.

[8] Nguyen Phuong Phi, Vo Truong Duy, Pham Thi Anh, Chu Pham Ngoc Son (2010), "Analysis of Trifluralin in Basa Fish by GC/MS Combined with QuEChERS Method of Sample Preparation", *J. Anal. Sci.,* **15(3)**, pp.255-260.

[9] A. Sage, J. Stahl-Zeng, J. Causon, M. Whitmore, S. El Ouadi, J. Franken, J. Van Leeuwen, M. Martha, P. Taylor (2017), *Rapid LC-MS/MS Method for the Analysis of Fipronil and Amitraz Insecticides and Associated Metabolites in Egg and other Poultry Products,* AB Sciex Document No RUO-MKT-02-6607-A, pp.1-5.

[10] Vietnam Ministry of Agriculture and Rural Development (2016), *Supplements and Amendments to a Number of Articles in of Circular No 57/2012/TT-BNNPTNT Stipulating Inspection, Supervision and Penalties for use of Substances in β-Agonist Group Banned from Liverstock Production*, Circular No 01/2016/TT-BNNPTNT.

[11] Q. Guo, S. Zhao, J. Zhang, K. Qi, Z. Du, B. Shao (2018), "Determination of fipronil and its metabolites in chicken egg, muscle and cake by a modified QuEChERS method coupled with LC-MS/MS", *Food Addit, Contam. part A Chem. Anal. Control. Expo. Risk Assess*, **35(8)**, pp.1543-1552.

[12] Nguyen Hong Thao, Nguyen Phuong Phi, Pham Thi Anh, Chu Pham Ngoc Son (2013), "Analysis of ethoxyquin in shrimp by LC-MS/MS combined with QuEChERS method of sample preparation", *The Third Analytica Vietnam Conference Proceeding,* pp.199-203.

DOI: 10.31276/VJSTE.62(3).26-32

A study on synthesis and properties of SAPs based on carboxymethyl cellulose

Thi Tuyet Mai Phan*, Ho Viet Cuong, Pham Ngoc Lan

Department of Chemistry, University of Science, Vietnam National University, Hanoi

Received 3 April 2020; accepted 2 July 2020

Abstract:

Carboxymethyl cellulose-graft-poly(acrylic acid-Sodium acrylate-acrylamide) SAPs have been prepared by the free-radical grafting solution polymerization of acrylic acid (AA) and acrylamide monomers (AM) onto carboxymethyl cellulose (CMC) in the presence of N,N′-methylenebisacrylamide as a crosslinker (MBA) and ammonium persulfate (APS) as an initiator. Various factors influencing the water absorbency of the polymer were studied. These include the weight ratio of APS, MBA, and CMC compared to the monomers. The optimal conditions were found as follows: 1% APS, 0.25% MBA, and 10% CMC (weight ratio to monomers). The maximum absorbencies for distilled water and 0.9 wt.% NaCl solution were 406 g/g and 69 g/g, respectively. The structure of the synthesized polymer was confirmed by Fourier Transform Infrared spectroscopy (FTIR). Additionally, the water absorption and water retention behavior of the polymer in soil were investigated. The results showed that this polymer could be employed as a suitable moisture-holding additive in soil for cultivation purposes.

Keywords: **absorbency, carboxymethyl cellulose, retention behaviour, SAP, water holding.**

Classification number: **2.2**

Introduction

Due to the water resource crisis, conserving water is essential for the sustainable development of agricultural production. Thus, there is an increasing urgent the need to use superabsorbent (SAP) in agriculture. After water absorption, SAP particles act as reservoirs near the root system that help to increase both the amount of water and the amount of time available for plants to grow [1-4]. However, because SAP is difficult to decompose, their use has negative impacts on the soil and the environment. For this reason, studying the manufacture of superabsorbent biodegradable polymers (BioSAP) is indispensable in order to trend to develop these products for use in the near future. BioSAP products can be synthesized from renewable materials such as cellulose, starch, chitin, natural resins, and so on. In particular, cellulose and their derivatives, such as CMC, are attracting much attention from researchers as they are the most abundant source of natural polymers and they are biocompatible and biodegradable. Many works devoted to grafting co-monomers such as acrylic acid, acrylamide and polyvinyl alcohol on cellulose derivatives have been carried out to form strongly absorbent polymer materials [5-8]. For example, Suo, et al. [5] synthesized highly water-absorbing carboxymethyl cellulose graft-poly(acrylic acid-co-acrylamide) by free-radical grafting solution polymerization in the presence of N,N'-methylenebisacrylamide as a crosslinker. The highest absorbency obtained was 920 g/g for distilled water, but the superabsorbent can retain 20.7% of the absorbency after heating for 10 h at 60°C in an oven. Pairote, et al. [7] prepared a SAP based on graft copolymerization of sodium carboxymethyl cellulose and acrylic acid with maximum swelling capacities of 544.95 g/g in distilled water and 44.0 g/g in 0.9% w/v NaCl solution. Alam, et al. [8] reported a new cellulose/CMC hydrogel using epichlorohydrin (ECH) as a crosslinker that was able to absorb up to 725 g distilled water/g and 118 g saline water/g.

*Corresponding author: Email: maimophong@gmail.com

However, cellulose-based superabsorbent materials reported to date are evaluated only by the absorbance and release capacity of water and a physiological salt solution in laboratory conditions. In many cases the absorbance and and release of water, as well as salt solutions and agricultural chemicals, in soil conditions have not yet been assessed. In addition, cellulose-based superabsorbent materials are easily broken due to weak gel stability under the pressure of the soil which greatly reduces the water holding capacity of the material. Specifically, the soil load causes a decrease in the water absorption capacity from 338.5 g/g to 19.3 g/g, and prolongs the swelling time [9]. Therefore, when making use of these materials in cultivation, the properties of the material do not reach what is reported in literature, for example, the mechanical durability and, the ability to absorb/release. In general, the material's properties sharply decrease under the pressure of ground conditions and the presence of salt minerals and fertilizer in the soil. Uncontrolled release of water is one of the main factors limiting their application in agriculture. Therefore, the target of this work is to determine the conditions for the synthesis of SAPs materials based on CMC with high water absorption while ensuring consistent gel stability. The BioSAP products are characterized by their properties and their ability to retain water in soil.

Experimental

Materials

CMC with degree of substitution, DS=0.8-0.9, 99.0%, 40-60 mPa.s (1% solution, 25°C) (F04HC, Sunrose), amonium persulfate (APS) 99.9% (Merck), N,N-methylene bisacrylamide (MBA) 99.9% (BioBasic), acrylic acid (AA) 99.6% (Wako), acrylamide (AM) 99.9% (Merck), NaOH 99% (alytical grade from Xilong Chemical), NaCl 99.9% (Merck). Solvents: ethanol and methanol from Xilong Chemical.

Procedure of samples synthesis

CMC aqueous solution is put into a 4-neck flask with a mechanical stirrer, reflux condenser, N_2 gas pipe and thermometer. After neutralizing AA to 65% with NaOH, the solution was mixed with AM (mass ratio AA/AM=6), followed by an addition of MBA. The mixture was then poured into the CMC solution, stirred, and continuously aerated with N_2 for 30 min, then the temperature of the mixture was rised to 40°C before adding the APS solution dropwise. The reaction was carried out at 60°C for 2 h, then the product was chopped and, washed with ethanol and soaked overnight in ethanol before drying for 8 h at 60°C. Raw BioSAP products come in a white opaque powder.

The control sample without CMC (denoted as SAP) was synthesized with the same procedure. The parameters of the samples are given in Table 1.

Table 1. The absorption of distilled water (S_{DW}) of SAP and BioSAP samples with synthetic conditions varies.

Samples	APS, wt.%	MBA, wt.%	CMC, wt.%	S_{DW}, g/g
M1	0.5	0.5	10	49
M2	1.0	0.5	10	193
M3	1.5	0.5	10	147
M4	2.0	0.5	10	141
M5	2.5	0.5	10	121
M6	1.0	0.10	10	311
M7	1.0	0.25	10	333
M8	1.0	0.50	10	193
M9	1.0	0.75	10	145
M10	1.0	1.00	10	110
M11	1,0	0.25	2	200
M12	1.0	0.25	5	220
M13	1.0	0.25	10	333
M14	1.0	0.25	20	259
M15	1.0	0.25	30	215
M16	1.0	0.25	40	210
SAP	1.0	0.25	0	285

Investigation methods

Fourier Transform Infrared spectroscopy (FTIR): the FTIR spectra were recorded on an FTIR-Affinity-1S-Simadzu by KBr disk fabrication technique, 32 scans were performed at 4 cm^{-1} resolution in the range of 600-4000 cm^{-1}.

Determination of gel fraction contents: the gel fraction contents were determined by the Soxhlet technique using acetone as a solvent for 8 h, according to the following formula:

$$G\ (\%) = \frac{m}{m_0}.100$$

where m_0 and m are the mass of samples before and after Soxhlet, respectively.

Determination of liquid absorption: the absorption capacity of the synthesized SAPs and BioSAPs were measured in distilled water, tap water and in saline 0.9 wt% of NaCl using the tea bag method. For the tea bag method, an accurately weighed powdered SAP sample (0.2 g) was placed into a tea bag (acrylic/polyester gauze with fine meshes) and the bag was immersed in an excess amount of water or of another solution (approximately 500 ml) in a standard laboratory (t=25±2°C, relative humidity RH=55±3%). The initial mass of the samples was determined on the analytical balance with 10^{-4} accuracy (m_o). After each designated period, the bag was removed from the solution, allowed to drain for 10 min and the bag was weighted (m_t). This process was repeated several times until the swelling equilibrium was reached (approximately 24 h), i.e. until the bag presented a constant weight.

The liquid absorption of the samples at each time is determined by the formula:

$$S\,(g/g) = \frac{m_t - m_0}{m_0}$$

where m_t and m_0 are the mass of samples absorbed at time *t* and the mass of the original dry samples, respectively. The final absorption of the samples was the average result of determinations.

Determination of water retention under laboratory conditions: samples after water saturation absorption were monitored for the release process at 50°C in an oven. After each designated period, the samples are weighed. Water retention of the samples is determined by the formula:

$$R(\%) = \frac{m_t}{m_0} x100 \quad (1)$$

where m_t and m_o are the water mass of samples at time *t* and initial time, respectively. The experiment was conducted at 50°C and was repeated 3 times.

Determination of water retention in soil: two hundred grams of dried soil mixed with 1 g BioSAP was put into a perforated plastic container at the bottom. The sample was watered until the first drop of water appeared from the bottom of the box. The samples were weighed after each designated period of time. Two hundred grams of control soil sample was prepared with no BioSAP was also performed. The water retention in the soil was calculated using Eq. (1). The experiment was conducted at 25±2°C and was repeated 3 times.

Results and discussion

Study on synthesis conditions of BioSAP

Survey on content of APS catalyst: the samples are prepared with a varying amount of APS (from 0.5 to 2.5%) in the presence of 10% CMC and 0.5% MBA by mass.

From Table 1, when the content of APS increases, the distilled water absorption of BioSAP increases and reaches its largest value at 1%. As the contet of APS continues to increase, the water absorption decreases gradually. This can be explained by the additional free radicals created by increasing APS contents, which increasing the number of grafted hydrophilic polymers onto CMC and, results in increased water absorption [10]. However, when the APS content is too large, an excess amount of free radicals were created, resulting in a reaction that occures too quickly and, a sudden increase in the viscosity of the reaction system. The reaction, therefore quickly ended and hydrophilic polymer short chains were created. The reaction was incomplete, which reduced water absorption [10]. Thus, the optimal APS content was 1 wt.%.

Survey on content of MBA crosslinker: the samples were prepared with a varying amounts of MBA (from 0.1 to 1%) in the presence of 10% CMC and 1% APS by mass.

From Table 1, it can be clearly seen that the distilled water absorption of BioSAP decreases with increasing MBA contents from 0.25 to 1%. The increased MBA contents boosts the number of crosslinks leading to a decrease of three-dimensional network space in the material structure, thus decreasing the water absorption [10, 11]. However, the lower the MBA content, the BioSAP gel is observed to be weaker (low gel strength). This is due to the low MBA content, which weakens the gel structure making, it easier to deform and, unable to hold a large amount of water. Thus, the most suitable content of MBA was 0.25 wt.%.

Survey on content of CMC: the BioSAP samples were prepared with a varying amounts of CMC (from 2 to 40%) in the presence of 1% APS and 0.25% MBA by mass.

From Table 1, it can be seent that, increasing the CMC contents increases the distilled water absorption of BioSAP, which reaches a maximum at 10%. Then further increase

of CMC contents causes the water absorption to decrease gradually. This result can be due to CMC molecules contain many hydrophilic groups such as -OH and -COO^- along the chain length. In addition, CMC chain acts as a framework for grafting polyacrylic acid, polyacrylate and polyacrylamide chains [12], so, the increase of CMC content was increased availability of grafting sites leading to better swelling capacity of the hydrogel. Thus, upon increasing the content of CMC, more space in the material is created and the number of hydrophilic functional groups increases, which leads to an increase in water absorption of materials. Specifically, at CMC 10% wt., the presence of CMC in the material structure significantly increases the water absorption of poly(acrylic acid-co-acrylamide) from 285 up to 333 g/g. This could be due to CMC molecules act as a backbone to make graft copolymers, increase hydgrogel strength, by this helping them retain the structure during the absorbing process to enhance the water absorption ability. So, this result indicated that at this most suitable CMC content seems to provide an interesting compromise between the absorbency and a stable gel structure. However, when furthur increasing the amount of CMC decreases both the water absorption capacity and stable gel. This decreasing could be due to the CMC loading is too high, the CMC acts as a filler that reduces the empty space in the BioSAP for water storage. This result is consistent with previous work reported in the literature [5]. Additionally, the higher of the CMC contents, the BioSAP gel is observed to be weaker (low gel strength) and materials becomes more sticky. In this study, attempts were made to synthesize SAP with CMC contents higher than 40%, but the obtained material dissolved in water when swelling studies were carried out for longer than 48 h. This suggests that, at too high CMC content, there is not enough cross linking density and the formed network is too loose and does not have enough strength to hold water molecules inside the structure. It is known in the literature that CMC increases biodegradability [3, 4], so, depending on the material's requirements for water absorption and self-degradation time, the CMC content can be selected anywhere 10 to 40%. In this work, the main purpose of introduction CMC into superabsorbent is to increase the water absorption while ensuring consistent gel stability, thus, 10% CMC is the most suitable content. This BioSAP material was characterized in terms of chemcial structure and gel fraction content. Its adsorption-desorption behavior in solutions was also studied. Finally, this BioSAP was tested on the water holding capacity in the soil.

The effect of CMC on liquid adsorption-desorption behavior of SAP materials

From Table 1, we can see that the presence of CMC in the material structure significantly increases the water absorption, from 285 up to 333 g/g. The increase in water absorption of the material can be explained by the fact that CMC molecules contain many hydrophilic groups such as -OH and -COO^- along the chain length. At the same time, CMC molecules act as a backbone to make graft copolymers and, increase hydrogel strength by helping them retain their structure during the absorbing process, which enhances the water absorption ability. In addition, the participation of CMC molecules in copolymer macromolecules also increases pore size, leading to an enhanced water absorption capacity of the material [8, 12, 13].

Notably, the presence of CMC significantly increased the absorption capacity of 0.9% NaCl solution in the BioSAP material from 51 up to 69 g/g. These results are shown in Fig. 1. Thus, CMC has increased the 0.9% NaCl solution absorption in SAP materials. It is noteworthy that the obtained product had a significantly higher absorption of 0.9% NaCl solution than other published studies [5-9]. Good water absorption is an important property to the application of this material in the agricultural sector as it helps to increase water absorption in the soil environment.

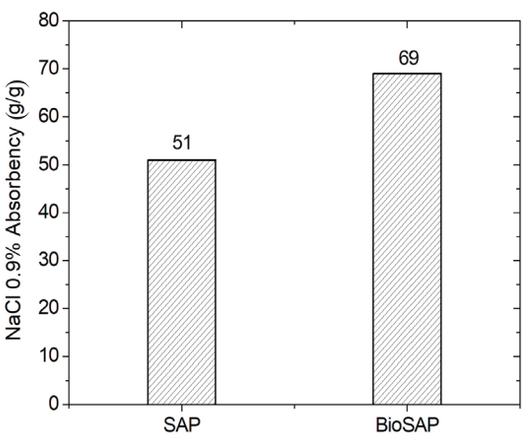

Fig. 1. Absorption of salt solution NaCl 0.9% of BioSAP containing 10% CMC and of SAP.

In this study, the effect of CMC on the desorption behavior of SAP materials is also investigated. The result is shown in Fig. 2.

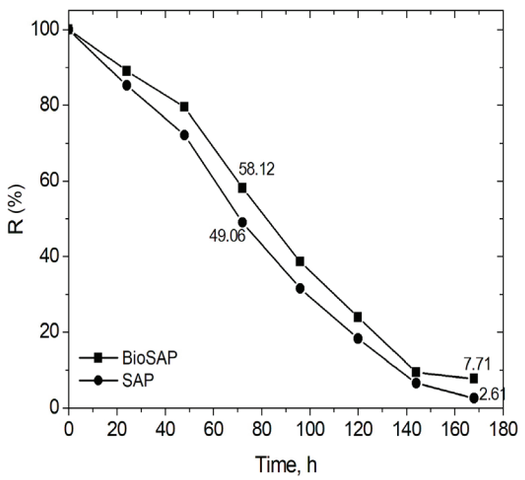

Fig. 2. Water retention of BioSAP and SAP at 50°C.

It can be seen that the presence of CMC reduces the rate of water release of the materials, which implies that CMC increases the water holding capacity. For example, after 72 h at 50°C, the polymer sample containing CMC (BioSAP) held up to 58% of the water absorbed while the sample without CMC (SAP) held only 49%. This may be explained by the presence of a large number of hydrophilic groups such as -OH and -COO^- along the molecular backbone of CMC chains, which form hydrogen bonds with water molecules and reduce the probability of water release in material. Thus, the addition of CMC increases the absorption of water and 0.9% NaCl solution, while also increasing the water holding capacity of these SAP materials.

Characterization of BioSAP

The properties of the BioSAP synthesized in the presence of 1% APS, 0.25% MBA and 10% CMC by weight are studied.

Gel fraction contents: the refinement of raw products has been carried out by the Soxhlet technique, which removes impurities such as water-soluble homopolymers, oligomers, residual monomers, catalysts, and others. The gel fraction of the products reached 98.5%. The saturated absorption of distilled water (S_{DW}), tap water (S_{TW}), and 0.9% NaCl solution (S_{NaCl}) of the raw and refined products are given in Table 2.

Table 2. Saturated absorption of BioSAP samples.

Samples	S_{DW}, g/g	S_{TW}, g/g	S_{NaCl}, g/g
Raw BioSAP	333	163	59
Refined BioSAP	406	295	69

The results of Table 2 showed that the refined BioSAP samples have a significantly higher absorption for all the media tested. Therefore, refinement of the products after synthesis is very important. The absorption of tap water and 0.9% NaCl solution is significantly lower than that of distilled water, proving that the presence of metal ions has a great influence on the water absorption capacity of the BioSAP materials.

FTIR Spectrum: the FTIR spectra of the SAP and BioSAP samples are shown in Fig. 3.

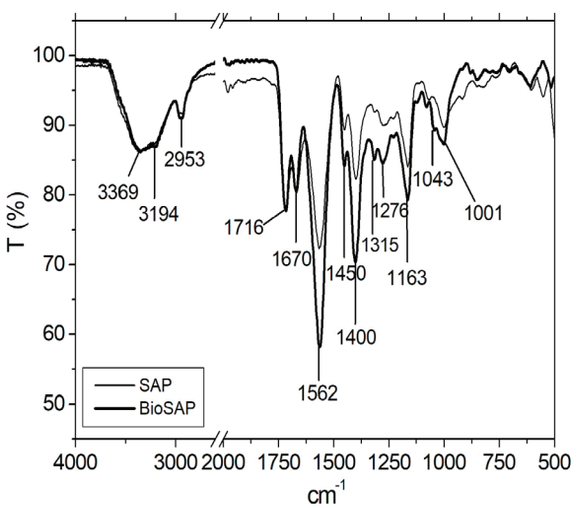

Fig. 3. FTIR spectrum of SAP and BioSAP samples.

As can be seen, from the FTIR spectra of the BioSAP, peaks appearing at 3369 cm^{-1} and 3194 cm^{-1} are typical for the valence vibrations of the O-H and N-H bonds, respectively, and the peak at 2953 cm^{-1} represents the valence vibrations of C-H bonds. The appearance of peaks at 1716 cm^{-1}, and 1670 cm^{-1} characterize the vibrations of the C=O bonds of acids and amides, respectively. In particular, the peak at 1562 cm^{-1} is typical for a sodium carboxylate salt [5-7]. The peaks at 1400 cm^{-1}, 1315 cm^{-1}, and 1276 cm^{-1} characterize the vibrations of the C-N, C-H, and C-C bonds, respectively. The increase in peak intensity of BioSAP compared to SAP at 1562 cm^{-1}, 1163 cm^{-1}, and 1001 cm^{-1} in the FTIR spectrum is due to the appearance of the C=O bonds of carboxylmethyl groups, and the C-O-C bonding bridge between the glucoside rings and CH-β-glycoside of CMC [12, 13]. Thus, analysis of FTIR spectrum demonstrate the presence of CMC in the structure of BioSAP.

Test on the water holding capacity of BioSAP in soil

To assess the water holding capacity of BioSAP in soil, water retention and slow release tests were conducted and, the results are shown in Table 3 and Fig. 4.

It can be seen from Table 3 that the volume of water retained in the soil samples containing BioSAP is almost 3 times greater than that held in soil samples without BioSAP.

Table 3. Water retention of soil samples with and without BioSAP.

Samples	m_{BioSAP},g	m_{soil},g	m_{water},g
Soil with BioSAP	1.0	200±0.1	105±4.6
Soil without BioSAP	0.0	200±0.1	36±2.6

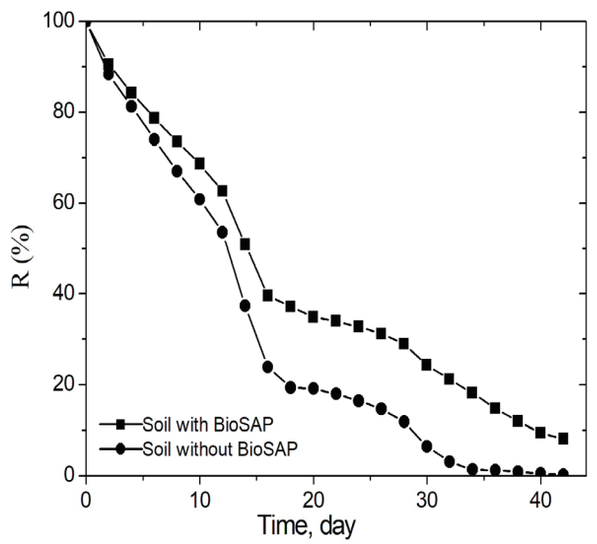

Fig. 4. Water retention in soil with and without 0.5% BioSAP by mass.

As can be seen from Fig. 4, soil samples containing 0.5% BioSAP have a significantly higher ability of water retention than the soil samples without BioSAP. Over the first 6 days, the amount of water decreased sharply and, then decreased gradually. After 10 days, samples with BioSAP could still hold 41.6% of water, while samples without BioSAP could only hold 23.8%. After 28 days, the water in the soil sample without BioSAP had completely evaporated, while the soil sample with BioSAP still retained nearly 20%. This proves that BioSAP improved the soil's ability to hold and release water slowly. Notably, the water retention and slow release capacity of our BioSAP products are significantly higher than that of other published studies [2, 3, 9].

Conclusions

- The effect of the content of catalyst, crosslinker and CMC on the water absorption capacity of SAP and BioSAP was examined. The results showed that the materials reached maximum absorption under the reaction conditions of 1% APS, 0.25% MBA, and 10% CMC by weight. The ratio of AA/AM=6 (AA was neutralized up to 65% by NaOH solution). The absorption of the product with distilled water and 0.9% NaCl solution was found to be 406 and 69 (g/g), respectively.

- The presence of CMC significantly increased not only water absorption, but also the water retention of the SAP materials, and in particular, significantly increased the absorption of 0.9% NaCl solution.

- Using 0.5% soil volume of BioSAP as a soil moisturizer significant increase in water retention and the ability to slowly release water from the soil was found. Therefore, SAP materials containing CMC have specific improved properties which help to increase water absorption in the soil environment and gives these BioSAP materials promising applications for agriculture.

ACKNOWLEDGEMENTS

The work is implemented by funding from a potential project, National Science and Technology Development Fund, NAFOSTED, code: 06/2019/TN.

The authors declare that there is no conflict of interest regarding the publication of this article.

REFERENCES

[1] A. Waleed (2018), "Impact of hydrogel polymer in agricultural sector", *Adv. Agr. Environ. Sci*., **1(2)**, pp.59-64.

[2] C. Demitri, F. Scalera, M. Madaghiele, A. Sannino, A. Maffezzol (2013), "Potential of cellulose based superabsorbent hydrogels as water reservoir in agriculture", *Hindawi*, DOI:10.1155/2013/435073.

[3] F.F. Montesano, A. Parente, P. Santamaria, A. Sannino, F. Serio (2015), "Biodegradable superabsorbent hydrogel increases water retention properties of growing media and plant growth", *Agric. Agric. Sci. Procedia*, **4**, pp.451-458.

[4] J.D. Stahl, M.D. Cameron, J. Haselbach, S.D. Aust (2000), "Biodegradation of duperabsorbent polymers in soil", *Environ. Sci. & Pollut. Res*., **7(2)**, pp.83-88.

[5] A. Suo, J. Qian, Y. Yao, and W. Zhang (2007), "Synthesis and properties of carboxymethyl cellulose-graft-poly (acrylic acid-co-acrylamide) as a novel cellulose based superabsorbent", *J. Appl. Polym. Sci.*, **103(3)**, pp.1382-1388.

[6] A. Pourjavadi, H. Ghasemzadeh and F. Mojahedi (2009), "Swelling properties of CMC-g-poly(AAm-co-AMPS) superabsorbent hydrogel", *J. Appl. Polym. Sci.*, **113(6)**, pp.3442-3449.

[7] K. Pairote, K. Patchareeya (2017), "SAP based on sodium carboxymethyl cellulose grafted polyacrylic acid by inverse suspension polymerization, synthesis and property of SAPs modified by carboxymethyl cellulose", *Inter. J. Polym. Sci.*, DOI:10.1155/2017/3476921.

[8] M.N. Alam, M.S. Islam, L.P. Christopher (2019), "Sustainable production of cellulose-based hydrogels with superb absorbing potential in physiological saline", *ACS Omega*, **4(5)**, pp.9419-9426.

[9] K. Lejcus´, M. Spitalniak, J. Da¸Browska (2018), "Swelling behaviour of SAPs for soil amendment under different loads", *Polym.*, **10(271)**, DOI:10.3390/polym10030271.

[10] E.M. Ahmed (2015), "Hydrogel: preparation, characterization and applications: a review", *J. Adv. Res.*, **6**, pp.105-121.

[11] H.V. Chavda, C.N. Patel (2011), "Effect of crosslinker concentration on characteristics of superporous hydrogel", *Inter. J. Pharm. Inves.*, **1(1)**, pp.17-21.

[12] L.P. Álvarez, L.R. Rubio, E. Lizudia, J.L.V. Vilela (2018), "Polysaccharide-based superabsorbents: synthesis, properties, and applications", *Cellulose-Based Superabsorbent Hydrogels*, pp.1393-1431.

[13] S.M.F. Kabir, P.P. Sikdar, B. Haque, A.R. Bhuiyan, A. Ali, M.N. Islam (2018), "Cellulose based hydrogel materials: chemistry, properties and their prospective applications", *Progress in Biomaterials*, **7**, pp.153-174.

DOI: 10.31276/VJSTE.62(3).33-37

One-step synthesis and performance evaluation of zinc metavanadate pigments as highly anticorrosive primers

Dang Quang Vinh Nguyen, Tien Khoa Le, Thi Thanh Thuy Nguyen*

University of Science, Vietnam National University, Ho Chi Minh city

Received 18 December 2019; accepted 17 March 2020

Abstract:

Recently, the vanadate species have been considered as promising inhibitor agents used for metal protection. Various metallic materials were treated in a vanadate solution in order to form a passivation coating. However, the use of solid vanadate compounds as inhibitor pigments in the formulation of anticorrosive primers is still limited. Therefore, in this work, solid zinc metavanadate pigments for application in paint primers were prepared by a simple route at various pH values and concentrations of monovanadate. According to the results, all samples showed a characteristic hexagonal structure with high anticorrosive abilities. Both the pH and monovanadate concentration strongly affected the morphology, the particle size, and the anti-corrosion power. Among the prepared samples, the best anticorrosive pigment was the sample prepared at pH 8 with a vanadate concentration of 0.2 M.

Keywords: **anticorrosive pigment, electrochemical impedance, primers, steel plate, Zinc metavanadate.**

Classification number: **2.2**

Introduction

Due to the planet's oxidizing atmosphere, metal corrosion is considered one of the most severe problems across various industries and causes not only material destruction but also tremendous economic damages. Over the past few decades many anti-corrosion methods have been proposed, which can be divided into two groups: active corrosion protection and passive corrosion protection. The former mechanism is based on the fabrication of corrosion-resistant alloys and the application of inhibitors on the metallic surface, whereas the latter mechanism relies on the development of coating films that isolate the underlying metal from its corrosive environment [1, 2]. In fact, corrosion can be effectively and economically prevented by using suitable anti-corrosion coatings. Among the available coating materials, chromate coatings have been widely used to passivate steel, aluminum, and other metals. Chromate was also used as an inhibitive pigment in the formulation of protective paint [3, 4]. However, due to the presence of hexavalent chrome, this type of coating and pigment is highly toxic and carcinogenic [3-7]. Thus, it is exceedingly necessary to develop novel materials that are both adequately anti-corrosive and environmentally benign [8, 9].

Recently, various works have proved that vanadate ions can play as an alternative coating for the protection of steel, aluminum alloy or Mg-Zn alloys [10-13]. In these studies, the metallic surface was treated in $NaVO_3$ solution with different concentration of vanadate ion and different pH values. For example, when zinc foil was dipped in an aqueous solution of $NaVO_3$ (4 mM), a polymerized vanadate film was successfully formed on the metallic surface [12], which can cause the two-order magnitude decrease in corrosion current density. Likewise, Feng, et al. (2018) [13] successfully created a dense vanadate film on the surface of AZ31 Mg alloy by immersing this alloy in the 4 mM solution of $NaVO_3$ at pH 7.7-9.2. Owing to this vanadate film, the

*Corresponding author: Email: ntthuy@hcmus.edu.vn

corrosion current density was dramatically decreased while the breakdown potential was effectively increased. In the presence of the vanadate film, the corrosion current density was dramatically decreased. It was also observed that the variation of vanadate concentration and solution pH may result in various types of vanadate ions, affecting the corrosion inhibition of coating films. In his work, Frankel noticed that the anti-corrosion power of metavanadate coating is better than decavanadate coating for the protection of Al alloy [14]. Moreover, when the vanadate concentration increased from 0.1 to 4.15 mM, the corrosion current density was found to be declined, proving that the concentration of vanadate plays an important role for the development of protective layers. Especially, Morks, et al. (2012) [10] proposed to embed Na_3VO_4 in a modified zinc phosphate coating with Mn-Mg additives. At the vanadate concentration of 10^{-3} M and the pH of 4, the inhibition efficiency for pipeline steel of this as-prepared coating can reach 99%.

These previous works have shown that vanadate is a promising inhibition agent for metal protection. However, up to now, the use of solid vanadate compounds as inhibitor pigments in the formulation of anticorrosive primers is still limited. There are only several papers reporting the application of ion-exchangeable pigments based on hydrotalcite/vanadate [15, 16] to passivate low carbon cold rolled steel plates. On the other hand, the solid vanadate compounds prepared by solid-state reactions or hydrothermal methods have been usually applied as catalysts [17, 18] for oxidation reactions or antibacterial additives [19]. Therefore, in this work, we proposed to synthesize solid zinc metavanadate pigment by using a simple precipitation method at various pH values and concentrations of vanadate in order to form anticorrosive paint primers for steel plates.

Experimental

Preparation of zinc vanadate

The starting materials, $ZnSO_4.7H_2O$, NH_4VO_3 and NaOH (≥97%, reagent grade), were purchased from Guanghua Sci-tech (Guangdong, China). These chemicals were used as received without further purification. Firstly, NH_4VO_3 was dissolved into distilled water to form the metavanadate solutions with various monovanadate concentrations (0.1, 0.2 and 0.5 M) and the pH of these solutions was adjusted to 6, 8, or 10 by NaOH solution. Then a $ZnSO_4$ solution was slowly added to the above NH_4VO_3 solutions under continuous magnetic stirring. The mixed solutions were magnetically stirred for 1 h. After that, the pigment products were filtered, washed with distilled water, and finally dried at 80°C for 2 h. In this manuscript, the samples are labelled as in Table 1.

Table 1. Synthesis conditions of pigment samples.

Samples	$ZnSO_4$ solution	NH_4VO_3 concentration	pH of NH_4VO_3 solution
ZV-5.8	1 M	0.5 M	8
ZV-2.6	1 M	0.2 M	6
ZV-2.8	1 M	0.2 M	8
ZV-2.10	1 M	0.2 M	10
ZV-1.8	1 M	0.1 M	8

Characterization

The structure and phase composition of our pigments were characterized by powder X-ray diffraction (XRD) on a D8-ADVANCE (BRUKER) using Cu K_α radiation with an accelerating voltage of 40 kV and an applied current of 40 mA. The XRD patterns were recorded from 10 to 70°. The morphology and particle size were investigated by field emission scanning electron microscopy (FESEM) on a S4800 (HITACHI, Japan) with an accelerating voltage of 10 kV.

Electrochemical impedance measurements

Pigments with a total mass of 0.25 g were dispersed into 250 ml of NaCl 3.5% w/w solution and magnetically stirred for 24 h. Then, the solid pigments were removed from the solution to obtain the leaching solutions. Meanwhile, steel plates (2.5×5 cm) were surface-treated and afterwards covered by insulating tape leaving only a surface with the area of 1 cm^2. These steel plates were immersed in the leaching solutions and the electrochemical impedance was measured versus time by using a Versastat 3 with 3 electrodes: the treated steel plates as working electrode, the silver electrode as reference electrode, and the platinum electrode as the counter electrode. For comparison, steel plates were immersed in a 3.5% w/w NaCl solution without monovanadate and their electrochemical impedance was also measured on a Versastat 3 (AMETEK Scientific Instruments).

Corrosion resistance of zinc vanadate pigments on steel

Firstly, 0.50 g of zinc monovanadate pigment was dispersed in a mixture containing 30.0 ml of commercial epoxy paint and solidifier. The painting mixture was subsequently applied on the surface of the steel plates (2.5×8 cm) that were previously surface-treated. After that, the steel plates were exposed to ambient atmosphere for 40 h in order to dry the paint coating. Finally, the steel plates were dipped into the NaCl 3.5% solution for 480 h to investigate their corrosion resistance. The blank sample

(without zinc monovanadate pigment) was also immersed in the NaCl solution for comparison. The steel plates coated with the paint mixture containing zinc monovanadate were also exposed to air at 30°C for 480 h to test their corrosion resistance in atmosphere.

Results and discussion

Crystal structure and morphology

Figure 1 presents the XRD patterns of the zinc monovanadate samples prepared with different monovanadate concentrations and different pH values. According to these patterns, all samples revealed the presence of the α-$Zn_3(VO_4)_2$ hexagonal phase (space group of P-6) identified by the characteristic diffraction peaks at 12.2, 16.6, 20.6, 29.5, 31.4, 33.5, 35.6, 41.6, 50.3, and 60.9°, which is the same as the results of D.A.H. Ayala, et al. (2001, 2002) [20, 21]. When both the concentration of monovanadate and the solution pH increase, the XRD baselines become less stable and the diffraction peaks become asymmetrical, which indicates the decrease in crystallinity in these samples.

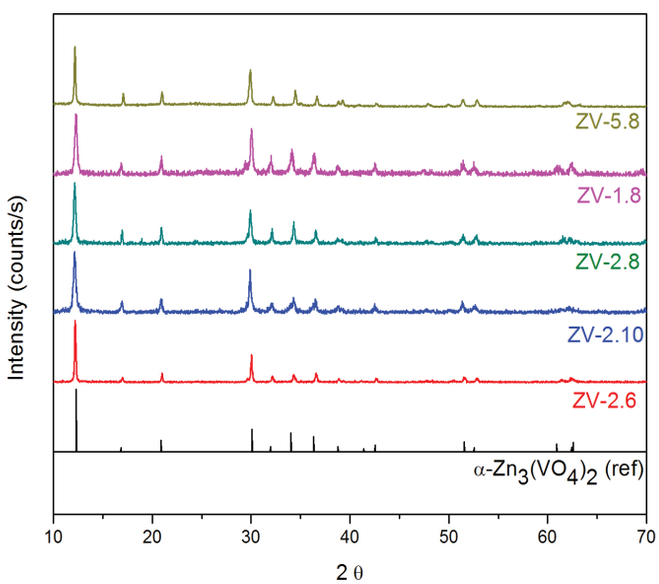

Fig. 1. XRD patterns of ZV samples.

Figure 2 presents the FESEM images of the pigment samples. It was observed that all samples were composed of multi-dispersed particles. For the samples prepared with low monovanadate concentrations (0.1 M and 0.2 M), the particles were tabular in shape with the particle size varying from 10 to 40 nm. When the monovanadate concentration was up to 0.5 M, the particle size greatly increased (100-2000 nm) with the appearance of very large polyhedral particles. The pH values of the NH_4VO_3 solutions also affect the morphology of zinc monovanadate pigments. At a monovanadate concentration of 0.2 M and pH of 6, the particle size can reach 1000 nm whereas at pH 8, the particle size decreases to 320 nm. Furthermore, the pigment particles of the ZV-2.8 sample were found to be more homogeneous in size than in other samples.

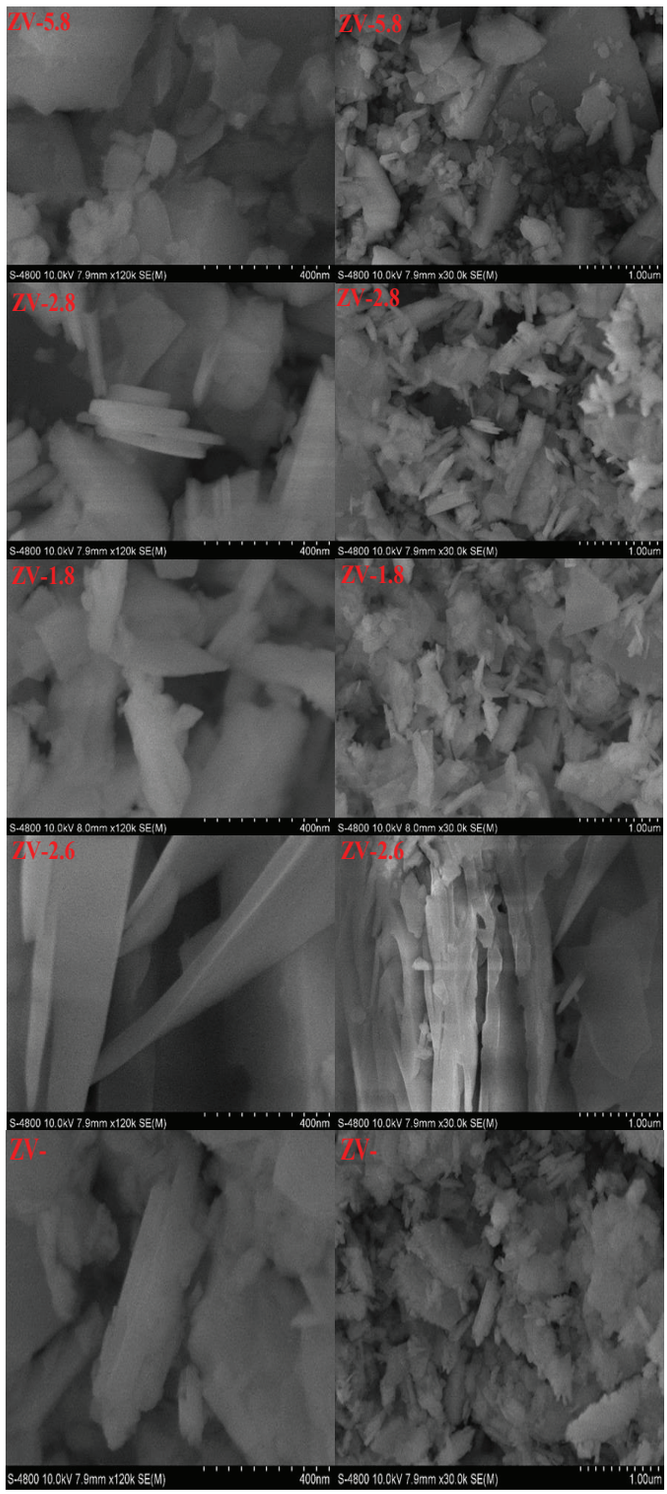

Fig. 2. SEM images of the ZV samples.

Table 2. The pH and electric conductivity values of pigment leaching solutions after 24 h in NaCl 3.5% solution.

	NaCl 3.5% w/w solution	ZV-5.8	ZV-2.8	ZV-1.8	ZV-2.6	ZV-2.10
pH	6.035	7.012	6.964	6.991	6.984	7.033
Electric conductivity (µS/cm)	53523.0	54217.9	54108.3	54303.4	53687.6	53985.4

It should be noted that the evolution of particle size and particle shape in our samples did not modify the pH or the electric conductivity of leaching solutions. Due to hydrolysis of the monovanadate ions, all the leaching solutions showed a higher pH and conductivity than that of the NaCl 3.5% w/w solution (Table 2).

Electrochemical impedance results

For all the steel plates, the electrochemical impedance values, Z, decreased with soaking time in the leaching solution, indicating that the corrosion of steel takes place over time (Fig. 3). Nevertheless, at the same time interval, the steel plates immersed in the leaching solution of zinc monovanadate pigments always showed higher impedance values than the blank sample. In addition, the decreased rate of impedance with time of the steel plates in ZV leaching solutions was lower than that of blank sample. Hence, we can confirm that the ZV pigments can help protect the surface of the steel plates. Moreover, in the leaching solution prepared from a low concentration of NH_4NO_3, the steel plates did not only show a high impedance but also presented a slow decrease in impedance values. Likewise, when the pH of the monovanadate solution rose from 6 to 8 and 10, the impedance value tended to increase and the evolution of the impedance versus time slowed down. These results suggest that the tabular shape and the particle size of 300-400 nm seem to be the most important factors to enhance the anti-corrosion power of zinc monovanadate particles.

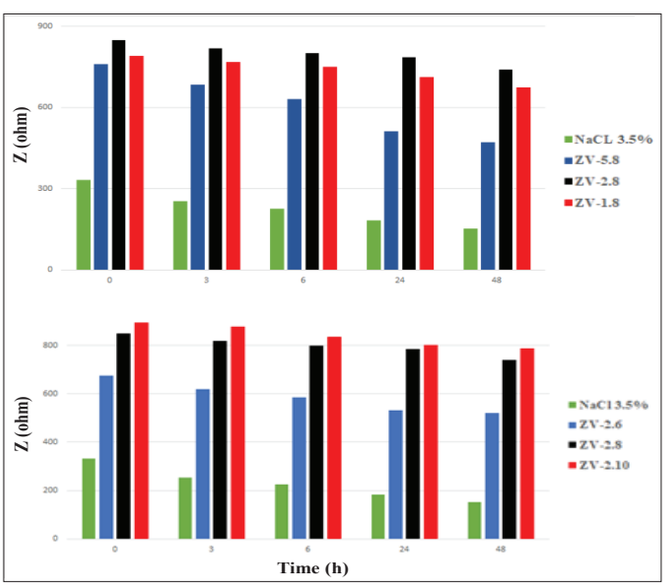

Fig. 3. The electrochemical impedance at 0.01 Hz as a function of immersion time in ZV extracts.

Corrosion resistance of zinc vanadate pigments coated on steel

According to Fig. 4A, after 480 h in NaCl 3.5% w/w solution, all the samples, including the blank sample and the steel plates coated with ZV-containing paints, suffered from corrosion that clearly occurred at their margins. Especially, corrosion strongly occurred at some spots on the surface of the blank sample. It was observed that the steel plates using ZV-2.6 and ZV-2.10 pigments in the primer also suffered from corrosion in a similar way to the blank sample. Among the samples, the steel plates using ZV-2.8 and ZV-1.8 pigments showed the best corrosion resistance in the NaCl solution.

In ambient atmosphere, all the steel plates coated with ZV-containing paints were less corrosive than the blank sample (Fig. 4B). The steel plates using ZV-2.8 and ZV-1.8 pigments were still the best anti-corrosive samples. However, the remaining samples showed several spitting areas on the surface, proving that the paint-containing ZV particles prepared under other conditions did not adhere well to the metallic surface. Thus, it can be stated that a monovanadate concentration of 0.2 M and pH of 8 were the optimal conditions to prepare zinc monovanadate pigments with high anti-corrosive power in this work.

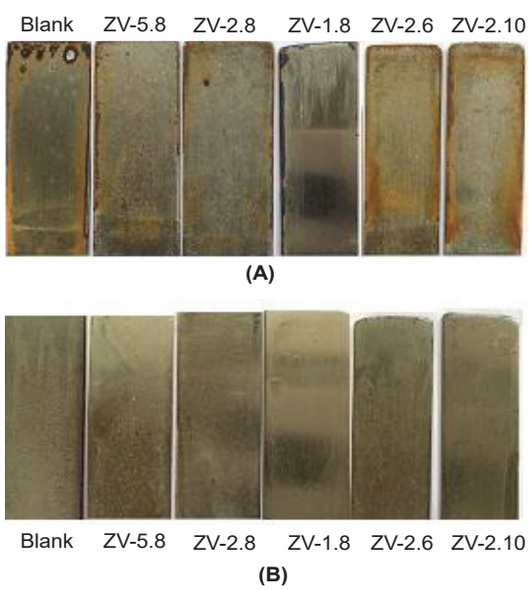

Fig. 4. Steel plate surfaces with primer paint after 480 h in (A) NaCl 3.5% solution and (B) ambient atmosphere.

Conclusions

In this work, we successfully prepared zinc monovanadate particles as inhibitor pigments used in the formulation of anticorrosive primers. When mixed with primer painting components, these pigments provided beneficial corrosive resistance for steel plates. The experimental results also demonstrated the influences of pH and starting concentration of NH_4VO_3 on the crystal structure, morphology, and anti-corrosive power of the pigments. Among all the samples, the pigments prepared with a monovanadate concentration of 0.2 M and pH of 8 show the best anti-corrosive performance for steel plates in both ambient atmosphere and NaCl solution.

ACKNOWLEDGEMENTS

This research is funded by University of Science, Vietnam National University, Ho Chi Minh city, under grant number T2018-12.

The authors declare that there is no conflict of interest regarding the publication of this article.

REFERENCES

[1] C. Verma, E.E. Ebenso, M.A. Quraishi (2017), "Corrosion inhibitors for ferrous and non-ferrous metals and alloys in ionic sodium chloride solutions: a review", *J. Mol. Liq.*, **248**, pp.927-942.

[2] S.B. Ulaeto, R. Rajana, J.K. Pancreciousa, T.P.D. Rajana, B.C. Pai (2017), "Developments in smart anticorrosive coatings with multifunctional characteristics", *Prog. Org. Coat.*, **111**, pp.294-314.

[3] S.A. Katz, H. Salem (1993), "The toxicology of chromium with respect to its chemical speciation: a review", *J. Appl. Toxicol*., **13(3)**, pp.217-224.

[4] S. Langård, T. Norseth (1975), "A cohort study of bronchial carcinomas in workers producing chromate pigments", *Br. J. Ind. Med*., **32(1)**, pp.62-65.

[5] R.G. Buchheit, H. Guan, S. Mahajanam, F. Wong (2003), "Active corrosion protection and corrosion sensing in chromate-free organic coatings", *Prog. Org. Coat.*, **47(3-4)**, pp.174-182.

[6] N. Granizo, J.M. Vega, D. de la Fuente, J. Simancas, M. Morcillo (2012), "Ion-exchange pigments in primer paints for anticorrosive protection of steel in atmospheric service: cation-exchange pigments", *Prog. Org. Coat.*, **75(3)**, pp.147-161.

[7] L. Fachikov, D. Ivanova (2012), "Surface treatment of zinc coatings by molybdate solutions", *Appl. Surf. Sci.*, **258(24)**, pp.10160-10167.

[8] S. Alinejad, R. Naderi, M. Mahdavian (2016), "The effect of zinc cation on the anticorrosion behavior of an eco-friendly silane sol-gel coating applied on mild steel", *Prog. Org. Coat.*, **101**, pp.142-148.

[9] M. Zubielewicz, W. Gnot (2004), "Mechanisms of non-toxic anticorrosive pigments in organic waterborne coatings", *Prog. Org. Coat.*, **49,** pp.358-371.

[10] M.F. Morks, P.A. Corrigan, I.S. Cole (2012), "Mn-Mg based zinc phosphate and vanadate for corrosion inhibition of steel pipelines transport of CO_2 rich fluids", *Int. J. Greenhouse*, **7**, pp.218-224.

[11] L. Niu, S.H. Chang, X. Tong, G. Li, Z. Shi (2014), "Analysis of characteristics of vanadate conversion coating on the surface of magnesium alloy", *J. Alloy Compd*., **617**, pp.214-218.

[12] B.L. Hurley, K.D. Ralston, R.G. Buchheit (2014), "Corrosion inhibition of zinc by aqueous vanadate species", *J. Electrochem. Soc*., **161(10)**, pp.C471-C475.

[13] Z. Feng, B. Hurley, J. Li, R. Buchheit (2018), "Corrosion inhibition study of aqueous vanadate on Mg Alloy AZ31", *J. Electrochem. Soc*., **165(2)**, pp.C94-C102.

[14] M. Iannuzzi, T. Young, G.S. Frankela (2006), "Aluminum alloy corrosion inhibition by vanadates", *J. Electrochem. Soc*., **153(12)**, pp.B533-B541.

[15] J.M. Vega, D. de la Fuente, B. Chico, M. Morcillo, N. Granizo (2013), "Ion-exchange pigments in primer paints for anticorrosive protection of steel in atmospheric service: anion-exchange pigments", *Prog. Org. Coat.*, **76**, pp.411-424.

[16] N. Granizo, J.M. Vega, I. Díaz, B. Chico, D. de la Fuente, M. Morcillo (2011), "Paint systems formulated with ion-exchange pigments applied on carbon steel: effect of surface preparation", *Prog. Org. Coat.*, **70**, pp.394-400.

[17] H. Sameie, A.A.S. Alvani, N. Naseri, S. Du, F. Rosei (2018), "First-principles study on ZnV_2O_6 and $Zn_2V_2O_7$: two new photoanode candidates for photoelectrochemical water oxidation", *Ceram. Int.*, **44(6)**, pp.6607-6613.

[18] L.Z. Pei, N. Lin, T. Wei, H.D. Liu, H.Y. Yu (2015), "Zinc vanadate nanorods and their visible light photocatalytic activity", *J. Alloys. Compd*., **631**, pp.90-98.

[19] A.S.K. Heer (2017), "Simple and direct synthesis of zinc vanadate (ZnV_2O_5) nanocrystals for its electrocatalytic and antimicrobial activity", *J. Chem. Pharm. Res.*, **9(12)**, pp.18-24.

[20] D.A.H. Ayala, A. Echavarria, C. Saldarriaga (2001), "Synthesis and structure of a porous zinc vanadate, $Zn_3(VO_4)_2.3H_2O$", *J. Mater. Sci.*, **36**, pp.5515-5518.

[21] D.A.H. Ayala, A. Echavarria, L.A. Palacio, C. Saldarriaga (2002), "Structural characterization of a porous zinc vanadate: $Zn_3(VO_4)_2.3H_2O$", *Powder Diffr.*, **17(4)**, pp.320-321.

DOI: 10.31276/VJSTE.62(3).38-44

Modelling of insulation in DC systems: the challenges for HVDC cables and accessories

Vu Thi Thu Nga*, Gilbert Teyssedre[2]

[1]*Electric Power University, Hanoi, Vietnam*
[2]*Laplace, CNRS and University of Toulouse, France*

Received 13 September 2019; accepted 25 December 2019

Abstract:

Cable technologies have evolved in different ways for applications using high voltage alternating current (HVAC) and high voltage direct current (HVDC) over the last 40 years. Since the 1950s, mass-impregnated paper was progressively replaced by extruded insulation made of polyethylene and then cross-linked polyethylene (XLPE). The switch from paper insulation to extruded cables went on continuously while cables were designed with ever increasing voltage requirements. However, regarding space charge build-up and field redistribution, particularly at polarity reversal stages in thyristors, the behaviour of extruded cables under such DC stress is not fully understood. For this reason, material improvement, characterization, and modelling are still intensively researched for cables, accessories, and power conversion equipment. The weaknesses and methods used to simulate the characteristics of insulation are presented and compared in this work through the simulation results of the macroscopic and fluid model.

Keywords: **DC systems, fluid model, HVDC.**

Classification number: **2.3**

Introduction

HVDC technologies remain a growing part of energy transmission systems owing to the new sources of energy being introduced, especially renewable energy, and to the need for strengthening energy networks while focusing on the de-carbonation of energy.

There are converging favourable conditions for the development of HVDC links for energy transmission, notably the development of large electrical power lines over long distances to link production and consumption areas and to interconnect different networks with ever growing size. HVDC can also be used in replacement of HVAC lines for transmitting more power over a spatially constrained infrastructure. The demand for HVDC lines has diverse origins, namely, submarine cables, urban areas, and strong public opposition of overhead lines. The switch from HVAC to HVDC systems has great advantages such as simplification of manufacture (Fig. 1) and virtually no limit on transmission length owing to the fact that compensation of the capacitive current is no longer a necessity. Therefore, materials used for the insulation of HVDC cables require specific properties, notably regarding conductivity behaviour. Aside from that, its space charge behaviour is something that is carefully considered at the material characterization level (as samples), as well as in a full cable configuration. The amount of charges is something that can be relatively well characterized, however, the criteria for the kinetics of charge release and the behaviour of materials at polarity reversal are not so well-defined [1]. A slow relaxation of charges implies that, at polarity reversal, the residual field will add to the applied field. Therefore, the objective of this work is the analysis of the weaknesses and methods used to simulate the characteristics of insulation in cables and accessories under DC electro-thermal stress.

*Corresponding author: Email: ngavtt@epu.edu.vn

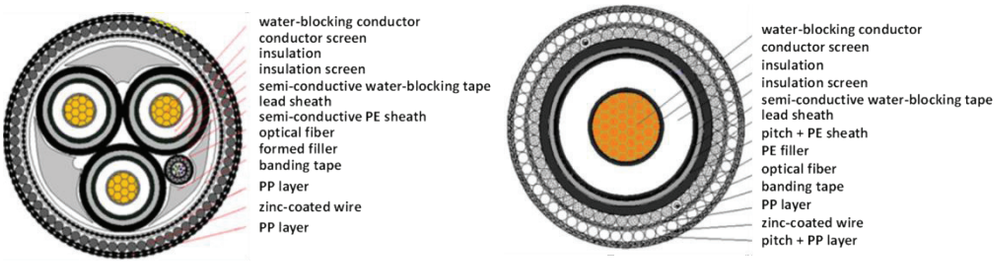

(A) **(B)**

Fig. 1. Examples of structures of HV submarine cables rated for 200 MW. Weight reduced by over 60% [2]. **(A)** 3-core HVAC 110 kV cable; outer diameter 193 mm; **(B)** +/- 160 kV HVDC cable; outer diameter 111 mm.

Threats for insulation withstanding in HVDC cables

As mentioned above, one of the threats to insulation under HVDC stress is the build-up of space charges in the insulation and its impact on the field distribution, along with the energy released when charges are redistributed upon fast-varying voltage. The weaknesses of polymers with respect to mass-impregnated paper can be found in their lower thermal conductivity and higher electrical resistivity, such that charge release is slower. For example, in mineral insulated (MI) cables, trapped space charge accumulation is considered insignificant [3]. Also, the maximal designed thermal stress is 55°C for MI-paper while it is 90°C for XLPE, at least under AC stress.

The major difference between HVAC and HVDC stress is the change from a capacitive distribution of the field to a resistive distribution; as even under DC there is a progressive switch from capacitive to resistive field distribution at each stress level. Under operating conditions, the electric field is not homogeneous along the cable radius and a thermal gradient exists along the radius due Joule losses from the circulating current in the conductor. As the resistivity of the insulation is much more dependent on the temperature and electric field than it is the permittivity, the thermal-electric stress rating in an HVDC cable is trickier to achieve. Under steady-state HVDC, the phenomenon of stress inversion occurs; i.e. the electric field becomes higher at the outer semiconducting screen than at the inner one (near the conductor) due to the lower temperature. Hence, lower electrical conductivity is found at the outer screen. An example of such stress inversion is represented in Fig. 2 for a medium voltage cable under a thermal gradient of 30°C as modelled by a realistic law for the electric conductivity of polyethylene insulation [4] given by:

$$\sigma(T,E) = A \cdot exp\left(\frac{-E_a}{k_B T}\right) \cdot sinh(B(T) \cdot E) \cdot E^{\alpha} \quad (1)$$

where A and α are constants, E_a is the thermal activation energy, k_B is Boltzmann's constant, E is the applied electric field, T is the temperature, and $B = aT+b$ is a temperature-dependent parameter to account for the change in threshold field versus temperature. It can be seen that the field initially exhibits a capacitive distribution; after 1000 s it is relatively homogeneous and after 1 h or so, the field is a maximum at the outer shield. The switch from capacitive to resistive field distribution is controlled by the dielectric time constant, ε/σ, where ε is the dielectric permittivity. When the polarity is reversed, which is usually done over a time much faster than the dielectric time constant, the residual electric field at the inner conductor constitutes an enhancement to the capacitive field and this local and transient enhancement of the field brings harmfulness to the cables.

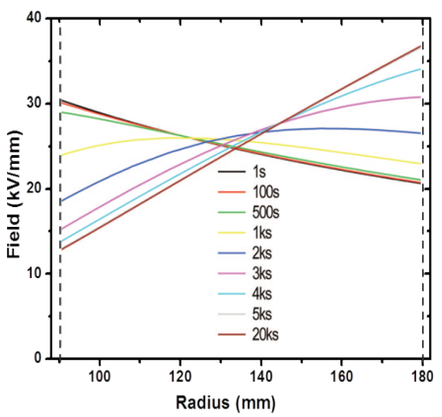

Fig. 2. Example of field redistribution vs. time and stress inversion under DC stress for a MV cable. Adapted from [5]. Parameters of equation (1) are: A=3.68×10^{7} S•m/V, E_a=0.98 eV, B=1.086×10^{-7} S•m/V and α=1. A temperature drop of 30°C across the insulator and a temperature of 80°C at the inner conductor are considered.

From the assumption on the temperature dependence of conductivity, using Maxwell's equation, it can be shown that the electric field distribution in the cable insulation, in cylindrical geometry and under steady state condition is given by expression [6, 7]:

$$E(r) = E_0 \frac{r_0 \sigma_0}{r\sigma(r)} \quad (2)$$

where E_0 and σ_0 are, respectively, the electric field and conductivity at the reference position, r_0. The charge density associated with non-uniform conductivity is of the form:

$$\rho_g(r) = div(\varepsilon \cdot E) = -E(r)\frac{\varepsilon}{\sigma(r)}\frac{\partial\sigma(r)}{dr} \quad (3)$$

where ε is the dielectric permittivity of the material. If the temperature dependence of the conductivity follows the Arrhenius law with activation energy E_a, the charge density can be written according to the following equation:

$$\rho_{tg}(r) = -\varepsilon . E(r)\frac{E_a}{k_B T^2}\frac{dT}{dr}, \quad (4)$$

where T is the absolute temperature, which is function of r and time, t [8]. It can be noticed from Eqs. (3) and (4) that the space charge polarity directly depends on the conductivity gradient $d\sigma/dr$.

The sign of the space charge, $\rho_g(r)$, is the same as the polarity of the voltage applied to the conductor. Such space charge is normally detected by experimental techniques that provide the charge distributions. Such a geometric space charge is also detected when dielectrics of different natures become associated, as in joints and terminations of cables. These junctions may correspond to a gradient of permittivity, or more likely, to a gradient of conductivity [9, 10]. We have shown that such an interfacial charge - or macroscopic Maxwell-Wagner effect - can be probed by the space charge measurement method. Depending on temperature and field values, the field can be a maximum in one or the other dielectric. Also, the kinetics for build-up and release of the interface charge depends on field and temperature [11].

Besides these geometric space charge effects there are also processes of charge build up due to charge trapping and internal dissociation phenomena. It was shown that the latter effect is strongly influenced by the presence of crosslinking by-products into cross-linked polyethylene. Progress in material behaviour when going from HVAC grade to HVDC was obtained by lowering the amount of crosslinking by-products or even suppressing them completely. But still, the issue remains where electronic carriers can be deeply trapped in the material and contribute to field distortion. There is a general trend towards using high resistivity materials [12] to avoid notable thermal runaway and possible breakdown in the cable [5]. However, this may be accompanied with slower space charge release. So, a kind of trade off has to be found. Fig 3 provides some desired features for insulations with an aim to avoid stress enhancement and heavy charge redistribution, of which both processes lead to damages.

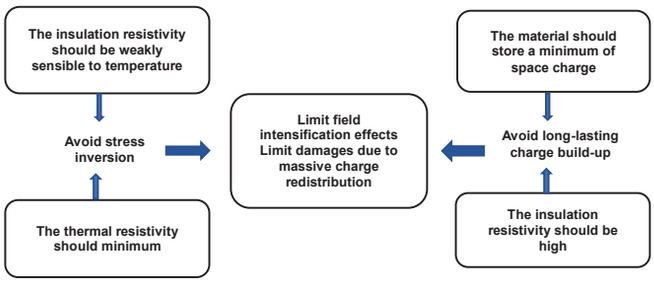

Fig. 3. Strategies for improving material withstanding in HVDC.

Thermal resistivity should be minimized to limit thermal gradients, the insulation's resistivity should be comparatively insensitive to temperature, and having nonlinear properties is attractive for field homogenization purposes (as with paper-oil insulation). These three conditions should limit field intensification. One way to avoid heavy charge distribution is to prevent charge storage, and another is to increase resistivity. However, a higher resistivity can also favour persistent charge storage. Therefore, at the same time as resistivity is reduced, charge generation processes should be avoided. Last, but not least, the DC breakdown stress should be high, even at high temperature, and the material should be insensitive to polarity reversal.

Modelling of insulations under DC electro-thermal stress

Several models have been proposed in the literature through the years to predict space charge and electric field distribution within an insulating material subjected to DC electro-thermal stress. Among these models, two types have been extensively used for the materials of HVDC systems, namely, macroscopic models and fluid models. These models will be described in the following paragraphs and simulation results will be presented for each model and for relevant cases linked to HVDC cables and accessories.

Macroscopic models

The material is considered as weakly conductive for these models and only a gradient in the applied stress (electric field, temperature, etc.) in the material will induce the appearance of a space charge due to non-homogeneity of the conductivity. These models have the advantage of requiring only a few macroscopic parameters, namely, conductivity and permittivity, to simulate the electric field distribution in an insulator. While conductivity is a non-linear function of the electric field and temperature, it is relatively easy to measure experimentally. This has been done for XLPE at different fields and temperatures [10] and an equation for the conductivity variation as a function of these parameters has also been proposed (Eq. 1) [10, 13]. With these data, it is possible to simulate the field and space charge dynamics in a loaded cable with a conductivity gradient. An example of such a calculation is proposed in Fig. 4 for an XLPE-insulated medium voltage (MV) cable 4.5 mm thick, under

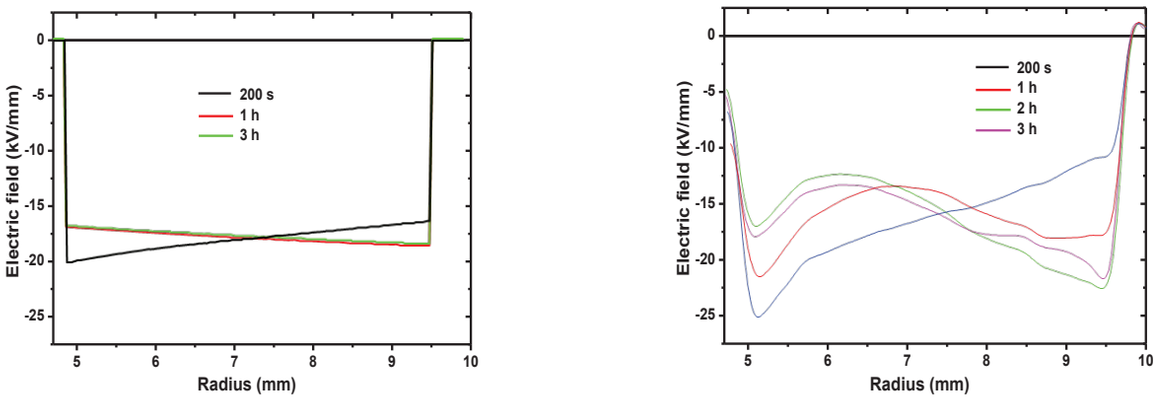

Fig. 4. Field distributions at different times for an MV cable under -80 kV and temperature gradient of ΔT=16°C. (A) Calculated (macroscopic model), **(B)** Measured by pulsed-electro acoustic (PEA) method.

an applied voltage of -80 kV, and a temperature gradient of ΔT=16°C (i.e. T_{in}=57°C and T_{out}=41°C) across the insulation.

The details concerning the conductivity equation, the protocol, and the numerical calculations are detailed elsewhere [10]. The experimental fields calculated from space charge measurements using the pulsed electro acoustic (PEA) method are given in Fig. 4B for comparison (the electric field should start at 0 but this part of the inner conductor is not visible due to the method used). In the simulation, the field distribution quickly deviates from the Laplacian field and achieves a maximum of the electric field at the outer electrode after one hour of polarization. The field distribution stabilizes with time. The maximal electric field values calculated are, respectively, 17 and 18.5 kV/mm at the inner and outer semiconductor. This change from capacitive (i.e. Laplacian field) to a resistive field distribution is due to the conductivity gradient that drives charges from the higher conductivity (inner semiconductor) to the lower conductivity (outer semiconductor). When compared to the experimental data, the same trend is observed, i.e. an inversion of the location of the maximal value of the electric field after one hour. However, in the experiment, the value is twice that which has been predicted by the macroscopic model (~20 kV/mm at the outer semiconductor). Hence, the macroscopic model can only predict the field values under the limits fixed by the conductivity variation linked to the thermal and/or electrical gradient. If other physical phenomena are at play in the cable, these types of models are not sufficient to predict the entire field response.

The real advantage of such a macroscopic model is to use it for large systems, where often times complex geometries and a large number of materials are present, to provide the field distribution along the system. This is, for example, the case with HVDC cable joints where different dielectrics are used and where the geometry plays a key role in the field pattern. Fig 5 shows an example of a pre-moulded joint actually used for a 200 kV DC link, where an interface is formed between two insulating polymers, namely XLPE and ethylene propylene diene monomer (EPDM). This geometry has been implemented in the macroscopic model. Under the simulation conditions, a voltage of 200 kV is applied at the inner side of the XLPE and the outer face of the EPDM is grounded. A current of I=1000 A flows in the conductor core. These conditions imply a temperature gradient as well as a field gradient, in the cable joint.

The calculated electric field distribution in the cable joint is presented in Fig. 6, for the proposed geometry of Fig. 5. In the simulations, we consider here that the thermal and electrical conditions have reached stationary states, with a thermal gradient on the order of 40°C between the cable core and the outside of the joint. The maximal values of the electric field are located, respectively, at the triple point of the XLPE, EPDM, semiconductor, and at the XLPE/EPDM interface at the limit of the cable joint. The field distribution in these regions is controlled by stress cones. The design and modelling of these parts actually represent one of the key points for reliable cable accessories [5, 15-17].

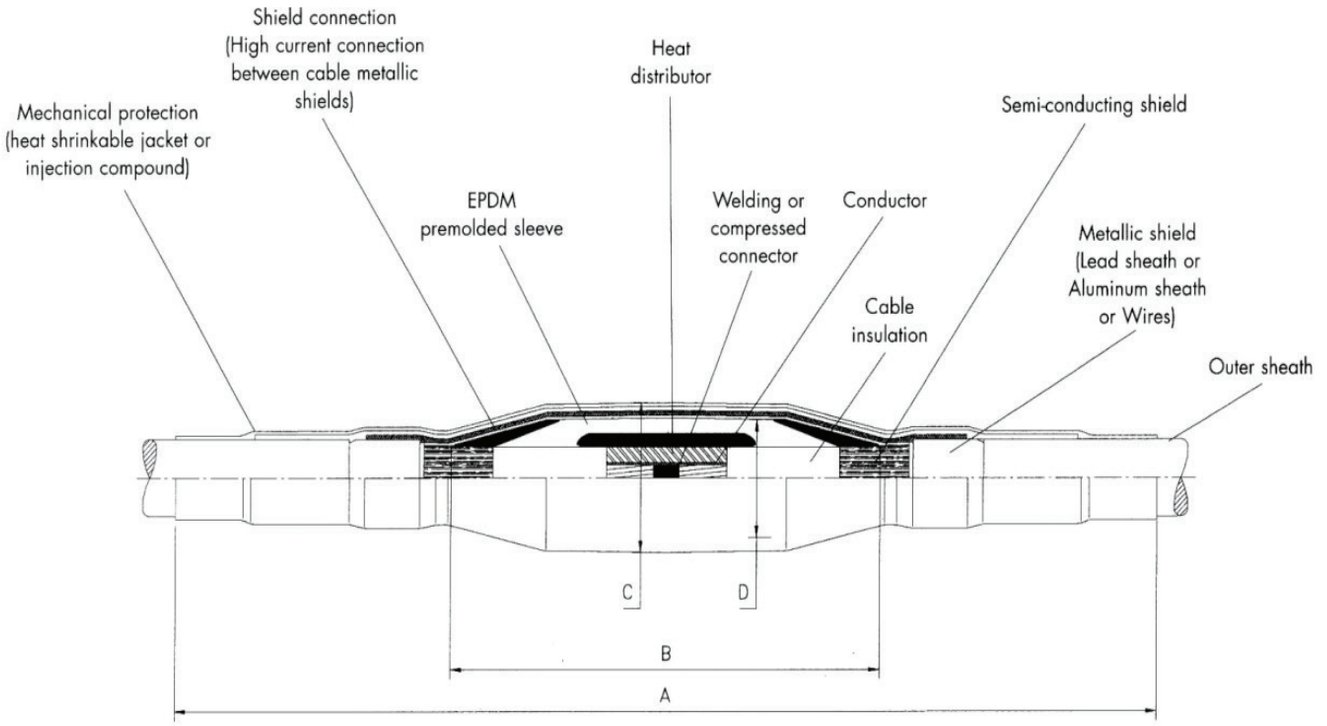

Fig. 5. Schematic representation of a pre-moulded joint for HVDC-extruded cables up to 200 kV [14].

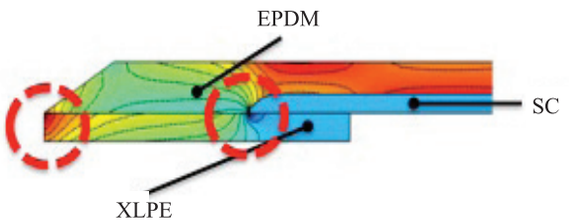

Fig. 6. Electric field distribution in a cable joint under V_{appl}=200 kV and I=1000 A. The colour scale implies a high electric field for red colours, and a lower electric field for blue colours.

This example shows the necessity to optimize the various parameters that play a role in the electric field distribution in cable joints, such as the system geometry (at the triple point but also at the junction boundary) and the material properties. Macroscopic modelling could be used as a design tool to optimize these parameters in regard to temperature and field with the goal of developing new materials with specific properties.

Fluid models

Contrary to macroscopic models, fluid models are based on a microscopic approach, where the physical hypotheses at play should be identified before any model development. They do not rely on the non-homogeneity of the conductivity, but on the generation and transport/accumulation of charges within the material. Instead of considering the conductivity as a macroscopic and homogeneous phenomenon under isotropic conditions, the location where charges are generated is taken into account, as well as their nature and fate during transport. These models can simulate the transient processes that occur when a thermo-electrical stress is applied to an insulating polymer. They account for processes linked to the energy levels located in the band gap, i.e. traps for electrons and holes. They also account for charge generation and extraction at the electrodes. These models are more difficult to implement compared to macroscopic models due to the parameterization of the traps distribution. However, as charge transport is linked to trapping and detrapping, charge accumulation can take place for reasons that are not linked to the non-homogeneity of the conductivity, for example, as a blocking contact at an interface.

Fluid models have been intensively developed these last 20 years [18-20], mostly for low density polyethylene (LDPE), the base resin of XLPE. An example of simulation results using a fluid model for an XLPE cable is proposed

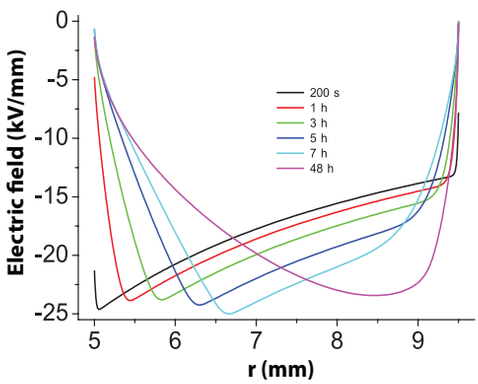

Fig. 7. Simulated electric field distribution (fluid model) vs. radius at different times for an MV cable of 4.5 mm thick insulation polarized at -80 kV, and a temperature gradient of ΔT=16°C.

in Fig. 7, for the same protocol as the one described for the macroscopic model, i.e. an MV cable of 4.5 mm, an applied voltage of -80 kV, and a temperature gradient of 16°C with same internal and external temperatures as mentioned previously. The charges that are accounted for are electronic charges, i.e. electrons and holes. These charges are generated only at the electrodes and follow the Schottky injection law. Charges can be mobile, having a hopping mobility that is a function of the electric field and temperature, or charges can be trapped into a unique level of deep traps, from which they can escape by a thermally activated process. Recombination is also taken into account in the fluid models. Recombination coefficients between each type of charge are a function of the mobility (i.e. Langevin coefficients). A complete description of the physical hypotheses included in the model, the numerical resolution, and the parameterization are detailed elsewhere for cable geometry [21]. When considering the simulated results at a steady state (i.e. 48 h), the electric field distribution is seen to switch from the Laplace field to its maximal value at the outer semiconductor. Moreover, the maximal field value at the outer electrode is on the order of 22.5 kV/mm, which is what has been measured experimentally. From these results, it is noticeable that the fluid model can predict the main characteristics observed experimentally, particularly the field enhancement at the outer electrode compared to the macroscopic model, which is not only due to a conductivity gradient. However, for these models, different processes are at play, with various characteristic times for each process. In this case, the parameterization is very sensitive and has not reached an optimized point and, in the proposed example, the dynamics for field stabilization is longer (48 h) compared to the experimental case (3 h).

Comparing fluid models to macroscopic models by means of electric field distribution shows the strengths and drawbacks of each model:

- Macroscopic models offer an easy implementation of the conductivity and the possibility to simulate complex systems over short time simulations. They are, however, limited when charge accumulation comes into play.

- Fluid models possess an efficient description of the charge behaviour, but at the cost of complex physics and parameterization. Aside from their direct implementation in real geometries in which parameterization and optimization are tricky, fluid models are interesting and efficient for testing hypotheses of physical processes controlling the charging behaviour. Such models are developed based on focused experiments that can be realized at a lab scale, as with electron beam irradiation.

Conclusions

According to current trends, HVDC cables are gradually replacing HVAC because of their significant benefits. However, due to the build-up of space charge and the consequent distortion electric fields, the challenge of designing insulating materials under DC stress is not straightforward. We have explored various research directions for the development of insulating materials and control of stresses upon DC cables by simulations and modelling using different methods. The simulation results of the macroscopic models and fluid models are compared in this work. The macroscopic models have the ability to simulate complex systems over a short time, however, the model is affected by the formation of space charges in the material. Fluid models are effective in modelling the physical processes that control the charging behaviour, but they are difficult in real geometries due to complex parameterization and optimization.

ACKNOWLEDGEMENTS

We would like to acknowledge the C.N.R.S. (France) for financial support to the ModHVDC project n° PICS07965.

The authors declare that there is no conflict of interest regarding the publication of this article.

REFERENCES

[1] T.T.N. Vu, G. Teyssedre, S. Le Roy, et al. (2017), "Space charge criteria for the assessment of insulation materials for HVDC", *IEEE Trans. Dielectr. Electr. Insul.*, **24**, pp.1405-1415.

[2] H.L. Zhang, J.M. Zhang, L. Duan, et al. (2017), "Application status of XLPE insulated submarine cable used in offshore wind farm in China", *J. Eng.*, **13**, pp.702-707.

[3] Z.Y. Huang, J.A. Pilgrim, P.L. Lewin, et al. (2015), "Thermal-electric rating method for mass-impregnated paper-insulated HVDC cable circuits", *IEEE Trans Power Delivery*, **30**, pp.437-444.

[4] S. Qin, S. Boggs (2012), "Design considerations for HVDC components", *IEEE Electr. Insul. Mag.*, **28(6)**, pp.36-44.

[5] C.O. Olsson (2008), "Modelling of thermal behaviour of polymer insulation at high electric DC field", *5th European Thermal-Sciences Conf.*, pp.1-8.

[6] D. Fabiani, G.C. Montanari, C. Laurent, et al. (2008), "HVDC cable design and space charge accumulation. Part 3: Effect of temperature gradient", *IEEE Electr. Insul. Mag.*, **24(2)**, pp.5-14.

[7] N. Adi, T.T.N. Vu, G. Teyssèdre, et al. (2017), "DC model cable under polarity inversion and thermal gradient: build-up of design-related space charge", *Technologies*, **5(46)**, DOI:10.3390/technologies.

[8] G. Mazzanti, M. Marzinotto (2013), *Extruded Cables for HVDC Transmission: Advances in Research and Development*, IEEE Press-Wiley.

[9] S. Delpino, D. Fabiani, G.C. Montanari, et al. (2008), "Polymeric HVDC cable design and space charge accumulation. Part 2: insulation interfaces", *IEEE Electr. Insul. Mag.*, **24 (1)**, pp.14-24.

[10] T.T.N. Vu, G. Teyssedre, B. Vissouvanadin, et al. (2015), "Correlating conductivity and space charge measurements in multi-dielectrics under various electrical and thermal stresses", *IEEE Trans. Dielectr. Electr. Insul.*, **22**, pp.117-127.

[11] T.T.N. Vu, G. Teyssedre, S. Le Roy, et al. (2017), "Maxwell-Wagner effect in multi-layered dielectrics: interfacial charge measurement and modelling", *Technologies*, **5(2)**, DOI:10.3390/technologies 5020027.

[12] V. Englund, J. Andersson, J.O. Boström, et al. (2014), "Characteristics of candidate material systems for next generation extruded HVDC cables", *Proc. Cigre Conference*, Paris, Paper D1-104.

[13] Silec Cable, *One-Piece Premolded Joint for Extruded Cables from 63 to 500 kV.*

[14] M. Jeroense, M. Saltzer, H. Gorbani (2013), "Technical challenges linked to HVDC cable development", *Proc. European Seminar on Materials for HVDC Cables and Accessories (Jicable)*, Perpignan, France, pp.1-6.

[15] D. Quaggia (2015), "Development of joints and terminations for HVDC extruded cables", *Proc. INMR-Insulator News and Market Report,* Munich, Germany, pp.228-234.

[16] S. Hou, M. Fu, C. Li, et al. (2015), "Electric field calculation and analysis of HVDC cable joints with nonlinear materials", *Proc. IEEE 11th Internat. Conf. Properties Appl. Dielectric Materials (ICPADM)*, pp.184-187.

[17]. H. Ye, T. Fechner, X. Lei, et al. (2018), "Review on HVDC cable terminations", *High Volt.*, **3**, pp.79-89.

[18] J.M. Alison, R.M. Hill (1994), "A model for bipolar charge transport, trapping and recombination in degassed cross-linked polyethylene", *J. Phys. D*, **27**, pp.1291-1299.

[19] S. Le Roy, G. Teyssedre, C. Laurent, et al. (2006), "Description of charge transport in polyethylene using a fluid model with a constant mobility: fitting model and experiments", *J. Phys. D*, **39**, pp.1427-1436.

[20] J. Xia, Y. Zhang, F. Zheng, et al. (2011), "Numerical analysis of packet-like charge behavior in low-density polyethylene by a Gunn effect-like model", *J. Appl. Phys.*, **109**, DOI: 10.1063/1.3532052.

[21] S. Le Roy, G. Teyssedre, C. Laurent (2016), "Modelling space charge in a cable geometry", *IEEE Trans. Dielectr. Electr. Insul.*, **23**, pp.2361-2367.

DOI: 10.31276/VJSTE.62(3).45-48

Effect of welding speed on the mechanical properties of friction stir welded aluminium alloy 5083

Tran Hung Tra[1*], Huynh Minh Tu[2]

[1]*Nha Trang University*
[2]*HCMC University of Technology and Education*

Received 6 January 2020; accepted 9 June 2020

Abstract:

The influence of welding speed on the properties of friction stir welded aluminium alloy 5083 was explored. The effects of various welding regimes on the defect formation, hardness distribution, tensile strength, and bending strength of the joint were experimentally investigated. Kissing bond defects were prevalent in the joint, however, this kissing bond was eliminated at high welding rates. The welded zone was softened significantly; all the tensile specimens were fractured in the welding zone with shear mode. The tensile strength of the joint reached 85% of the base aluminium alloy 5083 while the bending ductility of the joint was higher than that of base aluminium alloy 5083.

Keywords: **aluminium alloy 5083, defects, friction stir welding, mechanical properties.**

Classification number: **2.3**

Introduction

Aluminium alloys possess high specific strength and are suitable for high-speed vehicles and among other applications. Aluminium alloy 5083 (abbreviated as AA5083) is an advanced alloy with excellent corrosive resistance; thus, this alloy is used dominantly in shipbuilding. One of the significant challenges in using aluminium alloys is associated with their low weldability. Recently, friction stir welding (FSW) has emerged as a new method for welding aluminium alloys [1-7]. In FSW, the tool heats and moves the metal beneath the tool shoulder to produce the joint [8, 9]. During the FSW process, the microstructure in the welded zone dramatically recrystallizes through the interaction between the tool geometry and welding parameters. Thus, the welded zone becomes inhomogeneous and possesses varied properties [2-3]. Even though this welding technology possesses several preeminent points, application of this technology is still quite limited due to the deficiency of equipment (especially in the case of Vietnam). In this work, which is based on the NTU-FSW equipment at the Friction Research Center, Nha Trang University, the FSW butt-joint of AA5083 plate with 3.0 mm thickness is investigated experimentally and the effect of various welding regimes on the mechanical properties of the joint is evaluated.

Materials and experiments

The AA5083 plates with 3 mm thickness (Korea) were butt joined by the NTU-FSW machine in Friction Stir Welding Lab of Nha Trang University. Two AA5083 plates were joined by a tool with a concave shoulder and a truncated probe. The probe of the tool possessed a 4.0 mm diameter at its middle (with respect to length) and was 2.8 mm in height. The tilt angle of the pin was set at 2.0 deg. Various regimes of welding speed rates (denoted as WSR, mm/rev) were performed to fabricate the joints. The WSR defined as the ratio of weld speed and rotation speed. The microstructure of the welded zone and the base AA5083 was observed by an optical microscope (Olympus, Japan). The hardness property in and around the welded zone was measured by the HM-125 equipment (Japan) using 100 gf loading. Both the tensile specimens and bending specimens

[*]*Corresponding author: Email: tra@ntu.edu.vn*

were tested by the 3366 Instron (Instron, USA) at a constant strain rate of 10^{-3}/s. Here, the tensile specimen geometry was designed based on the standards ASTM E08; the bending specimen geometry relied on ASTM E290. Here the tested specimens were manufactured such that the loading direction was perpendicular to the welding direction, as shown in Fig. 1. Tables 1&2 show a data summary of the chemical composition and mechanical properties of AA5083, respectively.

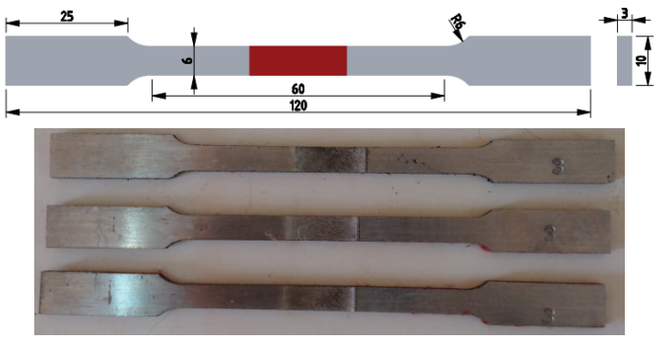

Fig. 1. The geometry of the tensile specimen (ASTM E290), dimension in mm.

Table 1. The chemical composition of AA5083, wt. %

Element	Al	Mg	Mn	Cu	Si	Zn	Mn	Ti	Cr
Percentage (%)	balance	4.0-4.9	0.4-1	Max 0.1	Max 0.4	Max 0.25	Max 0.3	Max 0.15	0.05-0.25

Table 2. The mechanical properties of AA5083 aluminium alloy.

Mechanical properties	Yield strength (MPa)	Tensile strength (MPa)	Elongation (%)	Hardness (HRB)	Elastic modulus (GPa)	Poisson ratio
Value	190	300	16	50	70.3	0.33

Results and discussion

Several welding speed rates were used to fabricate the joints. Afterwards, the defects formations and mechanical properties of the FSW joint were investigated. The typical microstructure of the FSW AA5083 (fabricated at *WSR*=0.71 mm/rev.) is presented in Fig. 2. It can be seen that the welded zone is characterized by dynamic recrystallization (Fig. 2). The grain size in the welded zone was refined significantly. The average grain size diameter in the stirred zone was about 10 μm, whereas the grain size of the base AA5083 was about 40 μm (see Fig. 2(I) and Fig. 2(IV)). The grain of the heat-affected zone (HAZ) was similar to that of the base alloy 5083, see Fig. 2(II&III).

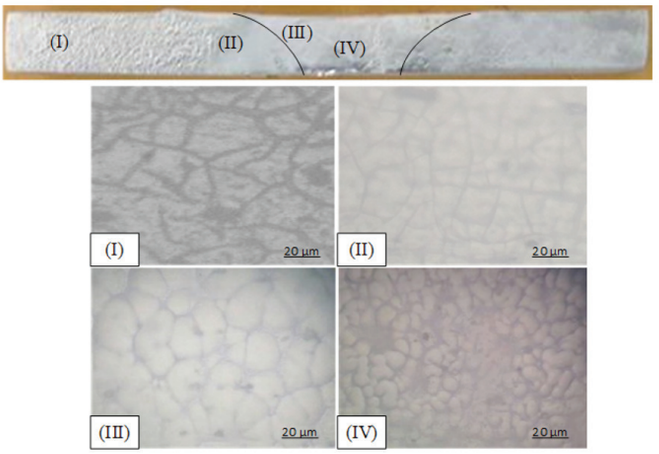

Fig. 2. The cross-section microstructure of the FSW fabricated at WSR = 0.71 mm/rev: base alloy (I), region (II), region (III), and region (IV).

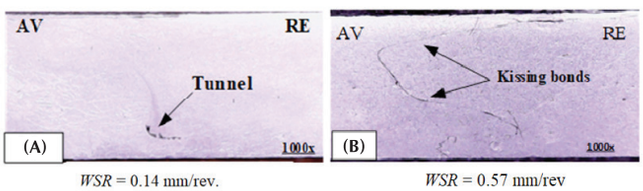

Fig. 3. Tunnel defect and kissing bond defect in the joints (AV and RE are abbreviations of the advancing side and retreating side, respectively).

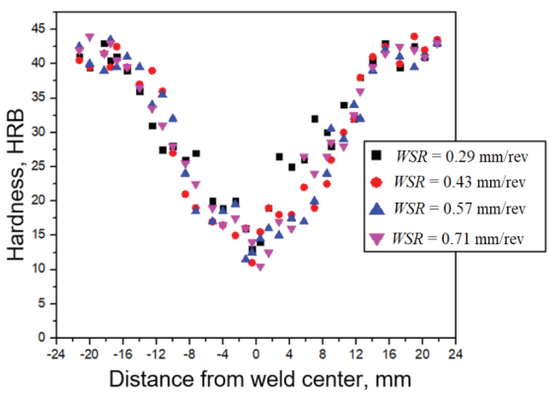

Fig. 4. Hardness distribution across the welding.

In the FSW, both the tunnel defect (see Fig. 3A) and kissing bond defect (see Fig. 3B) were found in the joints. The kissing bond was found to be dominant. The obtained joint was free of defects under the high *WSR* regime (*WSR* = 0.71 mm/rev).

The hardness distributions measured at the middle-line of the cross-sections are shown in Fig. 4 as a function of the *WSR*. For all the welding regimes, the material in the welded region was softened remarkably. This softened zone must be related to degradation of the material induced by the welding temperature. The lowest hardness took place in the

stirred zone where the peak welding temperature is located. The effect of the welding regime on the hardness of the joint seems to be unremarkable. The width of the softened zones (see Fig. 4) also seemed to be independent of *WSR*.

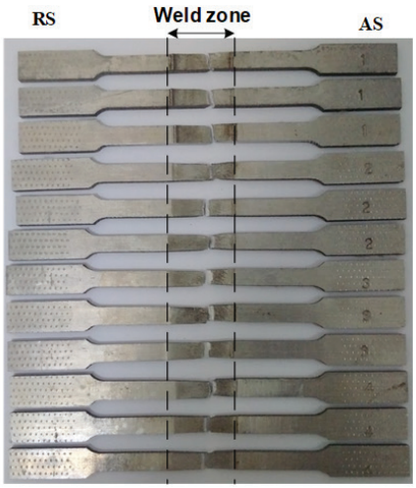

Fig. 5. Tensile specimens and the tensile fracture locations (the dash lines present the tool shoulder).

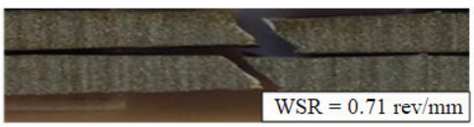

Fig. 6. Shear mode fracture of tensile specimens.

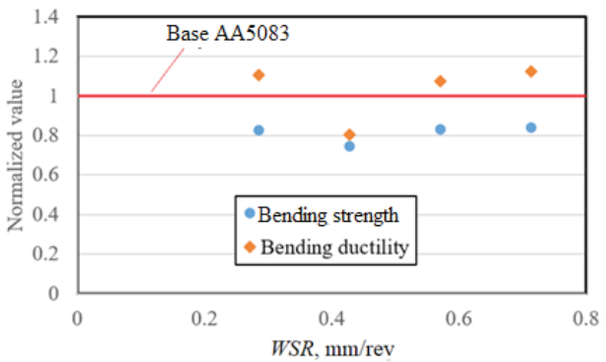

Fig. 7. Bending strength of the joint.

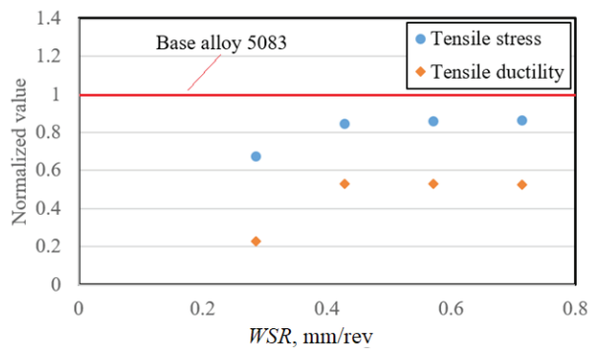

Fig. 8. Tensile strength and elongation of the joint.

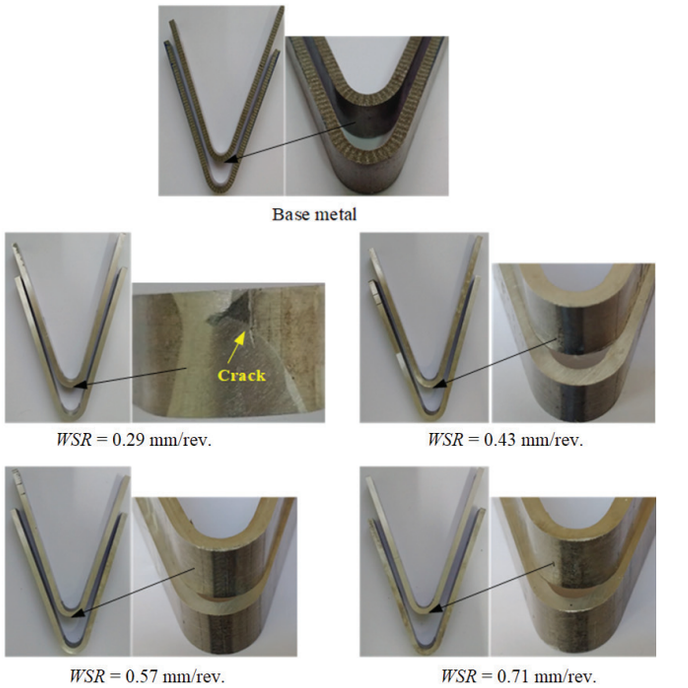

Fig. 9. Bended FSW specimens under various WSR.

To evaluate the tensile properties of the joint, the tensile specimens were extruded from the FSW plate and tested by the 3366 Instron with a constant loading strain rate of 10^{-3}/s. For all cases, the specimens were fractured in the welded zone (see Fig. 5) with a typical shear mode (see Fig. 6). The fracture locations occurred in the lowest hardness zone (Figs. 5 and 4). This fact implies that the effect of welding temperature on the degradation of the welded zone seems to be inevitable.

The ultimate tensile strength and the fracture elongation of the FSW are plotted in Fig. 7. For all welding regimes, in comparison to the base AA5083, the tensile properties of the FSW alloys degraded remarkably. The highest tensile strength and ductility was obtained at a WSR around 0.6 mm/rev. Here, the ultimate strength and fracture elongation of the FSW alloys were about 85% and 57% that of the base AA5083, respectively. It should be noted that at low welding rates, a tunnel defect appeared in the joint (see Fig. 3A). However, high values of *WSR* could lead to an incomplete joint.

The results of bending strength and bending ductility of the FSW alloys under the various welding regimes are shown in Figs. 8&9. In all cases, the bending strength of the

FSW was lower than that of the base AA5083. However, the bending ductility of the FSWs was mostly higher than that of the base alloy. It should be noted that the joint was cracked in the stirred zone (at the bottom face) at a low *WSR* (see Fig. 9). Generally, the bending strength and bending ductility of the FSW alloys are about 86% and 114% that of base AA5083, respectively.

In summary, the kissing bond maintained a prominent factor in the strength of the FSW AA5083. The joint can be obtained with high strength and ductility. Even though the strength of the joint degraded dramatically in comparison to that of the base AA5083, the bending ductility of the joint improved remarkably.

Conclusions

The FSW of AA5083 was successfully fabricated and the effect of welding speed rate on its defects, hardness, tensile, and bending properties was investigated. The kissing bond defect was found to be dominant in the joint but all the defects could be eliminated at high welding rates. The 0.71 mm/rev *WSR* was found to be a suitable regime to obtain a good joint. The strength of the joint reached 85% that of the base AA5083 and the bending ductility improved significantly.

The authors declare that there is no conflict of interest regarding the publication of this article.

REFERENCES

[1] M. Gene (2002), *The welding of aluminium and its alloys*, Woodhead Publishing Ltd, Cambridge England.

[2] Z.Y. Ma (2008) "Friction stir processing technology: a review", *Metallurgical and Materials Transactions*, **37A**, pp.642-658.

[3] R.S. Mishra, M.W. Mahoney editors (2007), *Friction stir welding and processing*, ASM International.

[4] D.D. Hao, M. Okazaki, T.H. Tra, Q.H. Nam (2019), "Defects morphology in the dissimilar friction stir welded T-lap joints of AA7075 and AA5083", *Advances in Engineering Research and Application*, pp.210-216, DOI: 10.1007/978-3-030-04792-4_29.

[5] Tran Hung Tra, Masakazu Okazaki (2017), "Creep-fatigue cracking near the welded interface in friction welding dissimilar superalloys INCONEL 718 and MAR-M247", *Metallurgical and Materials Transactions A*, **48**, pp.3692-3701.

[6] Duong Dinh Hao, Tran Hung Tra (2016), "Effects of friction stir welding parameters on the mechanical properties of AA7075-T6", *Archives of Materials Science and Engineering*, **77(2)**, pp.58-64.

[7] Tran Hung Tra, Masakazu Okazaki, Kenji Suzuki (2012), "Fatigue crack propagation behavior of friction stir welding AA 6063-T5: residual stress and microstructure effect", *International Journal of Fatigue*, **43**, pp.23-29.

[8] M. Shiva chander, P. Satish Kumar, Aruri Devaraju (2018), "Influence of tool rotational speed and pin profile on mechanical and microstructural characterization of friction stir welded 5083 aluminium alloy", *Material Today: Proceedings*, **5(2)**, Part 1, pp.3518-3523.

[9] K. Aruna Prabhaa Prasad, Kumar Puthab Balla, Srinivasa Prasad (2018), "Effect of tool rotational speed on mechanical properties of aluminium alloy 5083 weldments in friction stir welding", *Material Today: Proceedings*, **5(9)**, Part 3, pp.18535-18543.

DOI: 10.31276/VJSTE.62(3).49-55

Variation in morphology of the Red river and Duong river near Hanoi from 2000 to 2018

N.N. Quynh*, B.H. Hieu, N.N. Dang, N.H. Quang, To Vinh Cuong

Key Laboratory of River and Coastal Engineering, VAWR

Received 2 March 2020; accepted 29 June 2020

Abstract:

In recent years, the construction of upstream reservoirs and the extraction and structural construction activities on the river banks and beds have caused downstream changes in river morphology and hydrological regime of the Red river system, which has especially accelerated from 2000 to 2018. These dramatic variations have significantly changed the morphological characteristics and relationship between the flow and morphology that are a fundamental parameter to evaluate the stability of the channels. In this study, the morphological characteristics and relationship between flow and morphology over some periods as well as under current conditions were analysed. This work provides basic river training parameters for studying river training planning of the Red river system in general and for the Red and Duong river sections in Hanoi in particular.

Keywords: **bankfull discharge, relationships, river morphological, river morphology, river training parameters.**

Classification number: **2.3**

Introduction

Since 1987, the Hoa Binh reservoir and also other cascade reservoirs on the Da and Lo rivers have affected the Red river downstream dramatically. Changes to the riverbeds, river morphology, hydrological, and hydraulic characteristics of the Red river system before and after the Hoa Binh reservoir have been shown in several studies. These studies confirm that the impact of the Hoa Binh reservoir on downstream changes is dominant and the impact of these reservoirs on the downstream decreases gradually by time.

However, from 2000 to 2018, the trend has reversed with sudden changes to the channel bed and hydrological regime. The riverbed has been continuously eroded leading to lower water levels, especially in the dry season. Therefore, the operation and safety of hydraulic works (sluices, pumping stations, revetment, etc.) as well as waterway activities, environment, and ecology downstream of the main rivers have been adversely affected [1].

The main causes of these changes to the riverbed and hydrology after 2000 has been analysed in recent studies [2]. In particular, the sediment imbalance across the river system is increasing due to sediment depletion coming from upstream. Besides, the total extracted sediment volume downstream is still increasing. The average annual sediment in the downstream is only about 20-30% of the total extracted sediment, however, the actual sediment volume cannot be extracted from the rivers [3].

Since 2000, changes to the river channel and hydrological regime downstream of the Red river have caused changes in the river's morphological relationships. However, these trends need to be clarified and evaluated along with the channel bed stability under the present conditions. This study will present and analyse new results of the changes in relationship between the flow and morphology for a representative area, which is the Red river and Duong river sections around the center of Hanoi.

The results shown in this paper only consider one of

*Corresponding author: Email: quynhhuy161@gmail.com

basic relationships between flow and morphology. This is the relationship between flow and river cross section that determines the stable width (B) and depth (h) of the cross section.

The calculation and evaluation of the changes in river morphological relationships are the foundation for proposing basic river training parameters to develop river training planning protocols in the Red river system, in general, and for the Red and Duong river sections in Hanoi, in particular. To ensure that it is suitable with actual changes of rivers itself as well as to adapt to the impacts caused by the process of extraction and development on the river.

In order to compare results, the study and evaluation for changes to the river's morphological relationships characteristics are limited to the period from 2000 to 2018, which are divided into 3 periods: from 2000 to 2005; from 2006 to 2010 and from 2011 to 2018 (Fig. 1).

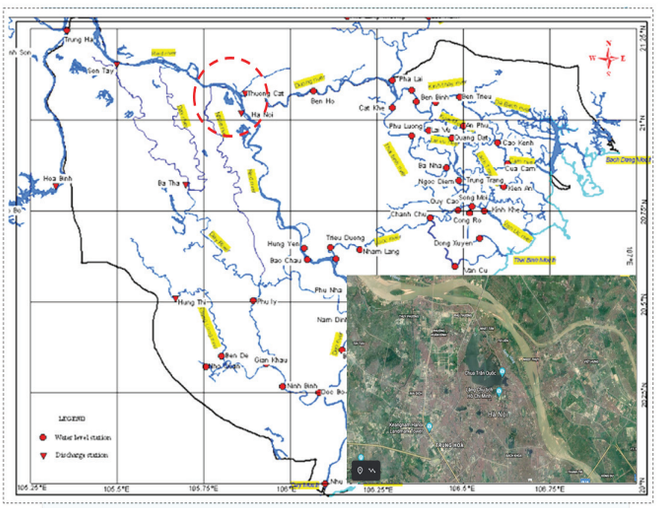

Fig. 1. Red river - Thai Binh river system and the Red and Duong river sections near Hanoi (source: Directorate of Water Resources, MARD).

Objects, materials and methods

Objects

The relationship between cross section and corresponding water level and bankfull discharge or bed building discharge is the studied river morphological relationship.

The basic parameters of the river morphological relation are stable width (B) and depth (h) of a section.

Materials

Hydrological and hydraulic data: daily water level, discharge, turbidity at Hanoi hydrological stations (Red river) and Thuong Cat (Duong river) from 2000 to 2018.

Topographic data: annual river cross-sections above hydrological stations; river cross sections are measured discontinuously from 2000 to 2018 and topographic maps are measured in 1999, 2005, 2008, 2010, 2014, 2016, 2018 on the Red river section from Lien Mac to Thanh Tri and the Duong river from Duong gate to Duong bridge. These topographic data were collected from state-level science and technology projects under KC.08/10-15, KC.08/15-20 programs; waterway consultancy projects of the Ministry of Transport (MT); survey projects of the Red river channel by the General Department of Disaster Prevention, Ministry of Agriculture and Rural Development (MARD).

Survey data, geological surveys of river channel, sediment on the bed of the Red river section and the Duong estuary in 1999, 2009, 2013, and 2016 are provided by fundamental projects and research projects granted by the Vietnam Academy for Water Resources.

Hydraulic parameters (water level, discharge, hydraulic slope, etc.) of the Red river system in years 2000, 2005, 2010, 2013, 2014, 2016, 2017, and 2018 were calculated by using the MIKE11HD and MIKE21HD models provided by research projects at ministerial and Hanoi levels and at the State level of the Vietnam Academy for Water Resources Research.

Methods

River morphological relationships at cross sections:

In order to analyse and calculate parameters of the main river cross section, two relationships (methods) are commonly used in Vietnam as follows:

- The morphological method is based on the method of C.T. Altunin, which describes the relationship between the stable width and depth under the influence of bankfull discharge and the method of the Russian Hydrology Institute, which focuses on the relationship between the width and depth at a stable cross section. This relationship shows the stability of the river channel at the cross section for each period:

$$B = A\frac{Q_f^{0.5}}{J^{0.2}} \quad (1)$$

$$\frac{\sqrt{B}}{h} = \zeta = \text{const} \quad (2)$$

where: B and h are the average width and depth of the stable river bed, respectively; A is the lateral stability coefficient (also known as bank stability coefficient); Q_f is the bankfull discharge (discharge corresponding to a water level at bank elevation); J is the water surface slope corresponding to bankfull discharge.

- The method of Prof. Luong Phuong Hau [4] shows the relations of a stable width and depth of the riverbed over average water level periods (or main river channel) under the impact of bankfull discharge:

$$B = 2.60\frac{W^{0.24}S^{0.24}}{g^{0.4}d_{90}^{0.32}}Q_f^{0.57} \quad (3)$$

$$h = 1.52\frac{g^{0.05}d_{90}^{0.24}}{W^{0.43}S^{0.43}}Q_f^{0.32} \quad (4)$$

where: d_{90} is the calculated sediment diameter (mm); W is the calculated flow velocity (m/s); S is the average sediment load (kg/m^3); Q_f is the bankfull discharge (m^3/s).

In this study, we only calculate the parameters B and h according to the method of C.T. Altunin. The calculation according to Prof. Luong Phuong Hau's method requires one to determine the actual value of the parameters d_{90}, W, and S, which is not within the scope of this work because the above parameters fluctuate greatly due to impact of the upstream reservoir system as well as riverbed extraction in the downstream. Thus, it leads to sediment imbalance, deep bed erosion, lack of incoming discharge and a complicated hydraulic regime, especially at the confluence of the Red and Duong river.

Determining bankfull discharge method:

For both of the mentioned river morphological relations, the most important thing is to determine the bankfull discharge. Bankfull discharge is a quantity that indicates the combined impact of a river discharge on the bed building process over a long time.

According to the morphological relationship of stable river channel, when the bankfull discharge changes, the morphological factor of the river channel will be recreated to adapt to new conditions, in which the most important are the factors of river cross-section including stable width and depth.

There are several methods to determine bankfull discharge in Vietnam and we often use the V.M. Macckaveep method. This is a method mainly based on series of statistical hydrological data (discharge, Q, and sediment concentration, ρ) at main hydrological stations on rivers.

Currently, under the real conditions of the Red river system, the application of the V.M. Macckaveep method is unsuitable because the deep bed erosion keeps increasing, which causes severe changes in morphological and hydrological characteristics at the stations. Further, sediment concentration in the downstream has been continuously decreasing over recent years and is currently very low such that it does not correctly show the actual process of sediment transport and rebuilding in the river channel.

Therefore, the bankfull discharge, Q_f of the Red and Duong river sections surrounding Hanoi is calculated by the following methods: building the relationship between discharge and water level (Q-H relation) from the measured data at Hanoi and Thuong Cat stations over the research periods, determining the Q-H relation for each year and over each period, then analysing and determining discharges corresponding to the water level at the riverbank at the above two stations. It should be noted that the riverbank elevation is the elevation of the natural riverbank, which has not changed or been affected by development and extraction activities of the floodplain.

Results and discussion

Results

Changes in river channel and hydrological regime of the Red and Duong river sections surrounding Hanoi from 2000 to 2018:

Analysed results of the changes to the Red and Duong River channel surrounding Hanoi in the period from 2000 until 2016 [1] confirm that the river channel tends to be continuously eroded. The results presented in Table 1 below have been updated until 2018 and the rivers are divided into sections appropriate for this study, in which the trend of deep erosion in the river channel has no sign of decline.

Table 1. Changes in river channel of Red river and Duong river sections surrounding Hanoi center from 2000 to 2018.

No	River/river section	Erosion level of river bed from 2000 to 2018 (m)	Note
1	***Red river***		
	From the confluence of Thao and Da rivers to the Luoc inlet	0.81÷4.22	Common deep erosion values (excluding local erosion points)
	River sections surrounding Hanoi: from Liem Mac to Thanh Tri	1.86÷3.25	
	At Hanoi hydrological station	3.08	
2	***Duong river***		
	Whole Duong river	3.30÷6.67	Common deep erosion values (excluding local erosion points)
	Upstream Duong river from Xuan Canh to Duong bridge	4.60÷6.67	
	At Thuong Cat hydrological station	5.32	

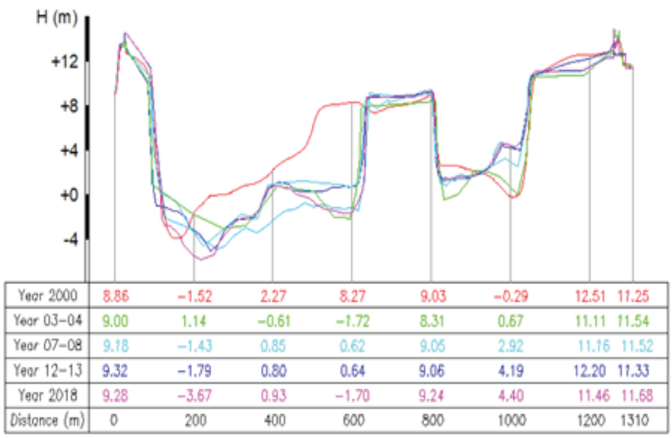

River cross section at Hanoi station

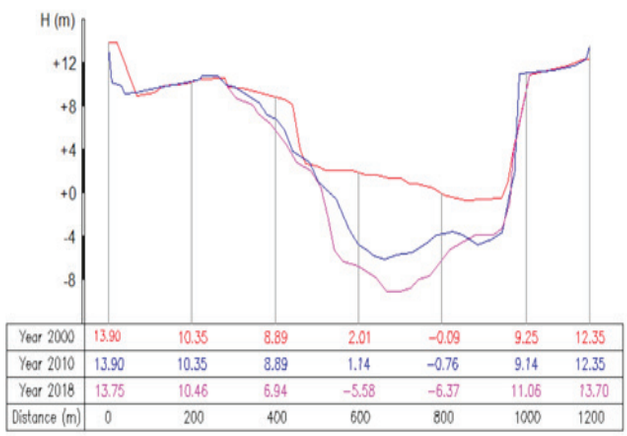

River cross section at Thuong Cat station

Fig. 2. Changes of river cross sections from 2000 to 2018 at Hanoi and Thuong Cat stations.

The deep erosion trend caused lower water levels, especially the water level during the dry season as well as hydrological and flow characteristics in most of the rivers (Fig. 2).

Changes to the hydrological regime on the Red and Duong rivers near Hanoi are considered through the increasing and decreasing trend of hydrological characteristics (discharge, water level) over the whole year, each season, and relation of discharge and water level (Q-H) over the period from 2000 to 2018. Based on the observed data, we made the following comments:

In the Red river section near Hanoi, the average annual discharge and discharges in the flood and dry season are reduced. Meanwhile, water level is significantly lower during the flood season, however, the annual water level reduces negligibly but the water level in the dry season increases.

In the section of the Duong river near Hanoi, the annual discharge and discharges in the flood and dry season tends to decrease more than that in the Red river sections. On the contrary, the average water level is unchanged during the flood season but increases significantly over the whole year and dry season.

The relations of Q-H at Hanoi hydrological stations (on the Red river) and Thuong Cat station (on the Duong river) show that the variation level over each period is very large and the common trend is that at the same discharge value the water level is continuously lowered (Figs. 3-5).

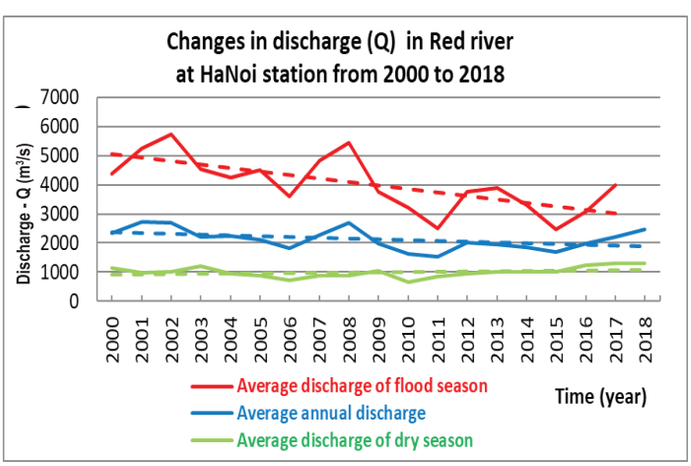

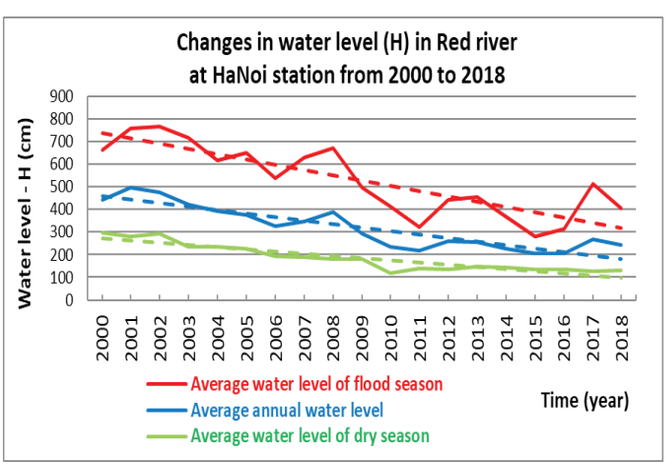

Fig. 3. Changes in hydrological characteristics in Red river at Hanoi station from 2000 to 2018.

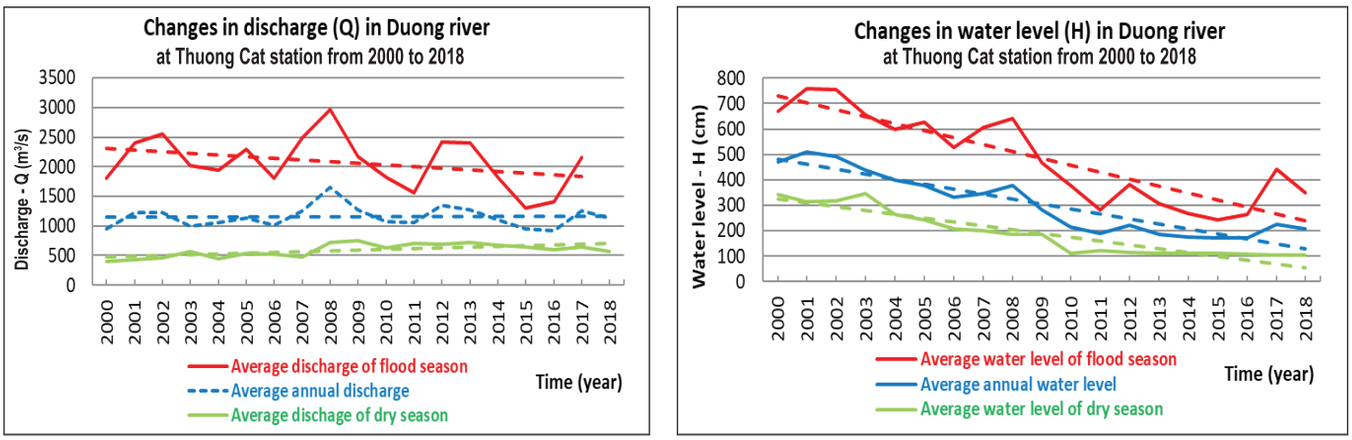

Fig. 4. Changes in hydrological characteristics in Duong river at Thuong Cat station from 2000 to 2018.

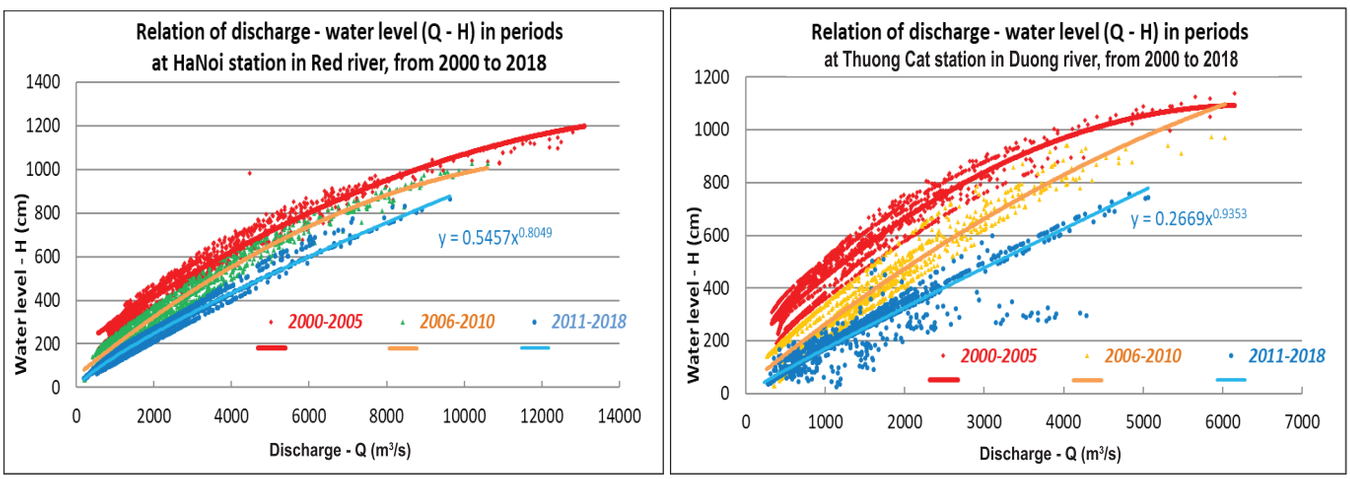

Fig. 5. Relation of discharge - water level (Q-H) in periods in Red river at Hanoi station, and in Duong river at Thuong Cat station from 2000 to 2018.

Determine bankfull discharge:

An analysis of the bankfull discharge (Q_f) in the Red river and Duong river sections near Hanoi over each period from 2000 to 2018 implemented based on the relation of Q-H and the floodplain elevation at Hanoi and Thuong Cat stations are shown in Table 2.

Table 2. Calculated bankfull discharge of Red river and Duong river at the cross sections of two stations.

Bankfull discharge	Period		
	2000-2005	*2006-2010*	*2011-2018*
Hanoi station (Red river)/floodplain elevation = 9.3/9.8m			
Q_f (m^3/s)	8,280	9,100	10,240
Thuong Cat station (Duong river)/floodplain elevation = 9.0/9.2m			
Q_f (m^3/s)	3,370	4,150	5,000

It is noted that the previously calculated bankfull discharge of the Red and Duong river sections near Hanoi based on the V.M. Macckaveep method is always less than results shown in Table 2.

The bankfull discharge in Table 2 is significantly greater than the calculated values based on other relations of river morphology in the past [4-6].

We believe that the changes to the incoming discharge and sediment transport from upstream tend to decline in recent years and our results of the bankfull discharge based on the relation of the measured discharge and water level Q-H is more appropriate.

Calculating average width (B) and depth (h) at river cross section according to C.T. Altunin method:

The stability coefficient of riverbank A according to the C.T. Altunin method that describes changes in riverbanks, river beds, and sediment transport in the river, is in the range of 0.9-1.7 for the Red and Duong river. Besides, based on previous studies from Professor Vu Tat Uyen and other researchers [5-7], the A coefficient varies from 0.9-1.1 and has slight changes during the periods. The bankfull discharge (Q_f) is illustrated in Table 3.

Table 3. Morphological and hydrological parameters of the Red and Duong rivers near Hanoi.

Morphological and hydrological parameters	Period		
	2000-2005	*2006-2010*	*2011-2018*
Red river from Lien Mac to the inlet of the Duong river			
Q_f (m^3/s)	11,930	13,160	14,800
J (10^{-4})	0.72	0.80	0.85
B (m)	818	810	792
h (m)	9.05	9.32	9.90
A	1.0	1.0	0.9
Red river from the inlet of the Duong river to Xuan Quan			
Q_f (m^3/s)	8,280	9,100	10,240
J (10^{-4})	0.70	0.75	0.81
B (m)	703	683	668
h (m)	8.27	8.61	9.42
A	1.0	0.95	0.9
Duong river from the inlet to Duong bridge			
Q_f (m^3/s)	3,370	4,150	5,000
J (10^{-4})	1.15	1.30	1.60
B (m)	366	357	360
h (m)	8.80	9.84	10.63
A	1.1	1.05	1.0

Note: the meaning of the parameters Q_f, J, B, h is the same as that in Eqs. (1) and (2).

Based on the 2019 results of the report "Calculate hydraulic characteristics by using MIKE11HD model for Red and Thai Binh river systems" [8] under project number KC.08.10/16-20, the average water surface slope (J) of the Red and Duong river sections near Hanoi varies with time and tends to increase from 2000 to present. In general, the water surface slope in the Duong river is much larger than that of the Red river.

The average depth (h) is calculated based on average width (B) and representative cross-sectional area in the studied river section. The representative cross section in the Red river section downwards to the inlet of the Duong river is at the Hanoi hydrological station. For the Duong river, it is observed at the Thuong Cat hydrological station and for the Red river upwards it is observed in front of the Duong inlet at the Lien Mac sluice.

Determining changes of river morphological relationship in cross section ($\sqrt{B}/h$):

Table 4. Changes of river morphological relationship in cross section during periods.

Morphological and hydrological parameters	Periods		
	2000-2005	*2006-2010*	*2011-2018*
Red river from Lien Mac to the inlet of Duong river			
B (m)	818	810	792
h (m)	9.05	9.32	9.90
$\zeta = \sqrt{B}/h$	3.16	3.05	2.84
Red river from the inlet of the Duong river to Xuan Quan			
B (m)	703	683	668
h (m)	8.27	8.61	9.42
$\zeta = \sqrt{B}/h$	3.21	3.04	2.74
Duong river from the inlet to Duong bridge			
B (m)	366	357	360
h (m)	8.80	9.84	10.63
$\zeta = \sqrt{B}/h$	2.17	1.92	1.78

The results in Table 4 showed that the riverbed stability in the Red and Duong rivers in the study area tends to decrease.

Discussion

In recent years, the bankfull discharge is widely determined by using the V.M. Macckaveep method in most of the river training studies in Vietnam. It is a method mainly based on a dataset of hydrological characteristics (discharge, Q, and sediment concentration, ρ) at observed stations. Under the condition that the river system is greatly affected by human activities, including exploitation and use for socio-economic development goals, the discharge and sediment density values do not reflect their natural characteristics. Thus, the bankfull discharge value is no longer suitable in reality.

For this reason, the water level corresponding to the bankfull discharge calculated by the V.M. Macckaveep method is often much lower than the riverbank elevation. The main reason for this is the Red and Duong riverbeds have tended to be continuously eroded from 2000 to present.

In this study, the bankfull discharge is calculated by using the traditional Q-H relation method. This is more

appropriate under current conditions of the studied river sections, however, it also requires further analysis and assessment in bankfull discharge for other rivers and river sections in the Red river system to show more convincing evidence for practical and theorical aspects.

Conclusions

Changes to the hydrological and morphological characteristics of the Red river from 2000 up to now show that the Red river has been in a new development process with different hydrological and morphological characteristics. Planning should be reviewed and studied, as well as parameters designed related to the current management as well as construction of hydraulic works and infrastructure in the Red river system.

Basic parameters such as B and h are also parameters for river training during the average water level season (main riverbed). When these factors change, there is a need to recalculate and redesign river training plans for the river channel during the average water level season and also for general river training plans during the flood and dry seasons to ensure environmental and ecological protection.

The river morphological relationship of cross sections ($\sqrt{B}$/h) tends to decrease, which shows the stability level on the cross section of the river bed of the Red and Duong rivers has also decreased.

This is an important issue to inform agencies at the Central and Hanoi levels. These issues are not only for river management, but also related to planning the river extraction and use of riverbeds and riverbanks for infrastructure and socio-economic development.

ACKNOWLEDGEMENTS

The research results presented in this paper are a part of the Science and Technology Program at National level: KC.08.10/16-20. We - the Key Laboratory of River and Coastal Engineering would like to thank the Ministry of Science & Technology, its managing agencies and the Executive Board of the National Science and Technology Program Office (KC.08/16-20) has financed, supported us to implement the research.

The authors declare that there is no conflict of interest regarding the publication of this article.

REFERENCES

[1] Nguyen Ngoc Quynh (2018), *Report on Assessing Current Condition and Forecasting Trends of River Bed, Water Level in the Red River System in Dry Season and Solutions to Overcome and Minimize Adverse Impacts*, Report to MARD leaders.

[2] Nguyen Ngoc Quynh (2017), "Assessing variations and causes of sediment decline in the Red river system during 2000-2015", *Journal of Water Resources Science and Technology*, **41**, pp.2-8.

[3] Pham Dinh, et al. (2015), *Studying Effects of Sand Extraction on Flow Regime, Channel Evolutions and Proposing Scientific and Technological Solutions for Management and Regulation, Reasonable Sand Extraction Plan on the Red and Thai Binh River System*, National Science and Technology project, code: DTDL.2012-T/27.

[4] Luong Phuong Hau, et al. (2010), *Study on Scientific and Technological Solutions for River Training System on Key River Sections in the Northern Delta*, National Science and Technology project, code: KC.08.14/06-10.

[5] Nguyen Ngoc Quynh (2013), "Impact of channel evolution on river characteristics and hydrological relationships on the Duong river", *Journal of Water Resources Science and Technology*, **16**, pp.45-52.

[6] Nguyen Ngoc Quynh (2016), "Impact of lowering river bed on hydrological regime and morphology of the Red river channel", *Journal of Water Resources Science and Technology*, **35**, pp.41-48.

[7] Vu Tat Uyen (1982), *Variations of the Red River Section from Viet Tri to Hanoi*, Proceeding of scientific reports on river dynamics.

[8] Nguyen Manh Linh (2019), *MIKE11HD Hydraulic Model Calculation Report*, National Science and Technology project, code: KC.08.10/16-20.

DOI: 10.31276/VJSTE.62(3).56-61

Water balance for agriculture production in the dry seasons of the Mekong river delta in Vietnam

Le Anh Tuan*

Research Institute for Climate Change - Can Tho University

Received 8 April 2020; accepted 24 July 2020

Abstract:

Water is the most important component of agriculture production, especially during the dry seasons when all water sources are scarce yet water needs are very high. The Mekong river delta in Vietnam is the largest agricultural and aquacultural region in the country where about half of the Delta's land area is used for rice and upland crop cultivation. One key strategy to address the regional water utility problem is to estimate the net water requirement during the dry seasons. The needs for irrigation water discharge for rice and other upland crops during the dry seasons of the Delta were quantified using the Penman-Monteith equation for estimating reference crop evapotranspiration along with the CROPWAT model for calculating crop irrigation water requirements. In general, the total water taken from the Mekong river flow for irrigation requirements should be approximately 2,300-2,600 m^3/s for normal yields in the current agriculture areas and under local cultivation conditions. Water diversion and upstream hydropower projects are challenging tasks, especially in the context of climate change, to satisfy the water needs for agricultural irrigation in the near future. All water stakeholders among the neighbouring countries that rely on the Mekong river must adjust their regional water-use planning as one of the mitigation solutions for the seasonal drought crisis.

Keywords: **agriculture, CROPWAT model, irrigation water, Mekong Delta, water balance.**

Classification number: **3.1**

Background

The Vietnamese Mekong river delta (MD) is the largest wetland region in the southernmost part of the Mekong river basin and connects more than 700 km of coastal line to the East Sea and the Gulf of Thailand (Fig. 1). The Delta is four million ha in size (12% of total natural land of Vietnam) and hosts more than 18 million inhabitants (about 22% of the entire country's population in 2009). For more than 300 years, the local people have lived close to rivers and streams to facilitate the domestic use of water, such as for agricultural cultivation, fishery, and river transportation. Thus, any change in the water source affects their activities and the ecosystem of the area. The MD is recognized as the largest agriculture and aquaculture production region of Vietnam. The delta supplies more than 53% of the nation's staple food, rice (Fig. 2), 65% of the total fish production, and 75% of the tropical fruit trees. Further, rice production is considered to be the main economic sector, which occupies more than 60% of the labour force in the MD.

The total rice production of Vietnam for the 2014-2015 market year reached 45.18 million tons of paddy rice or approximately 28.24 million tons of milled rice. Since the end of the 1980s, Vietnam has been known as one of the top five milled rice exporters to the world market and more than 90% of Vietnam's rice export comes from the MD. From a series of data obtained from the General Statistical Office [1], the total rice production in the MD exceeded 25.25 million tons in 2014-2015. In this period, about 7.1 million tons of rice was sold to the world food market, which became the record for the largest amount of rice exported from the nation. The cropping calendar for rice and other upland plant cultivation in the MD, in terms of the

*Email: latuan@ctu.edu.vn

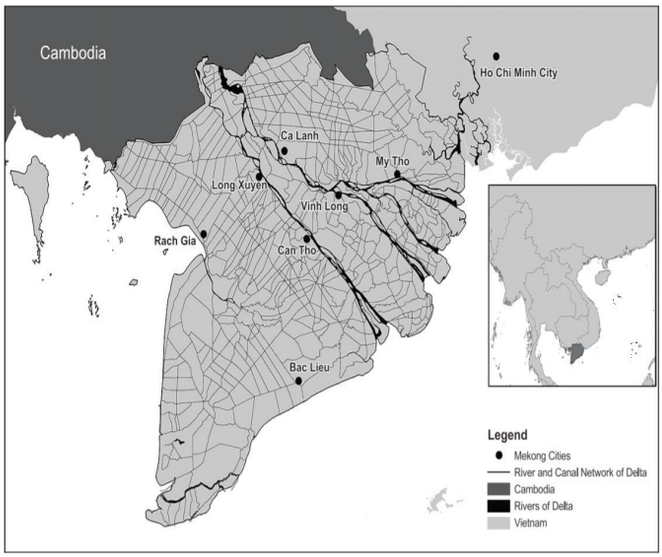

Fig. 1. The Mekong river delta in Vietnam and the delta's network of rivers and canals. Source [2].

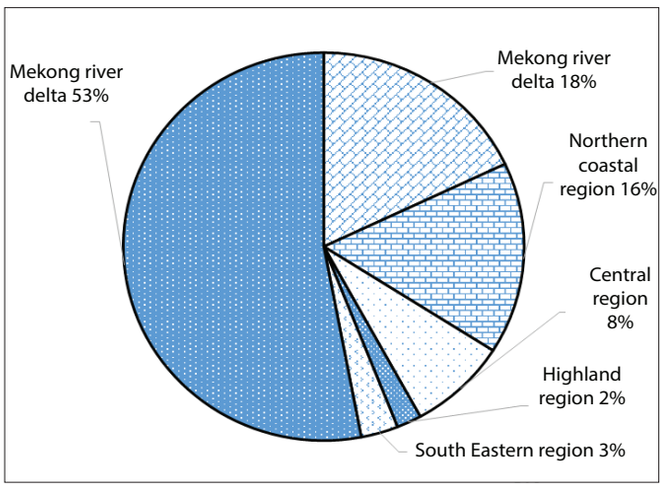

Fig. 2. Contributions to rice production in Vietnam. Data source [3].

growing season duration and the number of crops against the available water conditions in rainfed and irrigated areas, is shown in Fig. 3. From the calendar, a very large water requirement occurs at the end of the dry season, i.e. March and April. However, in March and April, a majority of the seasonal rice has been harvested and those fields are vacated. In a few irrigated areas and saltwater intrusion-free areas such as the An Giang, Dong Thap, Can Tho, and Vinh Long provinces, farmers may plough the lands to prepare for their new rice crop and a lot of water is pumped to the rice fields in March and April.

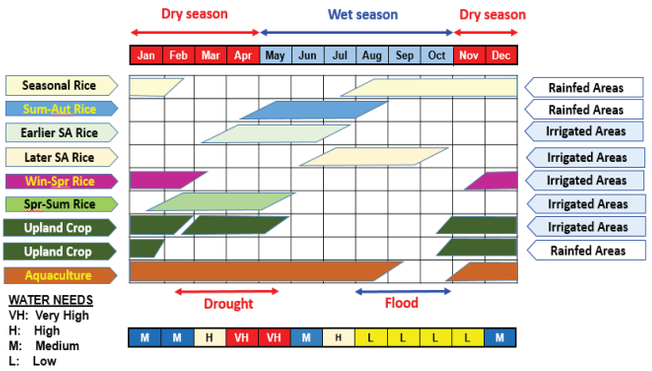

Fig. 3. Agricultural cropping calendar in the Vietnamese MD.

Since 2014, locating fresh water sources has become a huge challenge for agricultural irrigation, especially during the dry season. The available water flow from the Mekong river to the delta has seriously dropped resulting in saline water intrusion of hundreds of thousands of hectares of rice fields. According to the statistics from the Ministry of Agriculture and Rural Development [4], the serious effects of drought and saline intrusion in 2015-2016 caused damage to more than 339,000 ha of Winter-Spring rice paddies, which resulted in a nearly 22% loss of total rice area across the region. Due to limits placed on irrigation water, the Winter-Spring rice crop area dropped by 8.72% in 2016 when compared with the rice area in 2014 (Fig. 4).

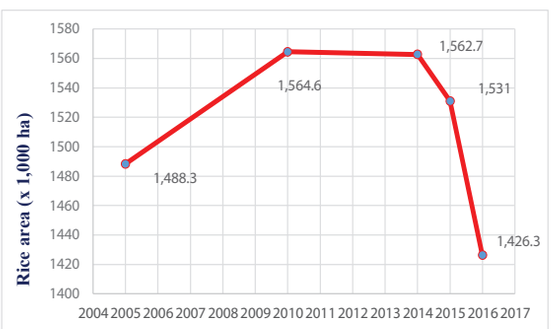

Fig. 4. Change in the Winter-Spring rice areas in the MD due to drought and saline intrusion. Data source [1].

Rice is a major food source for not only the Vietnamese but also for many people around the world. It is well-known that rice cultivation in the lowlands like the MD requires copious amounts of water. At the flowering stage of rice growth, the need for water is high and the rice yield is very sensitive to water deficit, which results in increased spikelet sterility and thus fewer grains. Determining the amount of field water needed to produce one kilogram of rice is a critical issue for water managers. Many experiences have shown that there are large variations in the water need, i.e.,

to produce one kilogram of rice, about 3,000-5,000 litres of water is required on average, which greatly depends on farming management and weather.

In agro-meteorology, evapotranspiration is a word combining evaporation and transpiration and is one of the most significant components of water balance in crop fields. On average, it takes 1.432 litres of evapotranspired water to produce 1 kg of rough rice [5]. In reality, the water need may go up to 2,500 litres, which includes the outflows of evapotranspiration, seepage, and percolation [6]. Water demand for agricultural cultivation is defined as the amount of water required for crops that compensates for the loss of water due to evapotranspiration and the physical conditions of the soil and land that contribute to water storage as well as the growth stages of the crop. Table 1 presents a rough comparison of water balance for irrigated areas in the countries of the Lower Mekong basin (LMB) versus land area, population, and the Mekong river flow discharge available in the dry season. An estimation of irrigation volume requirements for rice and other upland crops is considered as a regional water security strategy.

Table 1. Land, population and rice production in the Lower Mekong basin, 2014.

Variable	Thailand	Laos	Cambodia	Vietnam	Total
Area in LMB (km^2 x 10^3)	184.0	202.0	161.0	95.0	642.0
Area in LMB (%)	28.7	31.5	25.0	14.8	100.0
Population in LMB (2014) (x 10^6)	24.2	6.1	12.5	23.0	65.8
Population in LMB (2014) (%)	36.7	9.3	19.0	35.0	100.0
Population density (persons/km^2)	132	28	78	279	103
Agriculture area in LMB (ha x 10^3)	10,300	1,900	3,100	4,610	19,910
Paddy area in LMB (ha x 10^3)	1,647	631	1,647	2,606	6,531
Paddy are as % of agric. area	45.1	33.2	53.1	56.5	47.9
Irrigated paddy area (ha x 10^3)	1,425	172	505	1,921	4,023
Irrigated as % of paddy area	30.7	27.3	30.7	73.7	42.2
Paddy prod. (2014) (t x 10^6)	14.7	3.9	8.7	25.2	52.5
% growth of prod. (2000-2014)	2.5	4.5	6.1	3.0	3.4
Average yield (2014) (t x 10^6)	2.6	4.3	3.1	5.9	3.8
Prod. as % of country's total	45	98	94	56	57

Data source [7].

Methodology

CROPWAT [8] is a decision support system software developed by the Land and Water Development Division of the UN's Food and Agriculture Organization for the calculation of crop water and irrigation requirements based on soil, climate, and crop data. The equations for the efficient quantity of crop water are based the guidelines of [9] and the expected crop yield is based on the water use in [10]. The maximum crop evapotranspiration (ET_{crop}) is equal to the reference-crop evapotranspiration (ET_o) multiplied by the crop coefficient (K_c):

$$ET_{crop} = K_c \text{ x } ET_o \quad \text{(Eq. 1)}$$

The crop coefficient values, K_c, were provided for a large number of crops and the procedures to determine the ET_{crop} over the growing season were followed. Crop water requirements are defined by the depth of water needed to mitigate water loss through maximum crop evapotranspiration (ET_{crop}) in order to achieve full production potentials under the given crop growing environment. The Penman-Monteith equation is the FAO's standard method for modelling evapotranspiration and is formulated as [8]:

$$ET_o = \frac{0.408\,\Delta(R_n - G) + \gamma \frac{900}{T+273} u_2 (e_s - e_a)}{\Delta + \gamma(1 + 0.34 u_2)} \quad \text{(Eq. 2)}$$

where ET_o ($mm.day^{-1}$) is the reference evapotranspiration, R_n ($MJ.m^{-2}day^{-1}$) is the net radiation recorded at the crop surface, G ($MJ.m^{-2}day^{-1}$) is the monitored soil heat flux density, T (°C) is mean daily air temperature measured at 2 m height, u_2 ($m.s^{-1}$) is the wind speed measured at 2 m height, e_s and e_a (kPa) are the actual vapor pressure and saturation vapor pressure such that (e_s - e_a) (kPa) is the saturation vapor pressure deficit, Δ (kPa $°C^{-1}$) is the slope of the vapor pressure curve, and γ (kPa $°C^{-1}$) is the psychometric constant.

The water balance equation for a rice field is estimated by Eq. 3:

$$h_{Ci} = h_{0i} + \sum m_i + \sum P_{sdi} - \sum (e_i + K_i) - \sum C_i \quad \text{(Eq. 3)}$$

where all units are mm, h_{ci} is the water depth of the field at the end of calculated period, h_{oi} is the water depth in the field in the start of calculated period, Σm_i is the irrigated water during the i^{th} calculated period, ΣP_{sdi} is the possible precipitation used during the i^{th} calculated period, $\Sigma(e_i + K_i)$ are the water losses during the i^{th} calculated period, and ΣC_i is the drainage water during the i^{th} calculated period. It is necessary to first have an irrigation scheme based on Eq. 3 and then the irrigation water volume to each unit of irrigation land (m^3/ha) is estimated.

For estimation of the water requirement for an irrigation scheme, the coefficient of irrigation (q), defined as the water discharge needed for providing a plant cultivation area unit, is given in Eq. 4:

$$q_{ij} = \alpha_i \frac{m_{ij}}{86.4 \times t_{ij}} \quad \text{(Eq. 4)}$$

where q_{ij} ($l.s^{-1}ha^{-1}$) is the coefficient of irrigation of the i^{th} plant in the j^{th} irrigation time, α_i is the ratio of the area between the i^{th} plant and the entire irrigation area, m_{ij} ($m^3.ha^{-1}$) is the irrigation discharge of the i^{th} plant at the j^{th} irrigation time, and t_{ij} (days) is the time for m_{ij} irrigation. Evapotranspiration in the dry season is higher than in

Table 2. Lower Mekong mainstream monthly discharge 1960 to 2004 ($m^3.s^{-1}$).

Sites / Month	Mainstream sites						
	Chiang Saen	*Luang Prabang*	*Vientiane*	*Nakhon Phanom*	*Mukdahan*	*Pakse*	*Kratie*
January	1,150	1,690	1,760	2,380	2,370	2,800	3,620
February	930	1,280	1,370	1,860	1,880	2,170	2,730
March	830	1,060	1,170	1,560	1,600	1,840	2,290
April	910	1,110	1,190	1,530	1,560	1,800	2,220
May	1,300	1,570	1,720	2,410	2,430	2,920	3,640
June	2,460	3,110	3,410	6,610	7,090	8,810	11,200
July	4,720	6,400	6,920	12,800	13,600	16,600	22,200
August	6,480	9,920	11,000	19,100	20,600	26,200	35,500
September	5,510	8,990	10,800	18,500	19,800	26,300	36,700
October	3,840	5,750	6,800	10,200	10,900	15,400	22,000
November	2,510	3,790	4,230	5,410	5,710	7,780	10,900
December	1,590	2,400	2,560	3,340	3,410	4,190	5,710

Data source [11].

the rainy season and the available water discharge from the Mekong river to the delta is lower in the dry season, therefore this paper focuses on the estimation of the water requirement for the Winter-Spring rice crop.

In this study, the meteorological data for a 10-year series of water requirement calculations are collected from the provincial ueather stations of An Giang, Can Tho, and Soc Trang which serve as three rice production regions that represent the flood plain areas, middle areas, and coastal areas, respectively. Hydrological data for water balance analysis during the dry seasons are collected from the Mekong river commission [10, 11]. The monthly discharge from the hydrological stations of the Lower Mekong mainstream from Chiang Saen (in Thailand) to Luang Prabang, Vientiane, Nakhon Phanom, Mukdahan and Pakse (all in Laos) and Kratie (in Cambodia) is presented in Table 2. The mean monthly discharge flows at Tan Chau and Chau Doc (in Vietnam) are available over the period 1979-1996 as presented in Table 3. The soil texture groups of the surveyed fields are from the Provincial Department of Agriculture and Rural Development. Other secondary data, such as reports, papers, and irrigation water utility events from the upstream countries of the Mekong Basin are reviewed for discussion [12-19].

Table 3. Mean monthly flows at Tan Chau (TC) and Chau Doc (CD) Stations ($m^3.s^{-1}$).

St.	Jan.	Feb.	Mar.	Apr.	May.	Jun.	Jul.	Aug.	Sep.	Oct.	Nov.	Dec.
TC	6,220	3,720	2,600	2,010	2,640	7,180	11,270	16,390	21,140	20,340	15,260	10,180
CD	1,360	700	420	330	460	1,450	2,390	3,970	5,200	5,480	4,700	2,710
Tot.	7,580	4,420	3,020	2,340	3,100	8,630	13,660	20,360	25,430	25,820	19,960	12,800

Data source [12].

Results and discussion

Based on the Penman-Monteith equation (Eq. 2), the reference evapotranspiration ET_o calculation results of An Giang, Can Tho, and Soc Trang provinces during the dry seasons are given in Table 4.

Table 4. The reference evapotranspiration in ETo (mm/day) for 6 months of the dry seasons (data taken from 2008-2017).

Province/city	Nov.	Dec.	Jan.	Feb.	Mar.	Apr.
An Giang	3.27	3.04	3.28	4.48	5.43	5.82
Can Tho	3.35	3.16	3.43	4.39	5.21	5.73
Soc Trang	3.32	3.08	3.36	4.35	5.06	5.62

Based on the water balance equations, results from calculated irrigation rate from CROWAT for the Winter-Spring rice crop is 9,500±400 m^3ha^{-1} and the coefficient of irrigation is in the range of 1.36-1.39 $l.s^{-1}ha^{-1}$. When compared with the Vietnamese Standards (TCVN 8641-2011) for the Winter-Spring rice crop in the southern region of Vietnam, the irrigation rate during growing periods should be from 7,500 to 8,000 m^3ha^{-1} [20], excluding the irrigation rate for the land preparation period, which is about 900-1,000 m^3ha^{-1}. The higher calculated irrigation rate can be explained by the higher air temperature in combination with stronger air-wind speeds over the last 10 years resulting in higher evapotranspiration rates, which provides evidence of water insecurity compounded by climate variability.

For other agriculture products (upland crops, aquaculture, and animal husbandry), the water needs are experimentally estimated to be 30-35% [19] of the water amount for rice

cultivation or 594-693 m^3ha^{-1}. In general, the total water taken from the MD's river system for nearly 1,360,000 ha agricultural land during the dry season is approximately 2,500-2,600 m^3s^{-1}, which is the minimum requirement for normal yields.

Considering the mean monthly flow discharges of the Mekong river that passes Pakse (Laos), Kratie (Cambodia), Tan Chau (Vietnam), and Chau Doc (Vietnam) during the dry season, it is easy to find that the expected water requirement for irrigation in the MD is greater than the inflows of the Mekong mainstream. Thus, this figure indicates that this water source during the dry season is the greatest limitation to the extension of cultivation areas not only in the MD but also to other upstream countries.

Conclusions and recommendation

Lowland rice consumes much more water than any other crops. Although this study is based on a rough water balance equation that only uses three places (i.e. An Giang, Can Tho and Soc Trang) along the Hau river, the calculated results show that it is impossible to satisfy this huge water amount for the irrigation of all the rice areas in the Mekong river delta in Vietnam during the dry seasons.

There are many future uncertainties for which scenario-based studies might be required. For example, increasing air temperature, higher solar radiation, stronger wind velocity, less precipitation distribution, extended drought and salinity duration, as well as the effects of present and future agricultural transformation are main factors affecting rice planting areas and the growth of rice. Rice and other crop productivity can be damaged by an increasing scarcity of water resources for irrigation in the future.

When the extreme scenario of historical drought and salinity intrusion occurred in 2016, the cultivation areas in the MD were narrowed down by more than 35.5%. If upstream countries continue to develop their mega-irrigation projects with 3-fold larger irrigated areas than what exists currently, the water supply capacity for rice and upland crops in the delta will decrease dramatically.

In view of economic and social aspects, rice farmers in the Delta will pay more money to pump water when the water level and flow discharge of the Mekong River decreases. Accordingly, their income will be further reduced as a consequence of climate change, water diversion, as well as abnormal operation of hydropower dam projects. The rice production areas must be reduced as what has already been elaborated in resolution 120 of the Government of Vietnam because water and food security for the downstream nations will be threated.

Water for farming should be used as efficiently as possible; the water productivity (crop per drop) should increase and the water profitability (income per litre) should also be increased by switching from rice to high-value crops. The development of water saving methods for farmers in parallel with farming systems improvement and cropping patterns adjustment is strongly recommended. Furthermore, strategic solutions on hydro-diplomacy and the legal and institutional aspects of water resource governance on international, regional, and local scales should be promoted to share both water benefits and risks among all the Mekong countries.

ACKNOWLEDGEMENTS

This study is partly funded by the Can Tho University Improvement Project VN14-P6, and supported by a Japanese ODA loan.

The author declares that there is no conflict of interest regarding the publication of this article.

REFERENCES

[1] General Statistical Office (2016), *Statistical Yearbook of Vietnam*, Statistic Publishing House.

[2] S. Benedikter (2014), "Extending the hydraulic paradigm: reunification, state consolidation and water control in the Vietnamese Mekong delta after 1975", *Southeast Asian Studies*, **3(3)**, pp.547-587.

[3] General Statistical Office (2015), *Statistical Yearbook of Vietnam*, Statistic Publishing House.

[4] http://english.vietnamnet.vn/fms/vietnam-in-photos/151545/drought-and-saltwater-attack-mekong-delta.html.

[5] S.J. Zwart and W.G.M. Bastiaansen (2004), "Reviewed of measured crop productivity values for irrigated wheat, rice, cotton and maize", *Agric. Water Management,* **69**, pp.115-133.

[6] FAO Irrigation and drainage paper 24 (1977), *Crop Water Requirements*, Food and Agriculture Organization of the United Nations, Rome, Italy. ISSN 92-5-100279-7.

[7] T.L. Cosslett, P.D. Cosslett (2018), *Sustainable Development of Rice and Water Resources in Mainland Southeast Asia and Mekong River Basin*. Tables 5.2, 5.3, 5.4 and 5.5. Springer Nature, Singapore.

[8] M. Smith (1992), *CROPWAT: a computer Programme for Irrigation Planning and Management*, FAO Irrigation and Drainage Paper No. 46, Food and Agriculture Organization of the United Nations, Rome, Italy.

[9] R.G. Allen, L.S. Pereira, D. Raes and M. Smith (1998), *Crop Evapotranspiration - Guidelines for Computing Crop Water Requirements*, FAO Irrigation and Drainage Paper No.56, Food and Agriculture Organization of the United Nations, Rome, Italy.

[10] P. Steduto, C.H. Theodore, F. Elias and R. Dirk (2012), *Crop yield Response to Water*, FAO Irrigation and Drainage Paper No.66, Food and Agriculture Organization of the United Nations, Rome, Italy.

[11] MRC (2005), *Overview of the Hydrology of the Mekong Basin*, MRC, Vientiane, 73pp.

[12] MRC (2009), *The Flow of the Mekong*, MRC Management Information booklet series No.2. 12pp.

[13] F. Molle (2005), *Irrigation and Water Policies in the Mekong Region: Current Discourses and Practices*, Colombo, Sri Lanka: IWMI, 43pp (Research report 95).

[14] F. Molle and P. Floch (2007), *Water, Poverty and the Governance of Megaprojects: The Thai "Water Grid"*, Mekong Program on Water, Institut de Recherche pour le Développement, International Water Management Institute. Chiang Mai, Thailand. 30pp.

[15] F. Molle and P. Floch (2008), *The "Desert bloom" Syndrome: Irrigation Development Politics and Ideology in the Northeast of Thailand*, Mekong Program on Water, Institut de Recherche pour le Développement. International Water Management Institute, Chiang Mai, Thailand, 29pp.

[16] ADB (2011), *Lao People's Democratic Republic: Northern Community-Managed Irrigation Sector Project*, Technical Report, 81pp.

[17] C. Boualapha, O. Philavong (2011), "Water planning in Lao PDR", *Water in the Green Economy in Practice: Toward Rio+20*, Zaragora.

[18] F. Molle, T. Foran and M. Kakonen (2012), *Contested Waterscapes in the Mekong Region: Hydropower, Livelihoods and Governance*, Earthscan publishing, 448pp.

[19] R. Johnston, T. Try and S. Silva (2013), *Agricultural Water Management Planning in Cambodia*, WMI - ACIAR Investing in water management to Improve Productivity of Rice-Based Farming systems in Cambodia Project.

[20] MONRE (2011), *TCVN 8641:2011: Hydraulic Structures - Irrigation and Drainage Techniques for Provisions Crops*.

DOI: 10.31276/VJSTE.62(3).62-67

Identification, structural characterization, and *in silico* expression analysis of the sucrose transporter 'SWEET' gene family in peanut (*Arachis hypogaea*)

Ha Duc Chu[1*], Quynh Thi Ngoc Le[2], Yen Hai Thi Hoang[3], Thu Phuong Pham[3], Hong Viet La[3], Nguyet Minh Thi Nguyen[1], Anh Xuan Duong[4], Thao Duc Le[1], Linh Hung Le[1], Hoi Xuan Pham[1]

[1]Agricultural Genetics Institute, Vietnam Academy of Agricultural Sciences
[2]Faculty of Chemistry and Environment, Thuyloi University
[3]Faculty of Biology, Agricultural Technology, Hanoi Pedagogical University 2
[4]Padworth College, United Kingdom

Received 2 March 2020; accepted 29 May 2020

Abstract:

SWEET (Sugars Will Eventually be Exported Transporter) proteins are well known to play pivotal roles in the growth and development of plants. Here, we report the presence of 43 members of the AhSWEET family in peanut (*Arachis hypogaea*) and determine their general characteristics including chromosomal localization, gene structure, and numerous physical and chemical features of the proteins. We found that the *AhSWEET* genes were unevenly distributed among the peanut's 20 chromosomes. The AhSWEET proteins were hydrophobic with a grand average hydropathicity >0 while a majority of the proteins were basic with isoelectric points >7.0. Additionally, most of the *AhSWEET* genes contained 6 exons and 5 introns. The expression profiles of the *AhSWEET* genes were explored based on the previous transcriptome atlas. Interestingly, we found that the *AhSWEET* genes exhibited differential expression patterns across various organs and tissues during the growth and development of peanut plants. Our study provides a solid foundation of the *AhSWEET* gene family for further functional characterization of *AhSWEET* genes in the regulation of peanut growth and development.

Keywords: **bioinformatics, expression profiles, genome-wide, peanut, sucrose transporter, SWEET.**

Classification number: **3.1**

Introduction

Peanut (*Arachis hypogaea*) is considered to be one of the most important legume crops and is mainly cultivated in tropical and subtropical areas. These legumes provide a good source of protein, monounsaturated fats, and antioxidants [1]. Several peanut by-products such as peanut meal, peanut skin, peanut hull, and peanut vine can be used by the food processing industry and consequently play an essential role in food security [2]. However, peanut production and quality are severely affected by abiotic stress [3].

It has been confirmed that the concentration of soluble sugars (predominantly sucrose) can be boosted when plants are exposed to abiotic stress [4, 5]. Of our interest, a group of sucrose transporters, so-called "Sugars Will Eventually be Exported Transporters" or SWEETs, are reported as the functional proteins involved in the translocation of sucrose [6, 7]. Thus, SWEETs regulate numerous biological processes in the growth and development of plants such as nectar secretion, phloem loading and development, and seed filling [7, 8]. Previously, some studies have identified and characterized *SWEET* genes in many main crops such as rice (*Oryza sativa*) [9], soybean (*Glycine max*) [10], sorghum (*Sorghum bicolor*) [11], rapeseed (*Brassica napus*) [12], cotton (*Gossypium* spp.) [13], wheat (*Triticum aestivum*) [14, 15], and litchi (*Litchi chinensis*) [16]. Meanwhile, information from the *SWEET* gene family in peanut is lacking.

Therefore, in this study, the *SWEET* gene family in peanut is identified and characterized based on a bioinformatics approach. Specifically, a comprehensive survey of all putative *SWEET* genes was conducted in the

*Corresponding author: Email: hachu_amser@yahoo.com

peanut genome. Subsequently, the expression profiles of the *SWEET* genes in various organs were generated based on a previous transcriptome atlas.

Materials and methods

Materials

The latest reference genome, proteome, and transcriptome of the peanut ('Tifrunner' cultivar) [17, 18] from the Legume Information System [19] and PeanutBase [18] were used as the platforms for our *in silico* analyses.

Methods

Identification and annotation of the SWEET genes: to identify SWEET proteins in the peanut, we conducted a study in which the domain of the plant's SWEET, namely 'PF03083' [6, 7], obtained from the Pfam server [20], was acquired to search against the recent peanut assembly (BioProject: PRJNA419393) [17] published in NCBI and the Legume Information System [19]. The identified protein sequences were then subjected to a BlastP search against the proteome of the peanut [17] to obtain their necessary annotated information, which includes coding DNA sequence (CDS), genomic DNA sequence (gDNA), and chromosomal localization.

Analysis of characteristics of SWEET proteins: the full-length protein sequences of SWEET proteins were searched against the ExPASy Protparam to obtain general features such as molecular mass, length, instability index, isoelectric point, and grand average of hydropathicity (GRAVY) [21]. An instability index score of <40 and >40 indicates potential stability and instability, respectively. GRAVY values of <0 and >0 suggest hydrophilic and hydrophobic characteristics, respectively [21].

Phylogenetic analysis and gene organization of SWEET genes: a neighbour-joining phylogenetic tree comprised of the full-length amino acid sequences of all identified SWEET proteins was constructed with the aid of MEGA (Molecular Evolutionary Genetics Analysis) 7.0 [22] using the following essential criteria: a gap extension penalty of 0.2 and a gap open penalty of 10 [23]. Bootstrapping was performed with 1,000 replications. The exon/intron structure of each *SWEET* gene was analysed by subjecting the CDS and corresponding gDNA to the GSDS (Gene Structure Display Server) 2.0 tool [24].

Expression profiles of SWEET genes: the PeanutBase database was explored to provide a previous transcriptome atlas of different tissues/organs in the peanut [18]. Particularly, data from seven vegetative plant parts, including vegetative shoot tips, reproductive shoot tips, primary stem leaves, seedling leaves, lateral stem leaves, roots, and nodules were collected. The cluster heatmap for the relative expression of the *SWEET* gene was visualized in *R* software with the gplots package [25].

Results and discussion

Identification and annotation of the SWEET gene family in peanut

To identify all potential members of the SWEET family in the peanut, a comprehensive search of a well-established conserved domain of SWEETs [6, 7] against the newest peanut database [17] was performed. As a result, a total of 43 members of the SWEET family were found in the peanut. The annotation of these identified proteins, including protein identifiers and locus name, are subsequently explored and listed in Table 1. Previously, the *SWEET* gene family has been reported in several plant species. More specifically, 21 members of the *OsSWEET* family have been investigated in rice [9], while 52 and 23 *SWEET* genes have been found in soybean and sorghum, respectively [10, 11]. Recently, it has been reported that the *SWEET* gene family in rapeseed contained 68 members [12]. In the cotton species, the members of the *SWEET* gene family varied from 22 to 60 [13]. Our results indicated that the number of *SWEET* genes in plant species is highly variable.

Next, to annotate the chromosomal localization of the *SWEET* genes, we matched their corresponding gDNA sequence to the peanut genome [17]. We found that all members of the *SWEET* genes were randomly distributed among the 20 chromosomes of the peanut genome and no *SWEET* gene was localized in unplaced scaffolds (Fig. 1). Among them, chromosome Arahy.13 and Arahy.03 share the highest members of the *SWEET* family by 6 and 5 genes, respectively (Fig. 1). Additionally, there are 4 *SWEET* genes found in chromosome Arahy.08, while the chromosomes Arahy.14, 15, 16, 17, and 18 have 3 *SWEET* genes (Fig. 1). We also found that 2 *SWEET* genes were mapped on each of chromosomes Arahy.05, 06, and 20, while only 1 *SWEET* gene was reported in chromosomes Arahy.01, 04, 07, 09, 10, 11, and 19 (Fig. 1). It is also noted that no *SWEET* gene was localized in chromosomes Arahy.02 and 12 (Fig. 1). The entire 43 *SWEET* genes set was based on the order of the occurrences on the chromosomes (Table 1, Fig. 1).

Table 1. General information on *SWEET* gene family in the peanut.

#	Gene name	Protein code	Locus code	Size	MM	pI	II	GRAVY
1	*AhSWEET01*	XP_025675869.1	LOC112776072	227	25.81	8.82	43.35	0.96
2	*AhSWEET02*	XP_025689387.1	LOC112790966	279	31.48	8.99	38.23	0.46
3	*AhSWEET03*	XP_025689047.1	LOC112790726	253	27.92	9.37	46.63	0.56
4	*AhSWEET04*	XP_025676850.1	LOC112776807	159	18.23	9.74	33.58	0.87
5	*AhSWEET05*	XP_025691262.1	LOC112792298	293	32.86	8.49	31.46	0.48
6	*AhSWEET06*	XP_025691265.1	LOC112792300	220	25.04	9.68	28.98	1.05
7	*AhSWEET07*	XP_029153458.1	LOC112795203	175	20.21	9.83	38.61	0.82
8	*AhSWEET08*	XP_025697629.1	LOC112799834	250	27.59	9.19	32.87	0.72
9	*AhSWEET09*	XP_025697627.1	LOC112799832	242	26.85	8.68	37.49	0.80
10	*AhSWEET10*	XP_025606390.1	LOC112697429	244	26.70	8.91	32.98	0.78
11	*AhSWEET11*	XP_025603714.1	LOC112695553	312	34.23	9.15	21.70	0.41
12	*AhSWEET12*	XP_025610780.1	LOC112703520	235	26.20	8.38	44.42	0.84
13	*AhSWEET13*	XP_025612828.1	LOC112705985	246	27.12	9.30	32.96	0.64
14	*AhSWEET14*	XP_025612772.1	LOC112705945	262	29.03	9.02	27.45	0.51
15	*AhSWEET15*	XP_025616058.1	LOC112708127	301	34.32	8.84	51.86	0.10
16	*AhSWEET16*	XP_025616059.1	LOC112708128	285	32.77	9.05	39.49	0.40
17	*AhSWEET17*	XP_025616659.1	LOC112708960	320	35.26	8.34	34.39	0.70
18	*AhSWEET18*	XP_025622395.1	LOC112714914	292	32.46	8.82	33.82	0.66
19	*AhSWEET19*	XP_025629145.1	LOC112722363	226	25.74	8.82	43.49	0.95
20	*AhSWEET20*	XP_025641347.1	LOC112736207	261	29.73	6.99	41.81	0.53
21	*AhSWEET21*	XP_025637471.1	LOC112732876	278	31.37	9.09	38.33	0.48
22	*AhSWEET22*	XP_025637469.1	LOC112732875	249	28.29	9.71	33.13	0.84
23	*AhSWEET23*	XP_025636904.1	LOC112732406	253	27.90	9.37	46.29	0.56
24	*AhSWEET24*	XP_025639618.1	LOC112734493	293	32.90	8.97	32.73	0.48
25	*AhSWEET25*	XP_025639626.1	LOC112734496	225	25.30	9.66	31.43	1.00
26	*AhSWEET26*	XP_025650623.1	LOC112745021	274	30.31	8.95	35.74	0.60
27	*AhSWEET27*	XP_025646602.1	LOC112741728	200	21.71	8.46	30.60	0.58
28	*AhSWEET28*	XP_025650514.1	LOC112744946	261	29.73	6.99	41.08	0.54
29	*AhSWEET29*	XP_025655604.1	LOC112750900	248	27.61	8.72	36.50	0.68
30	*AhSWEET30*	XP_025655423.1	LOC112750786	250	27.76	9.18	33.60	0.71
31	*AhSWEET31*	XP_025650947.1	LOC112747164	242	26.89	8.84	38.20	0.80
32	*AhSWEET32*	XP_025659195.1	LOC112755367	268	29.33	9.16	24.33	0.44
33	*AhSWEET33*	XP_025662459.1	LOC112758096	310	34.17	9.22	25.22	0.36
34	*AhSWEET34*	XP_025659173.1	LOC112755353	244	26.62	9.22	32.26	0.77
35	*AhSWEET35*	XP_025667967.1	LOC112766275	262	28.88	9.01	28.76	0.54
36	*AhSWEET36*	XP_025664711.1	LOC112763193	104	11.33	6.51	38.82	0.65
37	*AhSWEET37*	XP_025666957.1	LOC112765256	246	26.95	9.30	34.20	0.64
38	*AhSWEET38*	XP_025672359.1	LOC112771761	235	26.10	7.62	43.28	0.86
39	*AhSWEET39*	XP_025673457.1	LOC112772695	301	34.38	8.71	57.28	0.10
40	*AhSWEET40*	XP_025672677.1	LOC112772012	287	33.01	9.05	39.29	0.38
41	*AhSWEET41*	XP_025679981.1	LOC112779842	281	31.26	8.47	40.94	0.78
42	*AhSWEET42*	XP_025685723.1	LOC112786568	248	27.49	8.84	36.64	0.81
43	*AhSWEET43*	XP_025683874.1	LOC112784769	292	32.52	8.81	35.55	0.65

Note: MM: molecular mass (kDa), pI: isoelectric point, II: instability index, GRAVY: grand average of hydropathicity.

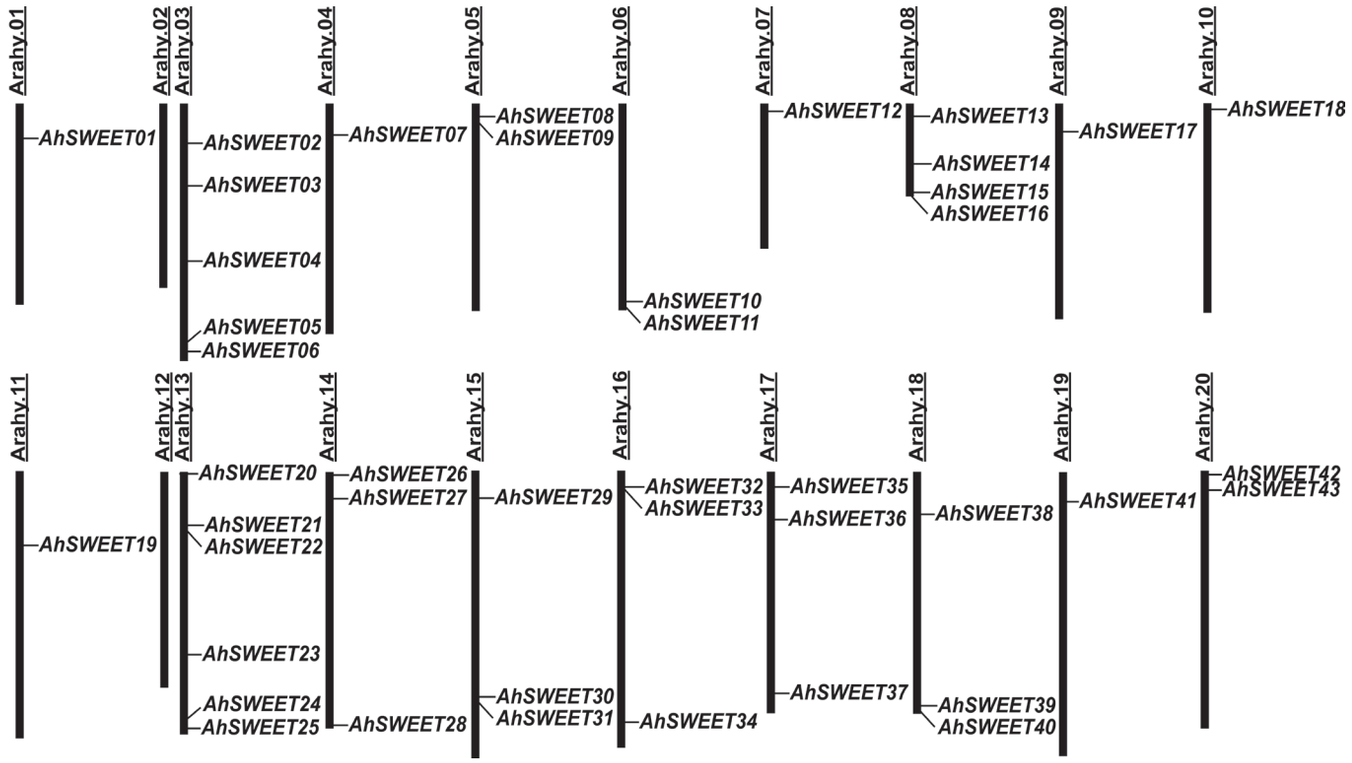

Fig. 1. Chromosomal distribution of *AhSWEET* genes in peanut. Chromosomal localization of 43 *AhSWEET* genes was based on the latest physical map described in NCBI and the Legume Information System.

Structural analysis of the SWEET gene family in peanut

The exon/intron organization of each *AhSWEET* gene was first analysed in order to gain insight into the *AhSWEET* gene family. As shown in Fig. 2, the most common motif of the gene structure of the *AhSWEET* family was 6 exons/5 introns. Only *AhSWEET41* and *AhSWEET36* contained 2 exons/1 intron and 3 exons/2 introns, respectively, while 3 genes, including *AhSWEET04*, *07*, *17* had 4 exons/3 introns (Fig. 2). Our findings were also confirmed by previous studies [10, 12-15, 26]. More specifically, a total of 34 (out of 52) *GmSWEET*s was recorded to contain 6 exons/5 introns [10], while the majority of *BnSWEET*s (51 out of 68) also had 6 exons/5 introns [12]. This phenomenon was also reported in other plant species such as cotton [13], wheat [14, 15], and litchi [16]. Taken together, it would be a reliable assumption that the general structure of *SWEET* genes in higher plant species is 6 exons/5 introns.

Next, the full-length protein sequence of each SWEET was used for retrieval from the ExPASY Protparam [21] in order to analyse the general features of the SWEET family in the peanut. The length of the SWEET proteins varied

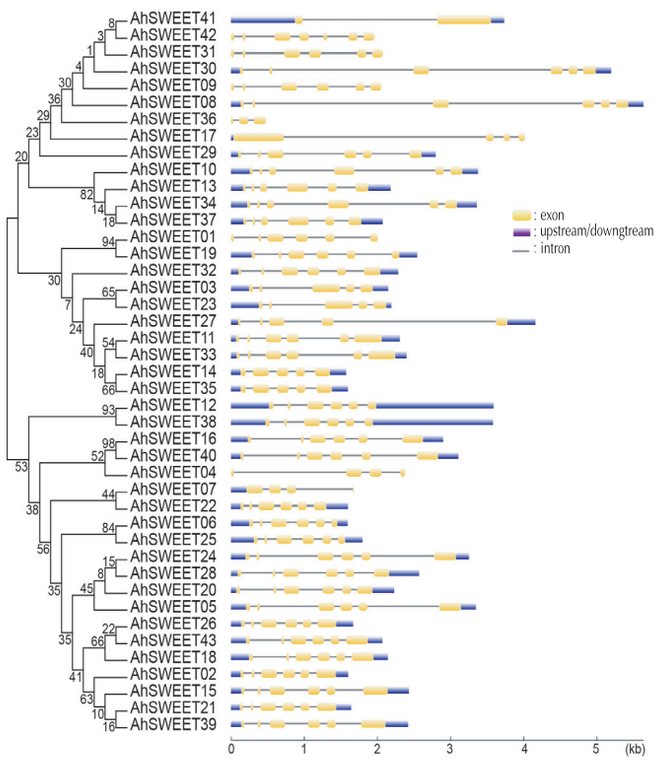

Fig. 2. Gene structure of *AhSWEET* gene family. An unrooted neighbour-joining tree was derived from the full-length AhSWEET sequences (left) and exon/intron organization analysis (right).

from 104 (AhSWEET36) to 320 residues (AhSWEET17) with their molecular masses ranging from 11.33 to 35.26 kDa, respectively (Table 1). The pI values of a majority of the SWEET proteins were >7, which revealed that these proteins were basic whereas only AhSWEET36 was acidic (pI=6.51) (Table 1). The two remaining SWEET proteins, AhSWEET20 and 28, were neutral (pI≈7) (Table 1). We also found that 32 SWEET proteins were stable (instability score <40) (Table 1). Furthermore, all 43 SWEET proteins were hydrophobic with a GRAVY value >0 (Table 1).

Previously, the characteristics of SWEET proteins have also been investigated in other plant species. For example, the SWEET proteins in rapeseed varied from 56 to 303 residues, while their molecular weight ranged from 6.5 to 33.45 kDa [12]. A total of 63 members (out of 68) of SWEET proteins were basic [12]. Additionally, most of the identified cotton's SWEET proteins ranged between 180 and 311 residues, while the molecular masses and isoelectric values of these proteins varied from 9.93 to 38.04 kDa and from 5.47 to 10.08, respectively [13]. In wheat, the molecular weights of SWEET proteins ranged from 10.93 to 33.86 kDa, while a majority of members in the SWEET family exhibited pI values >7 (basic) [14, 15]. Recently, the sizes and molecular weights of the LcSWEET proteins have been found to vary from 229 to 300 residues and from 25.6 to 33.6 kDa, respectively, while the pI values ranged from 7.66 to 9.81 [16]. Our findings suggest a diversity of molecular features of SWEETs in the peanut and perhaps in the plant species.

Expression profiles of AhSWEET genes in various tissues

To understand the expression patterns of the *AhSWEET* gene family, we visualized the transcriptome data obtained from 7 tissues respectively taken from vegetative shoot tip, reproductive shoot tip, main stem leaf, seedling leaf, lateral stem leaf, root, and nodule [18] by R programming with the gplots package [25]. We found that 17 genes, including *AhSWEET03*, *04*, *07*, *10*, *14*, *17*, *18*, *20*, *21*, *23*, *31*, *34*, *35*, *36*, *39*, *41*, and *42*, had no information on the expression profiles. The expressions of the remaining *AhSWEET* genes are displayed in Fig. 3.

Among them, 11 *AhSWEET* genes had no changes in the transcriptional levels of the 7 collected tissues (Fig. 3). Interestingly, *AhSWEET02* was noted to exclusively express in 3 samples of leaves and the reproductive shoot tip, while *AhSWEET15* was also strongly induced in lateral stem leaves, seeding leaves, and main stem leaves (Fig. 3). *AhSWEET27* was found to be strongly up-regulated in both

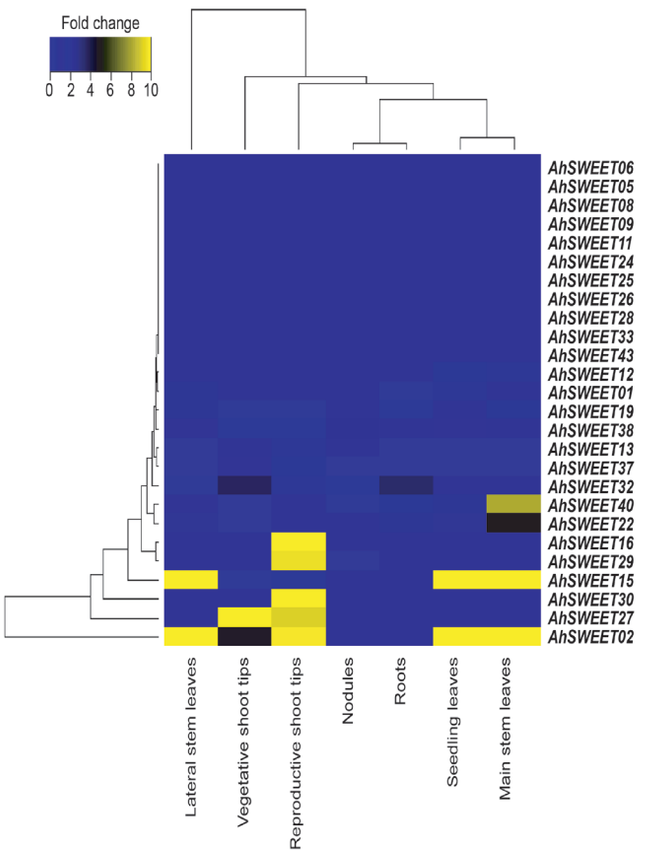

Fig. 3. Expression profiles of the *AhSWEET* genes in various tissues. The heat map was generated using R software with the gplots package. The detailed microarray data were obtained from the peanut gene atlas database.

reproductive and vegetative shoot tips (Fig. 3). In some cases, the *AhSWEET* genes were down-regulated in organs/tissues during the growth and development of the peanut plants. For example, *AhSWEET13* and *37* were recorded to be strongly reduced in lateral stem leaves, seeding leaves, and main stem leaves (Fig. 3). Taken together, the *AhSWEET* genes displayed differential transcription patterns in the investigated organs. Our results suggest that AhSWEET proteins might have diverse functions in controlling the development of various organs in peanut plants.

Conclusions

In this study, 43 *AhSWEET* genes have been identified in the peanut genome. Structural analyses revealed that the AhSWEET proteins were highly variable. Our expression re-analysis showed that the *AhSWEET* genes displayed differential expression levels in various organs. Two genes, *AhSWEET02* and *15*, were noted to strongly express in leaves and *AhSWEET27* was strongly induced in shoot tips, which indicate that these genes might play crucial roles

in these organs during the growth and development of the peanut.

The authors declare that there is no conflict of interest regarding the publication of this article.

REFERENCES

[1] O.T. Toomer (2018), "Nutritional chemistry of the peanut (*Arachis hypogaea*)", *Crit. Rev. Food Sci. Nutr.*, **58(17)**, pp.3042-3053.

[2] X. Zhao, J. Chen, F. Du (2012), "Potential use of peanut by-products in food processing: a review", *J. Food Sci. Technol.*, **49(5)**, pp.521-529.

[3] D.M. Kambiranda, et al. (2011), "Impact of drought stress on peanut (*Arachis hypogaea* L.) productivity and food safety", *Plants Environ*., Tech Publisher, pp.249-272.

[4] P.V. Minorsky (2003), "Raffinose oligosaccharides", *Plant Physiol.*, **131(3)**, pp.1159-1160.

[5] M.R. Morsy, L. Jouve, J.F. Hausman, L. Hoffmann, J.M. Stewart (2007), "Alteration of oxidative and carbohydrate metabolism under abiotic stress in two rice (*Oryza sativa* L.) genotypes contrasting in chilling tolerance", *J. Plant Physiol.*, **164(2)**, pp.157-167.

[6] B.T. Julius, K.A. Leach, T.M. Tran, R.A. Mertz, D.M. Braun (2017), "Sugar transporters in plants: new insights and discoveries", *Plant Cell Physiol.*, **58(9)**, pp.1442-1460.

[7] R.F. Baker, K.A. Leach, D.M. Braun (2012), "SWEET as sugar: new sucrose effluxers in plants", *Mol. Plant*, **5(4)**, pp.766-768.

[8] L.Q. Chen (2014), "SWEET sugar transporters for phloem transport and pathogen nutrition", *New Phytol.*, **201(4)**, pp.1150-1155.

[9] M. Yuan, S. Wang (2013), "Rice MtN3/saliva/SWEET family genes and their homologs in cellular organisms", *Mol. Plant*, **6(3)**, pp.665-674.

[10] G. Patil, et al. (2015), "Soybean (*Glycine max*) *SWEET* gene family: insights through comparative genomics, transcriptome profiling and whole genome re-sequence analysis", *BMC Genomics*, **16**, DOI: 10.1186/s12864-015-1730-y.

[11] H. Mizuno, S. Kasuga, H. Kawahigashi (2016), "The sorghum SWEET gene family: stem sucrose accumulation as revealed through transcriptome profiling", *Biotechnol. Biofuels*, **9**, DOI: 10.1186/s13068-016-0546-6.

[12] H. Jian, et al. (2016), "Genome-wide analysis and expression profiling of the SUC and SWEET gene families of sucrose transporters in oilseed rape (*Brassica napus* L.)", *Front. Plant Sci.*, **7**, DOI: 10.3389/fpls.2016.01464.

[13] L. Zhao, et al. (2018), "A genome-wide analysis of *SWEET* gene family in cotton and their expressions under different stresses", *J. Cotton Res.*, **1(1)**, DOI: 10.1186/s42397-018-0007-9.

[14] Y. Gao, et al. (2018), "Genome-wide identification of the *SWEET* gene family in wheat", *Gene*, **642**, pp.284-292.

[15] T. Gautam, et al. (2019), "Further studies on sugar transporter (*SWEET*) genes in wheat (*Triticum aestivum* L.)", *Mol. Biol. Reps.*, **46(2)**, pp.2327-2353.

[16] H. Xie, et al. (2019), "Genome-wide identification and expression analysis of *SWEET* gene family in *Litchi chinensis* reveal the involvement of LcSWEET2a/3b in early seed development", *BMC Plant Biol.*, **19(1)**, DOI: 10.1186/s12870-019-2120-4.

[17] D.J. Bertioli, et al. (2019), "The genome sequence of segmental allotetraploid peanut *Arachis hypogaea*", *Nat. Genet.*, **51(5)**, pp.877-884.

[18] J. Clevenger, Y. Chu, B. Scheffler, P. Ozias-Akins (2016), "A developmental transcriptome map for allotetraploid *Arachis hypogaea*", *Front. Plant Sci.*, **7**, DOI: 10.3389/fpls.2016.01446.

[19] S. Dash, et al. (2016), "Legume information system (LegumeInfo.org): a key component of a set of federated data resources for the legume family", *Nucleic Acids Res.*, **44(D1)**, pp.1181-1188.

[20] S. El-Gebali, et al. (2019), "The pfam protein families database in 2019", *Nucleic Acids Res.*, **47(D1)**, pp.427-432.

[21] E. Gasteiger, A. Gattiker, C. Hoogland, I. Ivanyi, R.D. Appel, A. Bairoch (2003), "ExPASy: the proteomics server for in-depth protein knowledge and analysis", *Nucleic Acids Res.*, **31(13)**, pp.3784-3788.

[22] S. Kumar, G. Stecher, K. Tamura (2016), "MEGA7: molecular evolutionary genetics analysis version 7.0 for bigger datasets", *Mol. Biol. Evol.*, **33(7)**, pp.1870-1874.

[23] H.D. Chu, K.H. Nguyen, Y. Watanabe, D.T. Le, T.L.T. Pham, K. Mochida, L.P. Tran (2018), "Identification, structural characterization and gene expression analysis of members of the nuclear factor-Y family in chickpea (*Cicer arietinum* L.) under dehydration and abscisic acid treatments", *Int. J. Mol. Sci.*, **19(11)**, DOI: 10.3390/ijms19113290.

[24] B. Hu, J. Jin, A.Y. Guo, H. Zhang, J. Luo, G. Gao (2015), "GSDS 2.0: an upgraded gene feature visualization server", *Bioinformatics*, **31(8)**, pp.1296-1297.

[25] Y. Liao, G.K. Smyth, W. Shi (2019), "The R package Rsubread is easier, faster, cheaper and better for alignment and quantification of RNA sequencing reads", *Nucleic Acids Res.*, **47(8)**, DOI: 10.1093/nar/gkz114.

[26] H. Miao, et al. (2017), "Genome-wide analyses of SWEET family proteins reveal involvement in fruit development and abiotic/biotic stress responses in banana", *Sci. Rep.*, **7(1)**, DOI: 10.1038/s41598-017-03872-w.

DOI: 10.31276/VJSTE.62(3).68-69

Mycetia hirta Hutch. (Rubiaceae), a new record for the flora of Vietnam

Vu Tien Chinh[1*], Nguyen Quoc Binh[1], Tran Van Hai[3]

[1]Vietnam National Museum of Nature, Vietnam Academy of Science and Technology
[2]Graduate University of Science and Technology, Vietnam Academy of Science and Technology
[3]Vietnam Academy of Science and Technology

Received 20 April 2020; accepted 28 July 2020

Abstract:

A newly recorded species, *Mycetia hirta* Hutch. (Rubiaceae) was reported from Muong Phang district, Dien Bien province in northern Vietnam. It is distinguished from the closely related species, *M. longifolia*, by its hairy stem and leaf blades, much shorter corolla tube and hirtellous calyx and corolla. Morphological description and color photographs of *M. hirta* Hutch. are provided.

Keywords: ***Mycetia*, *Mycetia hirta*, new record, Rubiaceae, Vietnam**.

Classification number: **3.4**

Introduction

The genus *Mycetia*, comprising approximately 45 species, is distributed in tropical to subtropical Asia. 15 species are recorded from China [1], and four species from Laos [2]. The genus has been taxonomically studied by several authors [3, 4] and currently known with two species distributed in Vietnam.

During a recent fieldwork to Muong Phang district, Dien Bien province in northern Vietnam, the first and the third author found an unrecorded species of *Mycetia* in Vietnam and collected specimens. This species is similar to *M. longifolia* (Wall.) Kuntze, but can be differentiated by its hairy stem and leaf blades, much shorter corolla tube and hirtellous calyx and corolla. After refering to related literature and type specimens, we found that this species should be *M. hirta* Hutch. and never recorded from Vietnam. The detailed comparision of *M. hirta* and *M. longifolia* was given in Table 1.

Table 1. Morphological comparison of *M. hirta* with *M. longifolia*.

Morphological characters	*M. hirta*	*M. longifolia*
Height	1-1.5 m tall	to 2 m tall
Leaf blade	oblong-elliptic to elliptic sometimes ovate, 8-23×4-8.5 cm, both surfaces moderately to densely hispidulous	elliptic-lanceolate or elliptic, 5-18(-35)×3-7(-10) cm, adaxially sparsely strigillose, hispidulous, or glabrous
Peduncle	0.7-3.3 cm; branched portion 2-8×2.3-9 cm	0.5-1.5 cm, branched portion 3-4×5-6 cm
Calyx	densely hirtellous, hypanthium ca. 2 mm long	glabrous; hypanthium ca. 1.5-2 mm long
Corolla	outside sparsely to densely villosulous or hirtellous, tube 5-6.2 mm	outside glabrous to villosulous, tube 10-14 mm

*Corresponding author: Email: vtchinh@vnmn.vast.vn

Results and discussion

M. hirta Hutch. is here described as a new record in Vietnam.

Mycetia hirta Hutch. in Sargent, Pl. Wilson. 3: 410. 1916. Type: China, Yunnan, Simao, A. Henry 12299 (holotype, K photo!, isotype, US photo!).

Shrubs, 1-1.5 m tall; stem hairy. Petiole 0.8-3.5 cm, densely villosulous to hirtellous; blade drying papery, oblong-elliptic to elliptic, 8-23×4-8.5 cm, both surfaces moderately to densely hispidulous, base obtuse to acute, apex acute; secondary veins 12-23 pairs; stipules usually persistent with leaves, oblong-lanceolate to ovate, 1-1.5 cm. Inflorescences terminal, several to many flowered, densely villosulous or hirtellous; peduncle 0.7-3.3 cm; branched portion 2-8×2.3-9 cm; bracts ovate, lanceolate, suborbicular, reniform, 2-9 mm, often marginally sparsely to densely stipitate-glandular; pedicels 1.5-4 mm. Flowers pedicellate. Calyx densely hirtellous, hypanthium ca. 2.3 mm; limb deeply lobed; lobes broadly triangular, 2-2.6 mm, marginally densely stipitate-glandular and sometimes appearing lacerate, glands 0.3-0.6 mm. Corolla yellow, tubular, outside sparsely to densely villosulous or hirtellous; tube 5-6.2 mm, sparsely villous inside; lobes triangular, 1-1.8 mm.

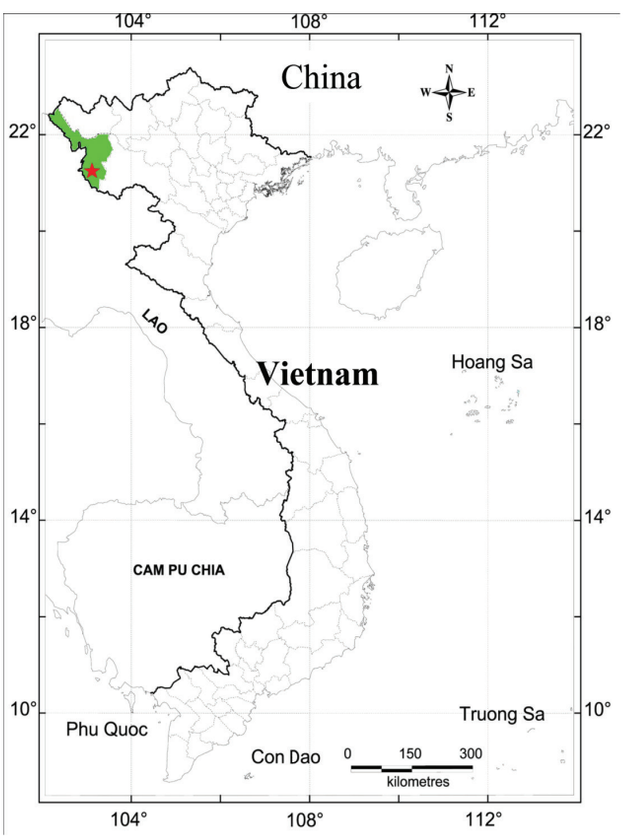

Fig. 1. Map showing the location of *M. hirta* Hutch. in Vietnam (indicated by the red star).

Distribution: northern Vietnam (Dien Bien), China (Hainan, Yunnan).

Ecology and habitat: the species grows in shade of secondary forests at 400-600 m alt.

Specimen examined: northern Vietnam, Dien Bien province, Muong Phang District, 5 June 2005, Nguyen Quoc Binh VN 1542 [HN]; 10 July 2006, Nguyen Quoc Binh QB 521 [VNMN] (Figs. 1 and 2).

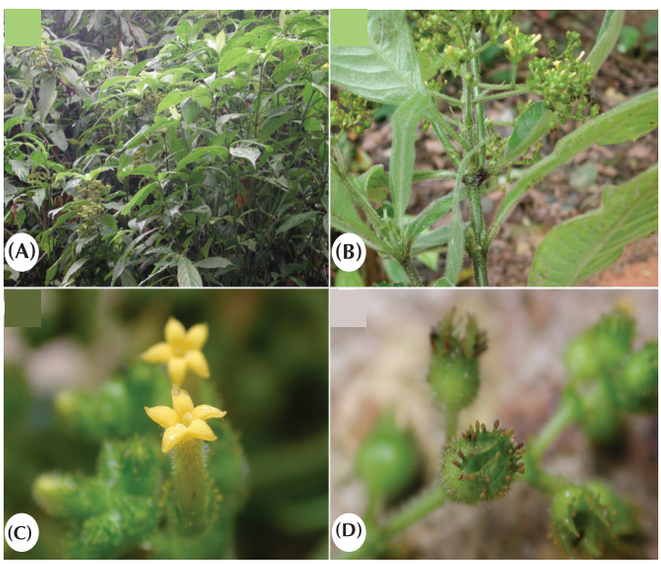

Fig. 2. *M. hirta* Hutch. (A) Habit, **(B)** Inflorescence, **(C)** Flower, **(D)** Fruit (photographed by Nguyen Quoc Binh from Dien Bien province).

The authors declare that there is no conflict of interest regarding the publication of this article.

REFERENCES

[1] T. Chen, et al. (2011), *Flora of China*, Science Press & St. Louis, Missouri Botanical Garden Press.

[2] M. Newman, et al. (2007), *A Checklist of the Vascular Plants of Lao PDR*, Royal Botanic Garden Edinburgh.

[3] Pham Hoang Ho (2000), *An Illustrated Flora of Vietnam*, Tre Publishing House.

[4] Nguyen Tien Ban, Tran Ngoc Ninh (2005), *Checklist of Plant Species of Vietnam*, Agriculture Publishing House.

DOI: 10.31276/VJSTE.62(3).70-75

The antifungal activity of essential oils from some plants in Vietnam against the pathogenic fungi *Candida albicans* and *Aspergillus fumigatus*

Vu Xuan Tao[1*], Tran Bao Tram[1], Nguyen Thi Hien[1], Thai Hanh Dung[2], Tran Van Tuan[2]

[1]*Center of Experimental Biology, National Center for Technological Progress, Ministry of Science and Technology*
[2]*Faculty of Biology, University of Science, Vietnam National University, Hanoi*

Received 15 April 2020; accepted 25 June 2020

Abstract:

Vietnam possesses an abundant and highly diverse resource of plants. Therefore, the search and evaluation of bioactive compounds extracted from these plants are a potential research direction to support developing products that improve human health. The purpose of this study is to assess the antifungal activity of some essential oils produced by materials harvested in Vietnam such as King orange peel (*Citrus sinensis*), lemongrass (*Cymbopogon flexuosus*), peppermint (*Mentha arvensis*), and betel leaf (*Piper betle*). The antifungal effect of these essential oils was determined by the Kirby-Bauer disc diffusion technique. In addition, the antifungal properties of the essential oils were also assessed through their effects on the reproduction of *C. albicans* and the spore germination, mycelium elongation, and sporulation of *A. fumigatus*. The results demonstrated that all peppermint, lemongrass, and betel leaf essential oils showed antifungal activity against *C. albicans* and *A. fumigatus*. Especially, betel leaf essential oil could perform antifungal activity at a low dilution concentration of 10% and could also inhibit the reproduction of *C. albicans* and the spore germination, mycelium elongation, and sporulation of *A. fumigatus*. Meanwhile, orange peel essential oil did not exhibit any antifungal properties.

Keywords: **antifungal activity, *Aspergillus fumigatus*, *Candida albicans*, essential oil.**

Classification number: **3.5**

Introduction

Nowadays, pathogenic microorganisms causing diseases in humans are highly diverse and complex. Besides bacteria and viruses, which have been widely known as common pathogens, micro-fungi are also reported to be responsible for several dangerous diseases. Due to the improper use of antibiotics, overdose of immunosuppressive drugs, the increasing number of immunodeficiency diseases, and the poor living conditions, poor nutrition, and lack of hygiene, fungi now have more chances to spread and function as factors of infection. *Candida albicans* and *Aspergillus fumigatus* are two opportunistic pathogens in humans, especially in immunocompromised individuals. For instance, up to 90% of HIV patients are infected with *Candida* [1]. *C. albicans* is a common micro-fungus causing vaginal infection in women, which accounts for 85-90% of fungal infection causes. Severe illnesses can lead to complications such as endometritis, oophoritis, and infertility [1, 2]. *A. fumigatus* has been recorded as a fungus causing respiratory infection, especially in the lungs, and its function is affected by the immune status of the human body [3, 4].

Currently, the control of these pathogenic fungi mainly depends on antifungal chemicals. The use of natural active ingredients such as essential oils has not been extensively studied. Essential oils are secondary metabolites synthesized by various plant organs such as flowers, leaves, stems, and seeds and are often characterized by a specific odour. Vietnam is one of the countries possessing the most abundant and diverse plant resources. The study of active compounds extracted from medicinal materials is a potential research direction to support developing products to improve human health. A number of studies have proved that essential oil is resistant to many pathogenic microorganisms. The resistance to pathogenic fungi of essential oils greatly

[*]*Corresponding author: Email: taovx.tsa@gmail.com*

depends on their chemical composition, specifically two main components including terpenoids and phenolics [5]. This study was conducted with the aim to assess the antifungal activity of four types of essential oils extracted from the King orange peel (*Citrus sinensis*), lemongrass (*Cymbopogon flexuosus*), peppermint (*Mentha Arvensis*), and betel leaf (*Piper betle*) on the two human pathogenic fungi *C. albicans* and *A. fumigatus*.

Materials and methods

Materials

C. albicans JCM2070 was provided by the Japan Collection of Microorganisms and *A. fumigatus* VTCC1414 was provided by the Vietnam Type Culture Collection, Institute of Microbiology and Biotechnology (IMBT), Vietnam National University, Hanoi. These two strains of fungi were kept in the Genomics Unit, The Key Laboratory of Enzyme and Protein Technology, VNU University of Science, Vietnam National University, Hanoi.

Essential oils were collected by the method of steam distillation from raw materials collected in Vietnam. Essential oil samples of King orange peel (*Citrus sinensis*), lemongrass (*Cymbopogon flexuosus*), peppermint (*Mentha arvensis*), and betel leaf (*Piper betle*) were provided by the Center of Experimental Biology, National Center for Technological Progress, Ministry of Science and Technology.

Methods

Preparation of fungal spores: the *A. fumigatus* strain of VTCC1414 was cultured on PDA. After 5 d of cultivation at 28°C, sterile distilled water was added to the surface of the dish, then a clean sterile squeegee was used to remove the spores from the mycelium. The collected fluid was filtered through a Miracloth filter (Calbiochem, Germany) and centrifuged at a rate of 4000 rpm for 10 min and the clear supernatant was then discarded. The spores were washed twice with sterile distilled water. The sediment after centrifugation containing fungal spores was dissolved in sterile distilled water and adjusted to a concentration of 10^6 spores/ml using a Thoma counting chamber [6]. For the *C. albicans* JCM2070 strain, the strain was cultured on liquid Hansen medium. The cell density of the culture fluid was also determined by a Thoma cell counting chamber and was adjusted to a concentration of 10^7 cells/ml.

Evaluation of antifungal activity: the test to assess antifungal activity was conducted with the Kirby-Bauer disc diffusion technique [7]. A 30 µl spore suspension of *A. fumigatus* VTCC1414 and *C. albicans* JCM2070 were cultured on PDA and Hansen media, respectively. Each plate was placed with a sterile blotting paper (6 mm in diameter). A 20 µl drop of betel leaf oil was added dropwise onto a sterile paper disc and left for 60 s. Each essential oil was diluted with DMSO 5% to the concentrations of 5, 10, 20, 30, 40, and 50% [8]. The Petri dishes were then kept at 4°C for essential oil diffusion for 4 h. With *A. fumigatus* VTCC1414, all petri dishes were incubated at 28°C for 4-5 d. With *C. albicans* JCM2070, all petri dishes were incubated at 37°C for 1-2 d. The antifungal activity of each type was calculated according to the size of the inhibition zone.

Evaluation the effects of essential oil on the reproduction of C. albicans JCM2070: the medium used was liquid Hansen medium. Essential oils were added to the media to the concentrations of 0.025, 0.05, 0.075, and 0.1%. The initial cell density of *C. albicans* JCM2070 was 1.75×10^6 cells/ml. The strain was cultivated at 37°C at the rate of 200 rpm. Cell density monitoring was conducted after intervals of 2, 4, and 6 h by dilution and inoculation on Hansen medium.

Assessing the effects of essential oil on the development of A. fumigatus mycelium VTCC1414: the slide culture technique was used, and observations were made under an Olympus optical microscope [9]. Essential oils were mixed into the PDA medium to the concentrations of 0.025, 0.05, 0.075, and 0.1 %. PDA media containing essential oils were used to cultivate fungi. Samples were incubated at 28°C and observed after 24 and 48 h.

Results and discussion

The antifungal activity of essential oils against C. albicans and A. fumigatus

Four types of essential oils, including King orange peel, lemongrass, peppermint, and betel leaf, were evaluated for their ability to resist against *C. albicans* and *A. fumigatus* with the Kirby-Bauer disc diffusion technique. The results showed that the essential oil from King orange peel did not exhibit any antifungal activities. On the other hand, the three other essential oils including peppermint, lemongrass, and betel leaf all exhibited antifungal activities against *C. albicans* and *A. fumigatus* (see Tables 1, 2 and Figs. 1, 2). With *C. albicans*, the peppermint essential oil (undiluted) and lemongrass essential oil (undiluted and diluted to 50%) completely inhibited the fungal growth (i.e. the fungi did not grow over the whole agar plate medium). However, the peppermint essential oil showed weak antifungal activity against *C. albicans* at a 50% dilution and no longer performed antifungal activity at a 40% dilution. Similarly, the lemongrass essential oil diluted to

Table 1. Antifungal activities of several essential oils against *C. albicans*.

Essential oils	Inhibition zone (mm) at different concentration of essential oils (%)						
	100	*50*	*40*	*30*	*20*	*10*	*5*
King orange peel	-	-	-	-	-	-	-
Peppermint	No fungus growth	5.33±0.58	-	-	-	-	-
Lemongrass	No fungus growth	No fungus growth	18.33±1.15	11.66±1.53	2.33±0.58	-	-
Betel leaf	22.00±1.00	20.67±0.58	15.33±0.58	12.33±1.15	11.67±1.52	7.33±0.58	-

- no inhibition zone exhibited.

a concentration of 20% exhibited weak antifungal activity against *C. albicans* and no antifungal activity at the 10% concentration. Meanwhile, the betel leaf essential oil diluted to a concentration of 20% still showed strong antifungal activity against *C. albicans* and could still perform similarly at 10% concentration. Thus, the betel leaf and lemongrass essential oils can be used to control the spread of *C. albicans*. However, the betel leaf essential oil shows more advantages due to its function even at low concentrations (10%) against *C. albicans*.

The result was similar to that obtained from the evaluation of the resistance abilities of the essential oils mentioned above to *A. fumigatus*. The peppermint essential oil (undiluted) and lemongrass (diluted to 30%) completely inhibited the growth of *A. fumigatus*. The lemongrass essential oil showed strong antifungal activity against *A. fumigatus* up to the concentration of 30%, meanwhile it could not perform any antifungal activity below the concentration of 20%. This can be explained by the strong diffusion ability of the peppermint and lemongrass oils and their characteristics of volatility at room temperature. The essential oil vapour cannot escape out of the petri dish, therefore, it completely inhibited the fungi growth. When the concentration of essential oil vapour decreased, the amount of diffused essential oil in the petri dish was insufficient to inhibit the filamentous fungi. On the other hand, the betel leaf essential oil could perform antifungal activity to a dilution concentration as low as 10%. Interestingly, in this research, we determined that the betel leaf essential oil has potential to be applied to controlling both human pathogenic fungi *C. albicans* and *A. fumigatus*. The ability of antifungal activity of the essential oils depends on their chemical compositions [5]. Due to the difference in quantities and ingredients among the distinguished types of essential oils, their antifungal characteristics are not only affected by a specific mechanism but also by various ones [5]. The main mechanism is due to their hydrophobic features, where they can attack the cell membrane and disrupt it or affect the enzyme systems leading to respiratory depression and eventually cell death [10]. Peppermint, lemongrass, and betel leaf essential oils have been globally recognized to possess the ability of resistance to several types of micro-fungi [6, 8, 11]. This research claims that the mentioned

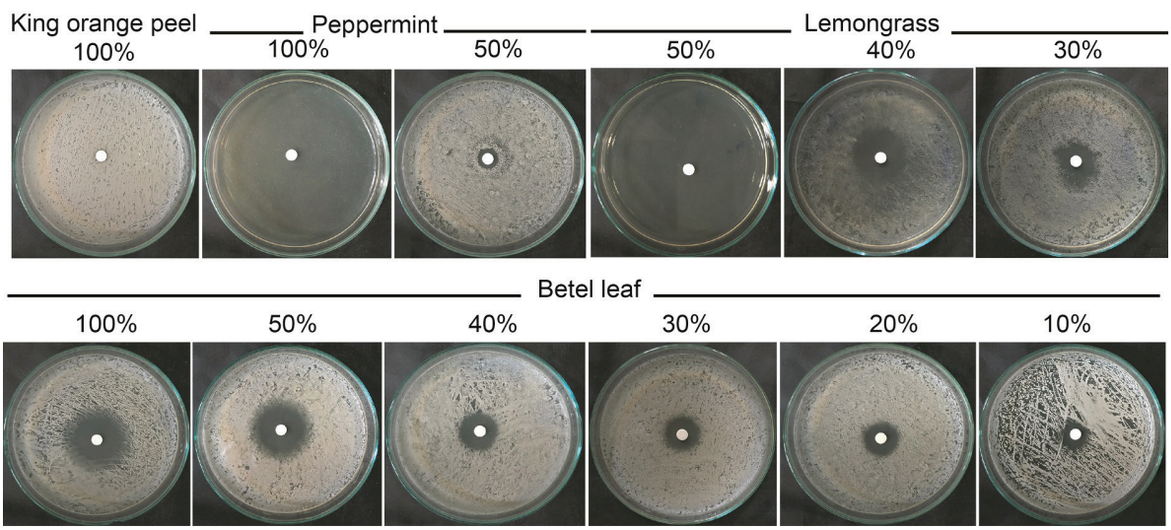

Fig. 1. Inhibition zones against *C. albicans* of some essential oils at different concentrations.

Table 2. Antifungal activities of several essential oils against *A. fumigatus*.

Essential oils	Inhibition zone (mm) at different concentration of essential oils (%)						
	100	*50*	*40*	*30*	*20*	*10*	*5*
King orange peel	-	-	-	-	-	-	-
Peppermint	No fungus growth	-	-	-	-	-	-
Lemongrass	No fungus growth	No fungus growth	No fungus growth	No fungus growth	-	-	-
Betel leaf	34.33±0.58	22.67±1.53	21.33±1.15	18.33±1.15	11.00±1.00	1.67±0.58	-

"-" no inhibition zone exhibited

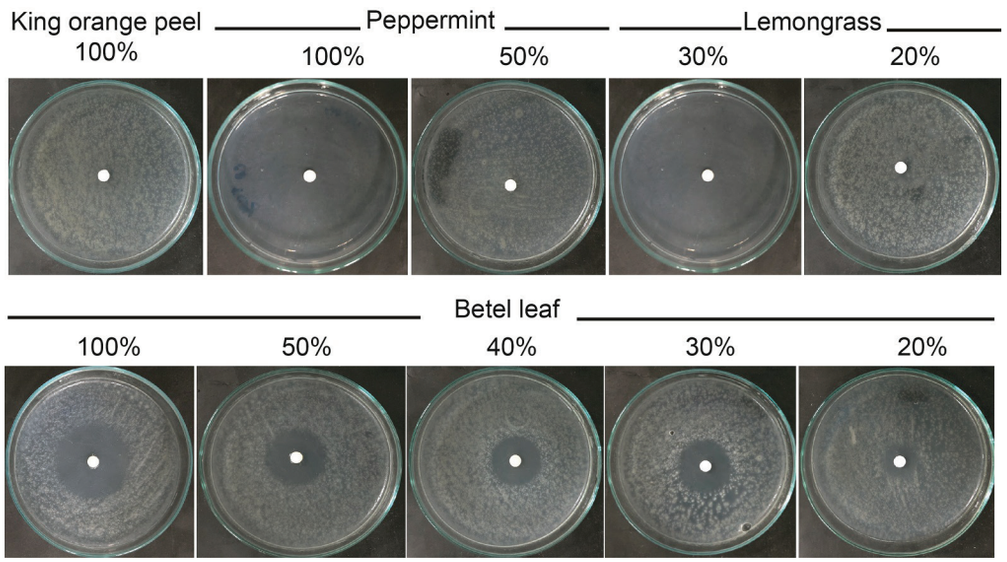

Fig. 2. Inhibition zones against *A. fumigatus* of some essential oils at different concentrations.

essential oils extracted from plants harvested in Vietnam also show strong antifungal activities and therefore have huge potential for being applied to the development of probiotics or medications for the diseases caused by the two fungi *C. albicans* and *A. fumigatus*.

While betel leaf essential oil could perform antifungal activity at a lower dilution concentration (10%), the lemongrass essential oil did not function below the dilution concentration of 20%. Thus, we believe that usage of betel leaf essential oil is a more economical and profitable material for the production of medical products. On the other hand, while the performance of lemongrass depends mostly on its dilution concentration, it showed a stronger inhibition towards fungus growth. Lemongrass essential oil could completely inhibit the growth of *C. albicans* at concentrations of 100% and 50% and completely inhibit the growth of *A. fumigatus* from the concentration of 30%, which was not exhibited by betel leaf essential oil. Therefore, betel leaf and lemongrass essential oils both possess certain advantages and disadvantages. As both are popular materials that can be easily grown and collected in Vietnam at low expense, we can consider their advantages and disadvantages in order to apply the appropriate type to mass industrial application.

Effects of betel leaf essential oil on the reproduction of the fungus C. albicans

In this research, the betel leaf essential oil was evaluated to have potential for controlling two human pathogenic fungi, *C. albicans* and *A. fumigatus*. Subsequently, we continued to evaluate the effects of the betel leaf essential oil on the reproduction of fungus *C. albicans*. The results showed the inhibition of the reproduction process in every medium containing the essential oil (Fig. 3). With the media containing the betel leaf essential oil at the concentration of 0.025-0.075%, the quantity of *C. albicans* cells after 2-6 h of cultivation did not demonstrate a significant change compared to the original quantity. Meanwhile, with the medium containing the betel leaf essential oil at a concentration of 0.1%, the quantity of fungi cells showed a tendency to gradually decrease. This could be due to the

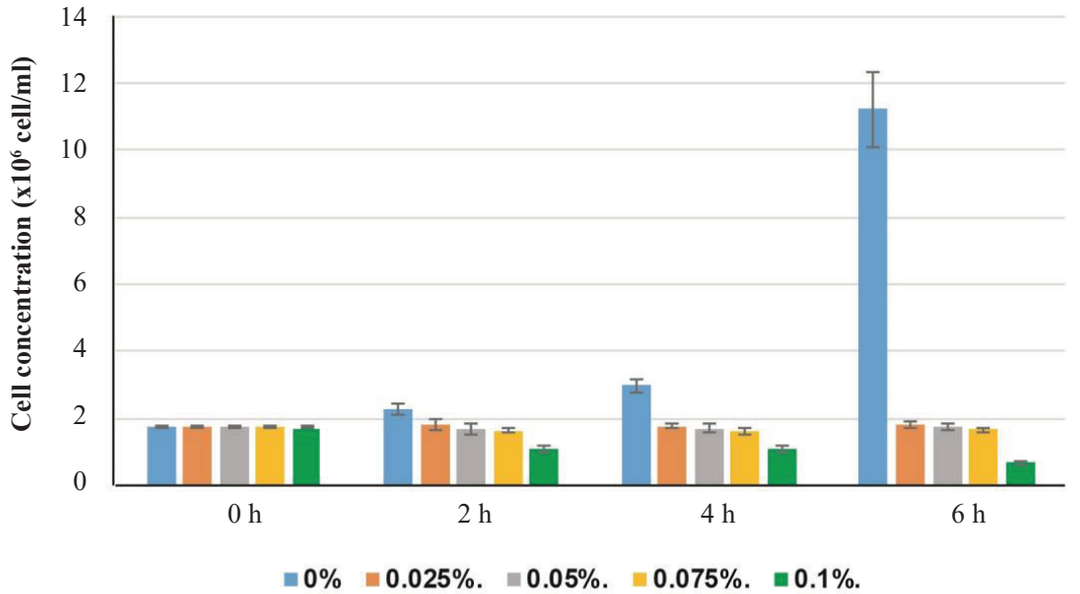

Fig. 3. Effects of betel leaf essential oil on the reproduction of *C. albicans.*

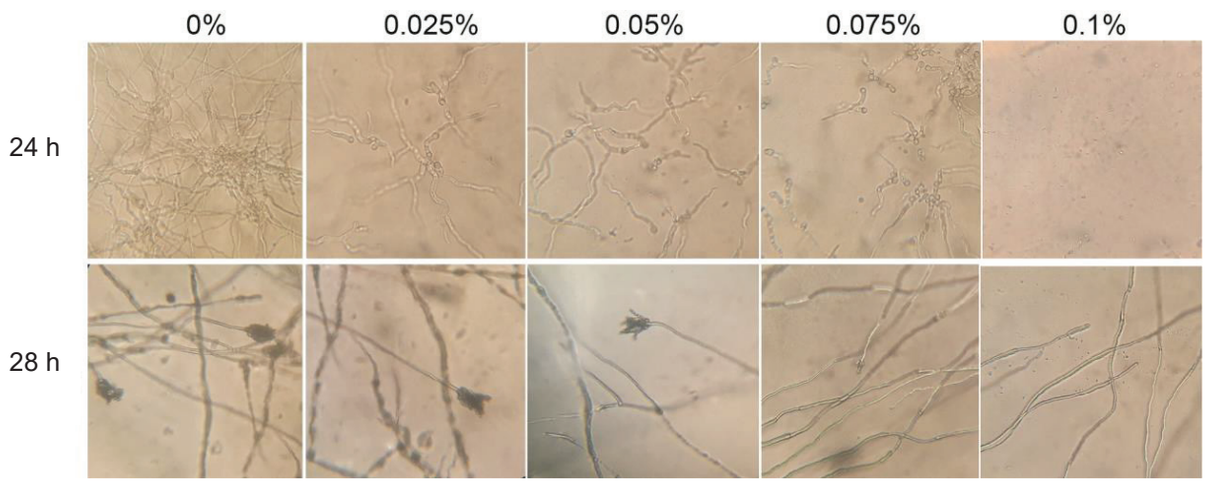

Fig. 4. Effects of betel leaf essential oil on the mycelium elongation of *A. fumigatus.*

start of fungal cell death by the betel leaf essential oil at a concentration of 0.1%, however, the process was dependent on the time. A previous study claimed that all parts of the betel plant showed strong antimicrobial activity by releasing their secondary metabolites [12]. Hydroxychavicol in the betel leaf was also proven to be resistant to the fungi *Candida* spp. by disrupting its cell membrane [13]. This research added a controlling role of the betel leaf essential oil on the fungus *Candida* through supressing its reproduction.

Effects of the betel leaf essential oil on the mycelium elongation of A. fumigatus

The betel leaf essential oil was proven to be resistant to several filamentous fungi of the genus *Aspergillus* such as *A. flavus*, *A. fumigatus*, *A. niger*, and *A. parasiticus* [13]. However, the majority of the research was only aimed at defining the minimum inhibitory concentration (MIC) [14]. A few other works mentioned that the betel leaf essential oil did not affect the cell wall of microorganisms [15]. This research was conducted to evaluate the effect of betel leaf essential oil on the mycelium elongation of *A. fumigatus*. The result showed that betel leaf essential oil inhibited the spore germination, mycelium elongation, and sporulation of *A. fumigatus* at every dilution concentration (Fig. 4). After 24 h of observation, the media containing betel leaf essential oil at concentrations of 0.025-0.1% delayed the process of spore germination and mycelium elongation. Especially in the medium containing betel essential oil at

the concentration of 0.1%, there was no spore germination even after 24 h. After 48 h of cultivation, in the media containing betel leaf essential oils at concentrations of 0.025% and 0.05%, there was a formation of conidiophores, however with a lower quantity compared to the medium not containing the essential oil. With the media containing essential oils at concentrations of 0.075% and 0.1%, there was recognition of the mycelium elongation but no formation of conidiophores. The inhibition of the spore germination, mycelium elongation, and sporulation of *A. fumigatus* could be recognized as a mechanism of controlling this pathogenic fungus by the betel leaf essential oil.

Conclusions

Peppermint, lemongrass, and betel leaf essential oils all showed antifungal activities towards *C. albicans* and *A. fumigatus*; especially betel leaf and lemongrass essential oils, which showed strong antifungal activities. Meanwhile, the King orange peel did not show any fungi resistance abilities.

The betel leaf essential oil was recognized to inhibit the reproduction of *C. albicans* and the spore germination, mycelium elongation, and sporulation of *A. fumigatus*.

ACKNOWLEDGEMENTS

We are grateful to Center of Experimental Biology, National Center for Technological Progress and Genomics Unit, The Key Laboratory of Enzyme and Protein Technology, University of Science, Vietnam National University, Hanoi for kindly providing the required microbial strains and essential oils. This work was funded by the National Center for Technological Progress, Ministry of Science and Technology.

The authors declare that there is no conflict of interest regarding the publication of this article.

REFERENCES

[1] P.L. Fidel (2002), "Immunity to *Candida*", *Oral Diseases*, **8**, pp.69-75.

[2] M. Mahmoudi Rad, A.S. Zafarghandi, M. Amel Zabihi, M. Tavallaee, Y. Mirdamadi (2012), "Identification of *Candida* species associated with vulvovaginal candidiasis by multiplex PCR", *Infectious Diseases in Obstetrics and Gynecology*, DOI: 10.1155/2012/872169.

[3] G.P. Bodey, S. Vartivarian (1989), "Aspergillosis", *European Journal of Clinical Microbiology and Infectious Diseases*, **8(5)**, pp.413-437.

[4] C. Paulussen, J.E. Hallsworth, S. Álvarez-Pérez, W.C. Nierman, P.G. Hamill, D. Blain, H. Rediers, B. Lievens (2017), "Ecology of aspergillosis: insights into the pathogenic potency of *Aspergillus fumigatus* and some other *Aspergillus* species", *Microbial Biotechnology*, **10(2)**, pp.296-322.

[5] S. Burt (2004), "Essential oils: their antibacterial properties and potential applications in foods a review", *International Journal of Food Microbiology*, **94(3)**, pp.223-253.

[6] X.T. Vu, T.T. Ngo, T.D.L. Mai, T.T. Bui, H.D. Le, T.V.H. Bui, Q.H. Nguyen, X.B. Ngo, V.T. Tran (2018), "A highly efficient *Agrobacterium tumefaciens*-mediated transformation system for the postharvest pathogen *Penicillium digitatum* using *DsRed* and *GFP* to visualize citrus host colonization", *Journal of Microbiological Methods*, **144**, pp.134-144.

[7] A.K. Tyagi, A. Malik (2010), "Liquid and vapour-phase antifungal activities of selected essential oils against *Candida albicans*: microscopic observations and chemical characterization of *Cymbopogon citratus*", *BMC Complementary and Alternative Medicine*, **10(1)**, pp.55-65.

[8] R. Kaypetch, S. Thaweboon (2018), "Antifungal property of *Piper betle* leaf oil against oral *Candida* species", *MATEC Web of Conferences*, DOI: 10.1051/matecconf/201824201021.

[9] J.L. Harris (1986), "Modified method for fungal slide culture", *Journal of Clinical Microbiology*, **24(3)**, pp.460-461.

[10] N. Noshirvani, B. Ghanbarzadeh, C. Gardrat, M.R. Rezaei, M. Hashemi, C. Le Coz, V. Coma (2017), "Cinnamon and ginger essential oils to improve antifungal, physical and mechanical properties of chitosan-carboxymethyl cellulose films", *Food Hydrocolloids*, **70**, pp.36-45.

[11] A.E. Edris, E.S. Farrag (2003), "Antifungal activity of peppermint and sweet basil essential oils and their major aroma constituents on some plant pathogenic fungi from the vapor phase", *Food/Nahrung*, **47(2)**, pp.117-121.

[12] B.S.L. Jenie, N. Andarwulan, N.L. Puspitasari-Nienaber, L. Nuraida (2001), "Antimicrobial activity of Piper betle linn extract towards foodborne pathogens and food spoilage microorganisms", *FT Annual Meeting*, New Orleans, Louisiana.

[13] I. Ali, F.G. Khan, K.A. Suri, B.D. Gupta, N.K. Satti, P. Dutt, F. Afrin, G.N. Qazi, I.A. Khan (2010), "In vitro antifungal activity of hydroxychavicol isolated from *Piper betle L.*", *Annals of Clinical Microbiology and Antimicrobials*, **9(1)**, pp.1-9.

[14] S. Pawar, V. Kalyankar, B. Dhamangaonkar, S. Dagade, S. Waghmode (2017), "Biochemical profiling of antifungal activity of betel leaf (*Piper betle L.*) extract and its significance in traditional medicine", *Journal of Advanced Research in Biotechnology*, **2**, pp.1-4.

[15] N. Singburaudom (2015), "Hydroxychavicol from Piper betel leave is an antifungal activity against plant pathogenic fungi", *Journal of Biopesticides*, **8(2)**, pp.82-92.

DOI: 10.31276/VJSTE.62(3).76-82

Optimization of the electrical signal generation of a microbial fuel cell for sensor applications

Duan Dong Ta[1], Linh Dam Thi Mai[2], Hai The Pham[1, 2*]

[1]GREENLAB - Center for Life Science Research (CELIFE), Faculty of Biology, University of Science, Vietnam National University, Hanoi

[2]Department of Microbiology, Faculty of Biology, University of Science, Vietnam National University, Hanoi

Received 20 September 2019; accepted 20 December 2019

Abstract:

In previous studies, a microbial fuel cell (MFC) was developed as a potential sensor that detects iron in water. However, to realize such an application in practice, the electrical signal generation of the MFC must be improved. Therefore, in this study, we investigated several measures to optimize the electrical signals of the MFC including (i) changing the anode spacing, (ii) testing different oxygen supply rates, (iii) testing different external resistances, and (iv) testing a new electrode material. An anode spacing of 2 cm was found to be optimal as the MFC generated a current that was at least 2-fold higher than any other anode spacing investigated. To limit oxygen diffusion from the cathode to the anode, an optimal cathode air flow rate of 1.8 ml min^{-1} was found, which corresponds to an oxygen supply rate of 0.286 mg min^{-1}. By a polarization experiment, a 60-Ω external resistance ensured the most stable MFC-generated current , which is compulsory for the use of the device as a biosensor. Finally, activated carbon was shown to be an excellent material to improve electrical signal generation by 2-fold in comparison with graphite felt and graphite granules. These reported results will be the basis of further development of the MFC toward a practical biosensor.

Keywords: **anode spacing, electrode material, external resistance, microbial fuel cell biosensor, oxygen supply rate.**

Classification number: **3.5**

Introduction

Microbial fuel cells (MFCs) are bioelectrochemical systems that generate electricity throughthe electrochemical activity of microorganisms that harvest electrons by oxidizing substrates at the anode [1]. Due to this unique property, MFCs offer a variety of potential applications. These include the use of MFCs as sensors to analyse or monitor pollutants such as organic content or metals [2-5]. Particularly, Nguyen, et al. (2015) [4] successfully developed an MFC that can be potentially applied to detect iron and manganese in water samples. Reusability, long lifetime, and simple handling are some advantages of an MFC system [6]. However, to realize such a potential application in practice, the stability and sensitivity of the electrical signal generated by the MFC need to be improved [6]. In order to achieve this objective, the following factors influencing the performance of MFCs should be addressed [7, 8].

The performance of MFCs can be affected by operational parameters such as temperature, pH, dissolved oxygen concentration, and electrolyte (or buffer) strength [7, 9]. The power generation of MFCs may not reach their theoretical maximumdue to ohmic, activation, and concentration losses that cause overpotentials. Some proposed approaches to reduce these losses include (i) optimization of the reactor configuration, such as adjusting the electrode spacing, (ii) use of a highly proton-selective membrane, (iii) increasing the electrode surface area, and/or (iv) improving the activity of the catalysts at both electrodes [10]. Therefore, to improve the performance of the previously-developed MFC for sensor applications [4], in this study we attempt to (i) discover a better performing electrode material to

*Corresponding author: Email: phamthehai@vnu.edu.vn

minimize the internal resistance of the MFC, (ii) modify the anodic electrode spacing to determine a design that better supports the electrochemical activity of acting bacteria, and (iii) reduce losses during the electron transfer process (from the electron donor at the anode to the electron acceptor at the cathode) via optimization of the cathode oxygen supply rate and the external resistance using polarization analysis.

Materials and methods

Reactor setup

The MFC reactors used in this study were fabricated based on the design of the lithotrophic iron-oxidizing MFC (LIO-MFC) previously developed in [4]. In brief, each reactor consisted of two large poly-acrylic frames (12 cm×12 cm×2 cm) and two small poly-acrylic rectangle-holed subframes of anode and cathode compartments (8 cm×8 cm×X cm), with X being 1.5 cm unless specified as the spacing value to be tested in the respective experiment. Each rectangle hole on each subframe had the dimension of 5 cm×5 cm and thus the dimension of each compartment was 5 cm×5 cm×X cm. Graphite granules (3-5 mm in diameter) were used as the default electrode material and thus loaded into each compartment until it was filled. These were replaced with activated carbon granules in an experiment specified below. These granules were loaded in a manner to ensure that they were packed well enough to ensure good contact with each other and with the graphite rod (5 mm in diameter) to collect the electrical current [4]. Epoxy glue was used to seal the gaps between the rod and the frame to ensure that the compartment was completely closed. Also, for this purpose, rubber gaskets were sandwiched between the poly-acrylic parts during reactor assembly. Two compartments of each reactor were separated by a 6 cm×6 cm Nafion 117 membrane (Du Pont, USA). The rest of the reactor assembly process was the same as described in [4]. A default external resistance of 10 Ω was used unless otherwise stated in an experiment.

The anolyte or the catholyte was conveyed in and out of their respective chambers in each reactor through PVC pipes sealed to 2 holes (5 mm in diameter) that were created on the large frame of each compartment. The sterilized modified M9 medium (0.44 g KH_2PO_4 l^{-1}, 0.34 g K_2HPO_4 l^{-1}, 0.5 g NaCl l^{-1}, 0.2 g $MgSO_4.7H_2O$ l^{-1}, 0.0146 g $CaCl_2$ l^{-1}, pH 7) was contained in a medium bottle and was passed through a drip chamber before being supplied to the anode chamber via the anode influent pipe inserted with a three-way connector [11].

Operation of the MFCs [4]

After assembly, the MFC reactors were operated as in previous studies [4, 12]. Specifically, in batch mode, at room temperature (25±3°C), with $FeCl_2$ as the source of ferrous ions mixed in the modified M9 medium through the three-way connector on the anode influent pipe. The modified M9 medium was purged with nitrogen (Messer, Vietnam) for 30-60 minbefore being supplied to the anode to minimize the amount of oxygen, which may compete with the anode to accept electrons. The final concentration of Fe^{2+} in the anolyte was achieved by a careful calculation of the volume and the concentration of the supplied $FeCl_2$ solution. In each batch, half of the anolyte (approx. 10 ml) was replaced. A $NaHCO_3$ solution was also supplied as the carbon source for the anode microorganisms such that its final concentration in the anolyte was 2 g l^{-1} [11]. At the cathode of each MFC reactor, only a buffer solution without any catalyst (0.44 g KH_2PO_4 l^{-1}, 0.34 g K_2HPO_4 l^{-1}, 0.5 g NaCl l^{-1}) was supplied. Any remaining catholyte was completely replaced with freshly-made catholyteat the beginning of each batch. The cathode compartment was aerated through the cathode influent pipe with an air pump (model SL-2800, Silver Lake, China) to provide the final electron acceptor, which is oxygen. The pump was manipulated so that the rate of aeration was slightly above 50 ml min^{-1} to ensure that the cathode solution was air-saturated [13] but did not evaporate quickly. In this study, the manner of oxygen supply was altered in some experiments, which is described later.

A batch run was startedwhen the anolyte was replaced, and the run was finished when the current dropped down to its baseline. Thus,such a batch usually lasted for 2 h. In experiments, an interval of 1 h was allowed in between every 2 consecutive batches. The MFC reactors were left on standby during the night. The operational scheme described above did not affect theperformance stability of the MFC reactors.

Enrichment of iron oxidizing bacteria in the MFCs

For the enrichment of iron-oxidizing bacteria in the MFCs, two different microbial sources were used for inoculation: (i) well water samples, with a fawn colour typical for water contaminated with iron, taken from Hoai Duc and Hoang Mai (Hanoi, Vietnam) and (ii) soil and mud samples at a depth of 10 cm from the Trai Cau iron mine, Dong Hy (Thai Nguyen province, Vietnam). The two sources were mixed at a ratio of 1:1 to create an inoculum for the enrichment. The

enrichment process was the same as in previous studies [4, 12], with 20 mM being the concentration of Fe^{2+} supplied into the anode during the enrichment.

Testing activated carbon granules as a novel electrode material

Activated carbon granules (COCO AC Ltd., Vietnam) about 3-5 mm in diameter were tested as the electrode material in an MFC at both the anode and the cathode. Graphite granules were used in another MFC as the control. The graphite and activated carbon granules were washed several times with distilled water to remove impurities and were left to drain. After that, the granules were loaded into the electrode chambers of the MFCs. The installation of the MFCs with the granules was performed in the same way as described in the previous studies [4, 12]. At the same time, the MFCs in the experiment were enriched with electroactive bacteria from the same microbial sources. After the enrichment, the performance of the MFCs, in terms of electricity generation, were investigated and compared by using the methods described below.

Testing different cathode oxygen supply rates

This experiment was conducted to investigate and optimize the rate of oxygen supply to the cathode of the LIO-MFCs. In this experiment, instead of pumping air directly into the cathode compartment, we purged the catholyte separately with air in a flask at full speed by an air pump before supplying the aerated catholyte into the cathode compartment. In the same manner, the rate of oxygen supply to the cathode was adjusted with a speed control valve inserted into the cathode influent pipe that conveyed the catholyte from the flask to the cathode compartment. Two MFCs were operated with cathode flow rates ranging from the lowest speed of *ca.* 0.12 ml min^{-1} to a speed as high as 30 ml min^{-1}. Considering that the aerated catholyte in the separate flask was air-saturated, the oxygen supply rate corresponding to each flow rate can be calculated. During the experiment, the MFCs were fed with 5 mM of Fe^{2+} at the anode.

Testing varied external resistances and polarization analysis

In this experiment, we attempted to establish the polarization curve of the LIO-MFC by changing its external resistance and measuring the corresponding voltage and current. The external resistance values ranging from 5000 Ω to 10 Ω were tested accordingly. Throughout the test, the appropriate and adequate time for the current to stabilize at each resistance level was about 5 min. Thus, the MFC was operated with each resistance for about 5 min and then corresponding voltage and current were recorded. The average voltage of 5 measurements in 5 min was calculated and used for the calculation of other parameters such as current density, power density, etc.

Testing different anode spacings

To investigate the effect of the anode spacing on the performance of the MFCs, different thicknesses of the anode chamber were tested, including 1.5 cm (the default thickness used in the previous studies), 2 cm, and 2.5 cm. Three MFCs with anode spacings of 1.5 cm, 2 cm, and 2.5 cm were assembled and inoculated with the microbial sources for the enrichment of electroactive bacteria, as mentioned above, before their electricity generation performances were evaluated and compared.

Measurement and calculation of electrical parameters

A data acquisition system coupled with a multimeter (Keithley model 2700, Keithley Inc., USA) was used to automatically record the voltage between the anode and the cathode of each MFC. The recording interval was 1 min or 10 min depending on each experiment. The measurement and calculation of the following electrical parameters:current I (A), voltage U (V), power P (W), and resistance R (Ω) were carried out according to Logan, et al. (2006) [1] and Aelterman, et al. (2006) [14]. Unless otherwise stated, all the experiments in this study were repeated at least 3 times before the data were collected and analysed.

Results

Activated carbon - an electrode material suitable for sensors based on MFCs

Replacing the electrode material with activated carbon granules strikingly improved the generation of electrical current. The assembled LIO-MFC that was setup and operated with activated carbon granules produced a stable current of ca. 0.65 mA, which is more than 3-fold higher than that of the control with graphite granules (see Fig. 1). The increased current by the former was not intermittent but steady (Fig. 1). Polarization analyses also showed that the LIO-MFC with activated carbon granules produced about a 2-fold higher power density and a 4-fold higher current density compared to the control (see Fig. 2).

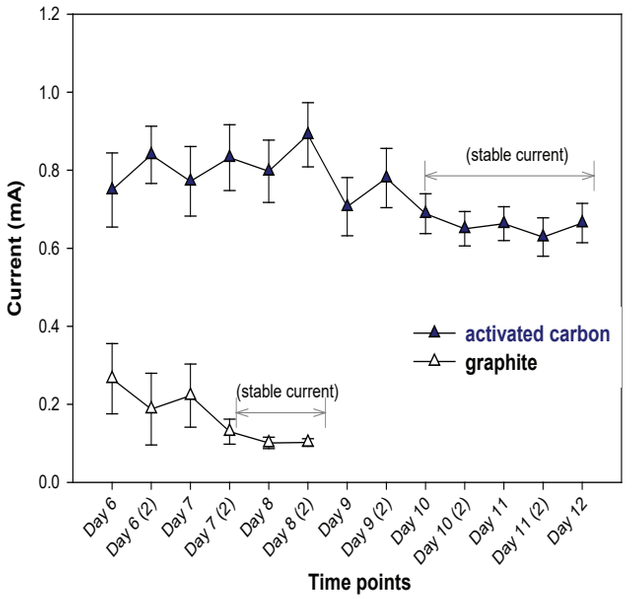

Fig. 1. Comparison of the electricity generation by the LIO-MFC operated with activated carbon granules as the electrode material (MFC 9) and the control operated with graphite granules as the electrode material (MFC 8). Both MFCs had an anode spacing of 1.5 cm and were operated at room temperature with an external resistance of 10 Ω and with directly-aerated cathodes.

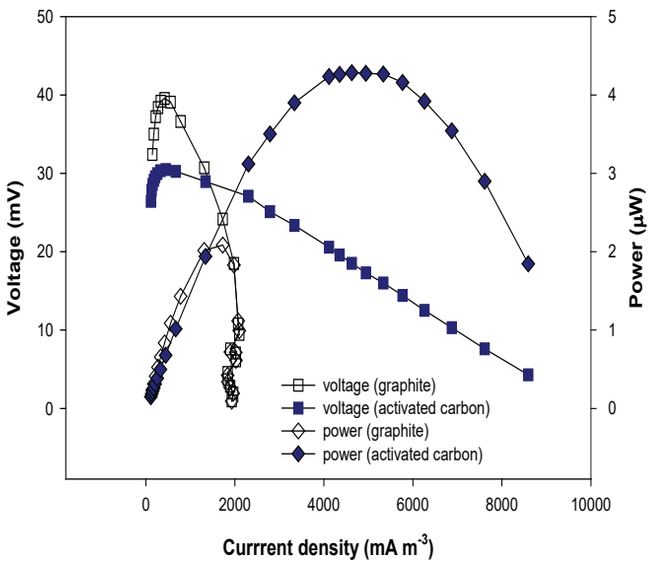

Fig. 2. The polarization curves performed on an MFC operated with activated carbon granules as the electrode material (filled symbols) and an MFC operated with graphite granules as the electrode material (unfilled symbols). Both MFCs had an anode spacing of 1.5 cm, and were operated at room temperature with an external resistance of 10 Ω, and with directly-aerated cathodes.

Activated carbon has been reported to have a larger surface area (thus larger contact area) and a higher catalytic activity for oxygen reduction when compared to graphite [15]. Increased surface area might reduce activation loss and diffusion loss and improve electron transfer [16]. It was reported that the catalytic activity for the oxygen reduction of activated carbon is over 3-fold higher than that of plain carbon (even better than that of graphite) and comparable to that of platinum [17]. Therefore, it is understandable that using activated carbon granules as the electrode material could improve the generation of electrical signals of our MFCs (the LIO-MFCs). Furthermore, our results indicate that this improvement can be stable in a long term. This point is also supported by Zhang, et al. (2011) [18], who reported that the material could stably perform for up to 1 year.

Determination of an appropriate oxygen supply scheme at the cathode of the MFCs to limit oxygen diffusion to the anode

Studies have shown that when oxygen is excessively supplied to the cathode, additional oxygen diffusion from the cathode to the anode can occur, which reduces electricity generation [9, 19]. It has also been reported that oxygen diffusion from the cathode chamber to the anode chamber can greatly affect the electron transfer and microbial community of the anode, therefore reducingthe generation of electricity [8, 20]. Therefore, our hypothesis is that our default mode of cathode aeration (as described above, at a rate of 200 l air h^{-1}) could lead to a rate of oxygen supply to the cathode that is too high, resulting in excessive dissolved oxygen levels and critical oxygen diffusion. Thus, we propose that the generation of electrical currents by the LIO-MFCs can be improved by a proper oxygen supply scheme at the cathode.

Therefore, various oxygen supply rates at the cathode were carefully tested by varying the air-saturated catholyte rates supplied to the cathode from 0.12 ml min^{-1} to 30 ml min^{-1}. Interestingly, the results (see Fig. 3) showed that the currents generated by the 2 MFCs in the experiment increased when the catholyte supply rate increased from 0.12 ml min^{-1} to 1.8 ml min^{-1} and clearly decreased when the catholyte supply rate was higher than 1.8 ml min^{-1}. At a catholyte flow rate of 1.8 ml min^{-1}, the currents generated by the 2 MFCs (MFC 6 and MFC 7) were 0.062 mA and 0.051 mA, respectively, which is almost double the currents generated at rates in the range of 11-30 ml min^{-1} (i.e.

excessive oxygen supply). This scheme of oxygen supply is much less intensive than our default direct aeration mode, even at high catholyte flow rates. From this we deduce that direct aeration mode is far from optimum and causes too much oxygen diffusion, as proposed in our hypothesis.

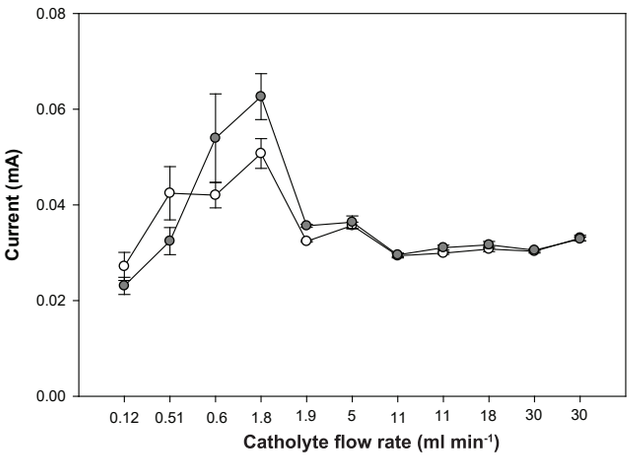

Fig. 3. The relationship between the air-saturated catholyte flow rate and the current generated by the LIO-MFC. Two MFCs were used as replicates. The MFCs both have an anode spacing of 1.5 cm, were operated at room temperature with graphite granules as the electrode material, and with an external resistance of 10 ohm.

As mentioned above, cathode-to-anode oxygen diffusion was discovered a long time ago, but to our knowledge no study has been conducted to determine a proper oxygen supply at the cathode to limit that diffusion and its consequence. In this study, we report for the first time, an optimal oxygen supply rate to the cathode, which is 1.8 ml air-saturated catholyte min^{-1} equal to 0.286 mg O_2 min^{-1}. Knowing this value will not only support the operation of MFCs in a way that minimizes the oxygen diffusion, but also help save energy for cathode aeration.

Determination of an optimal external resistance for a high and stable generation of the LIO-MFC

A polarization curve of a LIO-MFC operated with activated carbon granules as the electrode material was established by varying the external resistance in order to determine the condition at which the power density is maximum. The polarization curve (Fig. 2) showed that the power density of the MFC reached its maximum when the current density was in the range of 4200-4700 mA m^{-3}. Under these conditions, the external resistance was about 60-100 Ω (Fig. 4). In this range, the current is proportional to the voltage (Fig. 4), which indicates a stable performance of the system.

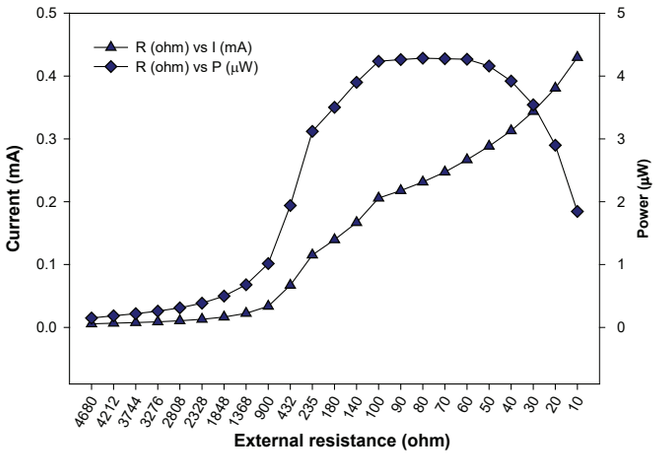

Fig. 4. The electricity generation of the LIO-MFC operated with activated carbon granules in response to changes in the external resistance.

The effect of external resistance on the performance of MFCs, in general, has been reported by a number of publications [9, 21] and the need to determine an optimal external resistance is evident [22]. It is believed that a proper match between the external resistance and internal resistance is required for a good performance of an MFC [22, 23]. While an external resistance of less than 500 Ω was suggested for use in certain types of BOD-sensing MFCs [9], a much lower external resistance (10.5 Ω) was suggested to improve and stabilize the performance of some other systems [24]. It is therefore plausible that there is a specific optimal external resistance for each individual system. In our study, an external resistance between 60 and 100 Ω appears to enable an optimal generation of electricity by the LIO-MFC.

Effect of anode spacing on the generation of electrical signals by the LIO-MFCs

As described above, 3 MFCs with different anode spacings (1.5 cm, 2 cm and 2.5 cm) were assembled and inoculated with the microbial sources for the enrichment of electroactive bacteria. The 3 MFCs began to generate electrical currents right after the first day of enrichment when operated with 20 mM Fe^{2+} at the anode. The currents gradually became stable 3 to 5 d after the inoculation. The average daily currents of the 3 MFCs were significantly different ($p<0.05$, Fig. 5). Among the 3 MFCs, the one operated with an anode spacing of 2 cm (MFC 7) showed the best performance with a generated current of around 0.3 mA. The current generated by the MFC operated with an anode spacing of 2.5 cm (MFC 6) was only around 0.25 mA and that of the MFC with 1.5 cm anode spacing (MFC 1)

was even lower at 0.15 mA. The results show that the anode spacing greatly affects the electrochemical processes inside the MFCs.

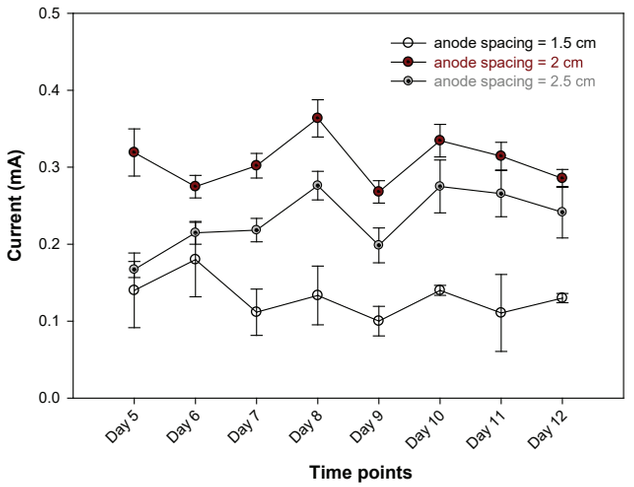

Fig. 5. The differences in electrical signals generated by 3 MFCs with different anode spacings: 1.5 cm (MFC 1) (the control), 2.0 cm (MFC 7), and 2.5 cm (MFC 6). The MFCs were all operated at room temperature with graphite granules as the electrode material, with an external resistance of 10 Ω, and with directly-aerated cathodes.

The currents of the 3 MFCs followed similar trends in time while the MFCs were operated under the same conditions, which indicates that the differences in the electrical current level are due to the differences in their anode spacings. It is interesting to note that increasing the anode spacing from 1.5 cm to 2 cm could significantly boost the current, but increasing 0.5 cm further led to a reduced current. The latter is the reason why we did not test further increased anode spacings. An increased anode volume may permit increased substrate supply and an increased surface area for the anode reaction, but this does not always mean that a larger anode volume generates a higher electrical current. Furthermore, a shorter electrode spacing is believed to reduce the internal resistance, resulting in better electron transfer and thus a higher power output [24, 25]. However, reducing the anode spacing to a certain level could lead to reduced electricity generation, possibly due to oxygen intrusion from the cathode to the anode [25]. Thus, it is always necessary to determine an optimal anode spacing for any MFC system. In our case, the anode spacing of 2 cm appears to be close to optimum. Our results also demonstrate that the current generated by the MFC with 2 cm anode spacing was more stable, which is a beneficial property for an MFC-based sensor.

Conclusions

In this study, several measures to improve the generation of electrical signals by a potential lithotrophic MFC-based sensor were found by combining the advantages of MFC performance optimization from previous studies. These include (i) increasing the anode spacing to an optimal value of 2 cm, (ii) replacing the electrode material with activated carbon granules, (iii) operating the MFC with an oxygen supply rate of 0.286 mg O_2 min^{-1} at the cathode, and (iv) operating the MFC with an external resistance in the range of 60-100 Ω. Upon those findings, further studies are required to realize the application potential of the improved system as a biosensor for environmental monitoring in practice.

ACKNOWLEDGEMENTS

This research received financial support from International Foundation for Science (IFS - Sweden) (grant No. W/5186-2) and from Korea Institute of Science and Technology (KIST) IRDA Alumni Program.

The authors declare that there is no conflict of interest regarding the publication of this article.

REFERENCES

[1] B.E. Logan, B. Hamelers, R. Rozendal, U. Schrorder, J. Keller, S. Freguia, P. Aelterman, W. Verstraete, K. Rabaey (2006), "Microbial fuel cells: methodology and technology", *Environmental Science & Technology*, **40(17)**, pp.5181-5192.

[2] M. Kim, S.M. Youn, S.H. Shin, J.G. Jang, S.H. Han, M.S. Hyun, G.M. Gadd, H.J. Kim (2003), "Practical field application of a novel BOD monitoring system", *Journal of Environmental Monitoring*, **4(2003)**, pp.640-643.

[3] M.C. Hsieh, Y.C. Chung (2014), "Measurement of biochemical oxygen demand from different wastewater samples using a mediator-less microbial fuel cell biosensor", *Environ. Technol*. **35(17)**, pp.2204-2211.

[4] T.T. Nguyen, T.T.T. Luong, P.H.N. Tran, H.T.V. Bui, H.Q. Nguyen, H.T. Dinh, B.H. Kim, H.T. Pham (2015), "A lithotrophic microbial fuel cell operated with pseudomonads-dominated iron-oxidizing bacteria enriched at the anode", *Microbial Biotechnology*, **8**, pp.579-589.

[5] M. Di Lorenzo, A.R. Thomson, K. Schneider, P.J. Cameron, I. Ieropoulos (2014), "A small-scale air-cathode microbial fuel cell for on-line monitoring of water quality", *Biosens. Bioelectron*., **62**, pp.182-188.

[6] H.T. Pham (2018), "Biosensors based on lithotrophic microbial fuel cells in relation to heterotrophic counterparts: research progress, challenges, and opportunities", *AIMS Microbiology*, **4(3)**, pp.567-583.

[7] M.-C. Hsieh, C.-Y. Cheng, M.-H. Liu, Y.-C. Chung (2016), "Effects of operating parameters on measurements of biochemical oxygen demand using a mediatorlessmicrobial fuel cell biosensor", *Sensors (Basel, Switzerland)*, **16(1)**, pp.35.

[8] B.H. Kim, I.S. Chang, G.M. Gadd (2007), "Challenges in microbial fuel cell development and operation", *Applied Microbiology and Biotechnology*, **76**, pp.485-494.

[9] G.-C. Gil, C. In-Seop, K. Byung Hong, K. Mia, J. Jae-Kyung, P. Hyung Soo, K. Hyung Joo (2003), "Operational parameters affecting the performance of a mediator-less microbial fuel cell", *Biosensors & Bioelectronics*, **18(4)**, pp.327-334.

[10] A.J. Bard, L.R. Faulkner (2000), *Electrochemical Methods: Fundamentals and Applications*, 2nd Edition, John Wiley & Sons, New York, 864pp.

[11] P. Clauwaert, K. Rabaey, P. Aelterman, L. De Schamphelaire, T.H. Ham, P. Boeckx, N. Boon, W. Verstraete (2007), "Biological denitrification in microbial fuel cells", *Environmental Science & Technology*, **41(9)**, pp.3354-3360.

[12] P.H. Nguyen Tran, T.T. Thi Luong, T.T. Thi Nguyen, H.Q. Nguyen, H.V. Duong, B.H. Kim, H.T. Pham (2015), "Possibility of using a lithotrophic iron-oxidizing microbial fuel cell as a biosensor for detecting iron and manganese in water samples", *Environmental Science: Processes & Impacts*, **10(2015)**, pp.1806-1815.

[13] T.H. Pham, J.K. Jang, H.S. Moon, I.S. Chang, B.H. Kim (2005), "Improved performance of microbial fuel cell using membrane-electrode assembly", *Journal of Microbiology and Biotechnology*, **15(2)**, pp.438-441.

[14] P. Aelterman, K. Rabaey, H.T. Pham, N. Boon, W. Verstraete (2006), "Continuous electricity generation at high voltages and currents using stacked microbial fuel cells", *Environmental Science & Technology*, **40**, pp.3388-3394.

[15] F. Zhang, S. Cheng, D. Pant, G.V. Bogaert, B.E. Logan (2009), "Power generation using an activated carbon and metal mesh cathode in a microbial fuel cell", *Electrochemistry Communications*, **11(11)**, pp.2177-2179.

[16] H. Tursun, R. Liu, J. Li, R. Abro, X. Wang, Y. Gao, Y. Li (2016), "Carbon material optimized biocathode for improving microbial fuel cell performance", *Frontiers in Microbiology*, **7**, pp.1-9.

[17] M. Ghasemi, S. Shahgaldi, M. Ismail, B.H. Kim, Z. Yaakob, W.R. Wan Daud (2011), "Activated carbon nanofibers as an alternative cathode catalyst to platinum in a two-chamber microbial fuel cell", *International Journal of Hydrogen Energy*, **36(21)**, pp.13746-13752.

[18] F. Zhang, D. Pant, B.E. Logan (2011), "Long-term performance of activated carbon air cathodes with different diffusion layer porosities in microbial fuel cells", *Biosensors and Bioelectronics*, **30(1)**, pp.49-55.

[19] T.H. Pham, J.K. Jang, I.S. Chang, B.H. Kim (2004), "Improvement of cathode reaction of a mediatorless microbial fuel cell", *Journal of Microbiology and Biotechnology*, **14(2)**, pp.324-329.

[20] S.-E. Oh, J.R. Kim, J.H. Joo, B. Logan (2009), "Effects of applied voltages and dissolved oxygen on sustained power generation by microbial fuel cells", *Water Science & Technology*, **60(5)**, pp.1311-1317.

[21] J.K. Jang, T.H. Pham, I.S. Chang, K.H. Kang, H. Moon, K.S. Cho, B.H. Kim (2004), "Construction and operation of a novel mediator- and membrane-less microbial fuel cell", *Process Biochemistry*, **39(8)**, pp.1007-1012.

[22] R.P. Pinto, B. Srinivasan, S.R. Guiot, B. Tartakovsky (2011), "The effect of real-time external resistance optimization on microbial fuel cell performance", *Water Research*, **45(4)**, pp.1571-1578.

[23] P. Aelterman, M. Versichele, M. Marzorati, N. Boon, W. Verstraete (2008), "Loading rate and external resistance control the electricity generation of microbial fuel cells with different three-dimensional anodes", *Bioresource Technology*, **99(18)**, pp.8895-8902.

[24] Y. Park, V.K. Nguyen, S. Park, J. Yu, T. Lee (2018), "Effects of anode spacing and flow rate on energy recovery of flat-panel air-cathode microbial fuel cells using domestic wastewater", *Bioresource Technology*, **258**, pp.57-63.

[25] S. Cheng, H. Liu, B.E. Logan (2006), "Increased power generation in a continuous flow MFC with advective flow through the porous anode and reduced electrode spacing", *Environmental Science & Technology*, **40**, pp.2426-2432.

DOI: 10.31276/VJSTE.62(3).83-89

Preliminary assessment on the microplastic contamination in the atmospheric fallout in the Phuoc Hiep landfill, Cu Chi, Ho Chi Minh city

Thuong Quoc Thinh[1], Truong Tran Nguyen Sang [1, 2], Tran Quoc Viet[1, 2], Le Thi Minh Tam[2], Nguyen Phuoc Dan[2], Emilie Strady[2, 3, 4], Kieu Le Thuy Chung[5*]

[1]Faculty of Environment and Natural Resources, University of Technology, Vietnam National University, Ho Chi Minh city, Vietnam
[2]CARE (Asian Center for Water Research), University of Technology, Vietnam National University, Ho Chi Minh city, Vietnam
[3]Univ. Grenoble Alpes, CNRS, IRD, Grenoble, France
[4]Aix-Marseille Univ., Mediterranean Institute of Oceanography (MIO), Marseille, Université de Toulon, CNRS /IRD, France
[5]Faculty of Geology and Petroleum Engineering, University of Technology, Vietnam National University, Ho Chi Minh city, Vietnam

Received 16 September 2019; accepted 25 November 2019

Abstract:

Microplastic pollution has become a global issue in recent years. Since the early 2000s, scientists have investigated the occurrence of microplastics (MiPs) in the environment. While research on marine MiPs is more advanced at present, there are immense gaps of knowledge regarding continental MiPs. Airborne MiPs are one source of MiPs in the aquatic environment. In the scientific literature, there have been only three publications on presence of MiPs in atmospheric fallout. In developing countries, where plastic waste management is weak, studies on the presence of MiPs in this area are limited. This current study presents a preliminary assessment of the presence of MiPs in atmospheric fallout sampled from the Phuoc Hiep landfill, Ho Chi Minh city (HCMC). The results of this work show that MiP concentrations vary between 1,801 items $m^{-2}d^{-1}$ and 913 items $m^{-2}d^{-1}$ in the dry and rainy seasons, respectively.

Keywords: **atmospheric fallout, microplastics, Phuoc Hiep landfill.**

Classification number: **5.1**

Introduction

Nowadays, plastic pollution is an emerging concern worldwide. Global plastic production increases annually by approximately 3% and reached 335 million tons in 2017 [1], which has led to a dramatic change of the type of solid wastes discharged into the environment. Especially in developing countries, where plastic wastes are often mismanaged or abandoned in illegal dumping sites, plastic pollution is significantly contributing to environmental pollution [2]. As a result, plastic particles can be transferred to aquatic environments. Many studies have shown that plastics are found from continental aquatic system such as lakes, canals, and rivers to the oceans along the coastal zones, seabed sediments, beach sands, floating on the water's surface and even in frozen ice in the Arctic and Antarctic regions [3].

The existence of plastic waste in the aquatic system poses challenges to the world's environment. The 2030 Agenda for Sustainable Development and its Sustainable Development Goals dedicated several necessary goals that are relevant to this issue (e.g. SDG 11, SDG 12, SDG 14), especially Target 14.1 which states: "By 2025, prevent and significantly reduce marine pollution of all kinds, in particular from land-based activities, including marine debris and nutrient pollution". More seriously, under impacts from many factors such as mechanical processes, oxidation, and biodegradation, microplastics (MiPs), i.e. plastic particles comprised between 1 μm and 5 mm in

*Corresponding author: Email: kltchung@hcmut.edu.vn

size [4] are formed and can last thousands of years in the environment due to their chemical stability and durability [5]. MiPs are considered as a new pollutant that is of great concern by the world due to its deleterious effects on the survival and reproduction of aquatic organisms [6] through ingestion and accumulation [7] as well as its effect on human health through seafood, salt ingestion, and inhalation of airborne MiPs [8].

Recent years, global studies have shown the distribution of MiPs and their harmful effects on marine environments such as seas [9-11], freshwater lakes [12, 13], rivers [14, 15], and terrestrial environments in Vietnam. Authors also reported that the concentrations of MiPs in the water of HCMC's canals and the Saigon river varied from 270 to 518×10^3 fibres m^{-3} and from 7 to 223 fragments m^{-3} [16].

While the presence of MiPs in the marine environment is widely documented, their sources, dynamics, and fate in rivers and estuaries remain poorly understood and largely undocumented [17, 18]. Among the sources of MiPs, urban inputs such as wastewater treatment plant effluents are increasingly studied while the atmospheric compartment is mostly neglected, though the fact that the presence of MiPs in atmospheric fallout has become an environmental and social challenge due to their ability to spread toxic additives, organic, and inorganic contaminants that adhere to the MiPs' surface, the aquatic environment, or even directly to the human body during inhalation [17]. So far, there have only been three publications on MiPs in atmospheric fallout in Donguan (China), Paris, and a remote area called French Pyrenees (France), which all show that there was a significant concentration of MiPs in the atmosphere in those areas [19-21].

HCMC, the economic capital of Vietnam and one of the most dynamic developing cities from South East Asia, was chosen to study MiPs in atmospheric fallout. This study aimed to determine the occurrence of MiPs in atmospheric fallouts at Phuoc Hiep landfill, during the dry and rainy seasons, and point out the physical characteristics of suspected items.

Materials and methods

Sampling

Sample collection was conducted during both dry and rainy seasons at the Phuoc Hiep landfill (10°57'53.8"N 106°26'18.7"E) located in the northwest of HCMC and operated by the HCMC Urban Environment Company Limited (Citenco) (Fig. 1). The designed disposal volume of this landfill is around 4.4 million tons. There were 8 samples collected during the dry season (December 2018 and January 2019) and the rainy season (May and June 2019) with a sampling duration of 3 or 4 days for each sample (Table 1).

Fig. 1. Sampling location.

The design of the sampling device employed in this research was based on a previous study [19], which consisted of a 250 mm diameter glass funnel placed on a 10-litre glass bottle to collect rainwater and air dust falling into the funnel area and into the bottle. The sampling device was placed at a height of 3 m above ground (Fig. 2).

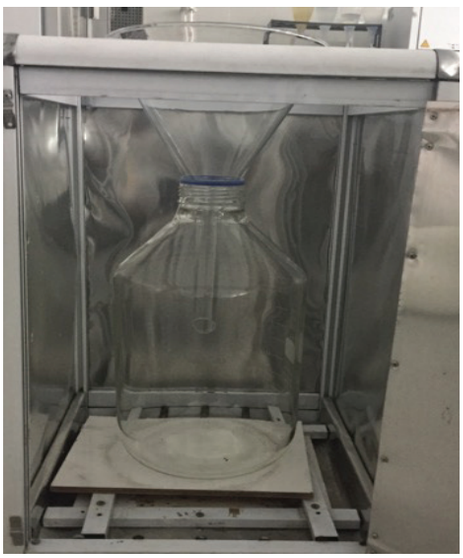

Fig. 2. The sampling devices.

Digestion protocol

The samples were digested before filtration to degrade organic matters for better stereomicroscopic observation. The extraction method was based on the protocol proposed by Ref. [22] (Fig. 3) and briefly described as follows:

Step 1: sieving the sample through a 1-mm sieve to remove big organic pieces.

Step 2: density-separating the sample, using NaCl (Merck®, 1.18±0.02 gcm^{-3}), the sample : NaCl volume ratio was 1:1.

Step 3: adding 1 g of sodium dodecyl sulfate (SDS, Merck®) to the sample and storing the sample at 50°C for 24 h.

Step 4: adding 1 ml of biozym SE (protease and amylase, Spinnrad®) and 1 ml of biozym F (lipase, Spinnrad®) to the sample and storing the sample at 40°C for 48 h.

Step 5: adding 15 ml of hydrogen peroxide (H_2O_2, Merck®) to the sample and storing the sample at 40°C for 48 h.

Step 6: filtering the sample through glass fibre filters (GF/A, Whatman®, 1.6 µm porosity), using a glassware filtration set.

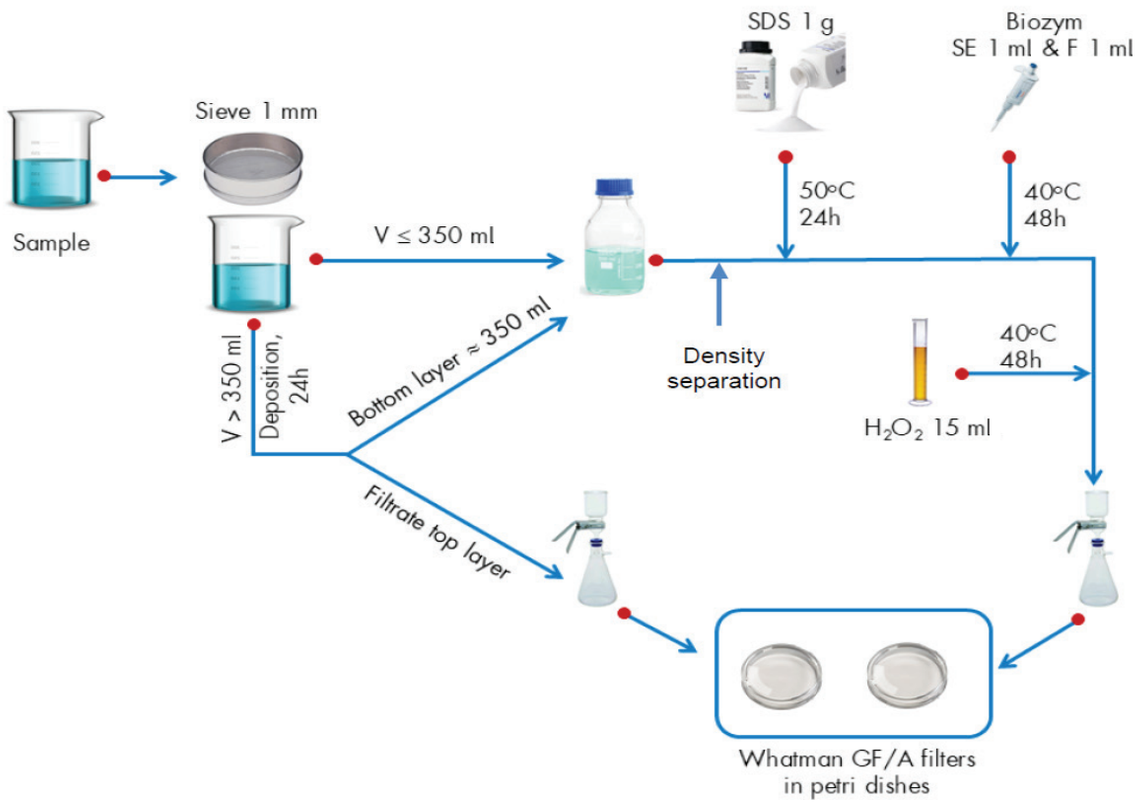

Fig. 3. Protocol for extraction of microplastic fibres from atmospheric fallout samples.

So far, MiP qualitative analyses were mostly carried out using FTIR (Fourier Transform InfraRed Spectrometry) combined with a microscope [11]. In this study, due to the unavailability of the equipment, the MiPs were defined based on the criteria proposed by Ref. [23]. The filters after the treatment period will be observed by a S6D stereomicroscope integrated with a MC170 camera and LAS software (Fig. 4) for analysing physical characteristics (quantity, shape, size, colour) of the MiPs. It is worth emphasizing that the size range of the MiPs observed in this study were 100 µm to 5 mm for the fibres' length and fragments' longest dimension.

Fig. 4. S6D stereomicroscope integrated with a MC170 camera.

Results and discussions

Microplastic occurrence

There were a total of 1,791 microplastic fibres and fragments observed from 8 samples, with fibres being more predominant than fragments (1,142 fibres or 64% compared to 649 fragments or 36%) (Fig. 5). The concentration of MiPs was calculated from the number of MiP fibres and fragments, the diameter of the sampling funnel (250 mm), and the sampling duration (Table 1, Fig. 6).

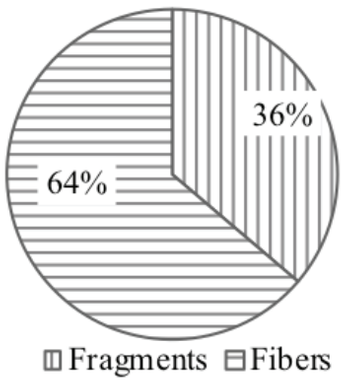

Fig. 5. Percentage of total microplastic fibres and fragments found in all samples.

The concentration of MiPs (both fibres and fragments) was 1,356.8 items $m^{-2}d^{-1}$, roughly 50 times more than what was measured in Paris, which was 2 to 355 items $m^{-2}d^{-1}$ of sizes ranging from 200 mm to 5 mm, and under the conditions of filtration without digestion step [20]. Similar to the results reported by these two sites, fibre was found to be the dominant shape initially identified by visual observation of the suspected items in the atmospheric fallout.

The concentration of the observed MiP fragments and fibres fluctuated during the sampling time, and a particularly large number of items were found during the dry season (Fig. 6). During the dry season, the average concentration of fibres found at the sampling site was 1,333.5 items $m^{-2}d^{-1}$, about 3 times more than the concentration of observed fragments, which was 467.7 items $m^{-2}d^{-1}$. During the rainy season, the concentration of MiPs did not show any significant difference, with concentrations of 515.7 and 396.8 items $m^{-2}d^{-1}$ for fragments and fibres, respectively. Besides, the concentration of MiPs in the dry season (1,801.2 items $m^{-2}d^{-1}$) was 2 times greater than in the rainy season, about 912.5 items $m^{-2}d^{-1}$ (Table 1). This indicates that there is less microplastic accumulation in the atmospheric fallout at the Phuoc Hiep landfill during rainy days, which may be due to the impact of rainfall limiting air pollutant concentrations [24]. MiP monitoring should be carried out to better understand the temporal variation of MiP concentration.

Table 1. Concentration of microplastic fibres and fragments found at Phuoc Hiep landfill.

Season	Sampling time	Sampling duration (days)	MiP counts		MiP concentration (items $m^{-2}d^{-1}$)		Average seasonal MiPs concentration (items $m^{-2}d^{-1}$)		
			Fragments	*Fibers*	*Fragments*	*Fibers*	*Fragments*	*Fibers*	*Total*
Dry	20/12/2018	4	24	129	122.2	657.0	467.7	1,333.5	1,801.2
	24/12/2018	3	27	185	183.3	1,256.3			
	03/01/2019	4	54	217	275.0	1,105.2			
	07/01/2019	3	190	341	1,290.2	2,315.6			
Rainy	16/05/2019	4	25	59	127.3	300.5	515.7	396.8	912.5
	27/05/2019	3	37	64	251.3	434.6			
	03/06/2019	4	176	86	896.4	438.0			
	06/06/2019	3	116	61	787.7	414.2			

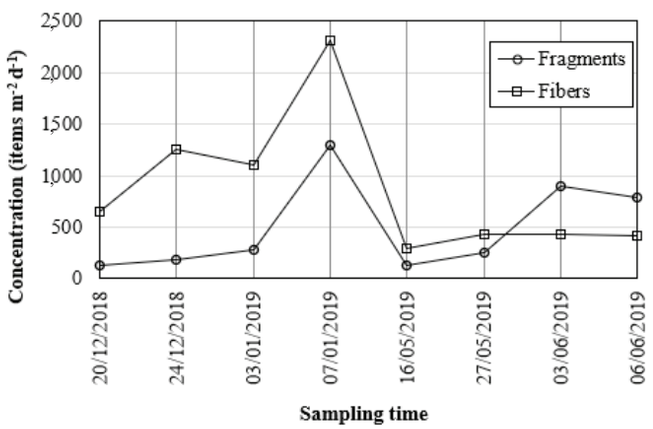

Fig. 6. Concentration of microplastic fibre and fragments concentration (items $m^{-2}d^{-1}$) with sampling time.

Physical characteristics of microplastics

Concerning the size of MiPs found at this study location, within the observation size range stated previously, i.e. 100 µm to 5 mm for fibres' length and fragments' longest dimension, most of the fibres and fragments are considered to be in the small size range (Fig. 7). As seen in Fig. 7A, the smallest fibres ranging from 100-500 µm in length were predominant at nearly 74.5% of the total fibres counted, while longer fibres were relatively rare. This result was similar to the length distribution of fibres shown by Ref. [20].

The fragments were predominant over a small surface area, with 409 fragments in the surface area range of 1,000-10,000 μm^2, which occupied 63% of the total number of fragments observed for all dry and rainy days (Fig. 7B).

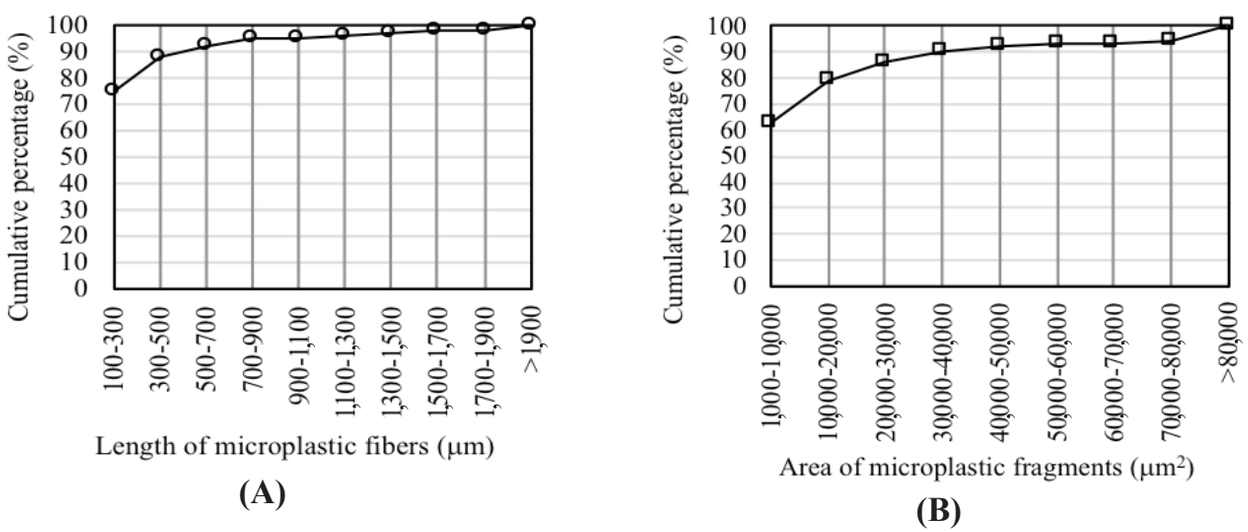

Fig. 7. Cumulative percentage of (A) length of microplastic fibres (mm) and (B) area of microplastic fragments (mm^2).

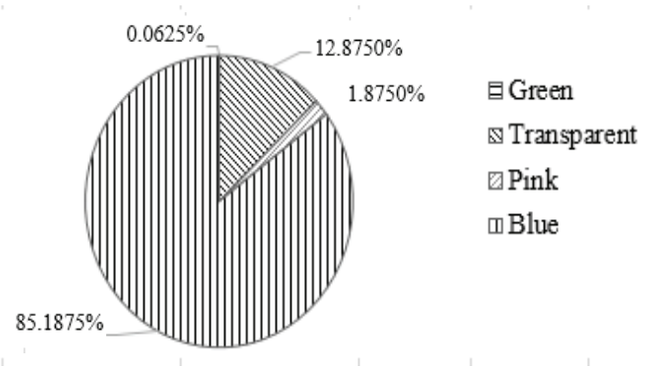

Fig. 8. Total microplastics with colours found in the atmospheric fallout collected in the Phuoc Hiep landfill.

In terms of colour, blue MiPs were the most dominant for both fibres and fragments (Fig. 8). At different sampling times, blue fibres fluctuated from 89% for the sample collected on Jan 03, 2019 to 99% for the sample collected on June 06, 2019, as seen in Fig. 9A. The other colours, in decreasing order, were pink (1 to 9%), transparent (0 to 2%), and green (0 to 1%). For fragments, the percentage of MiP colours fluctuated more in comparison to that of MiP fibres. At different sampling times, blue fragments fluctuated from 12% for the sample collected on June 6, 2019, to 100% for the sample collected on June 03, 2019, as seen in Fig. 9B. The other colours, in decreasing order, were transparent (0 to 88%) and pink (0 to 1%). There was no green colour found

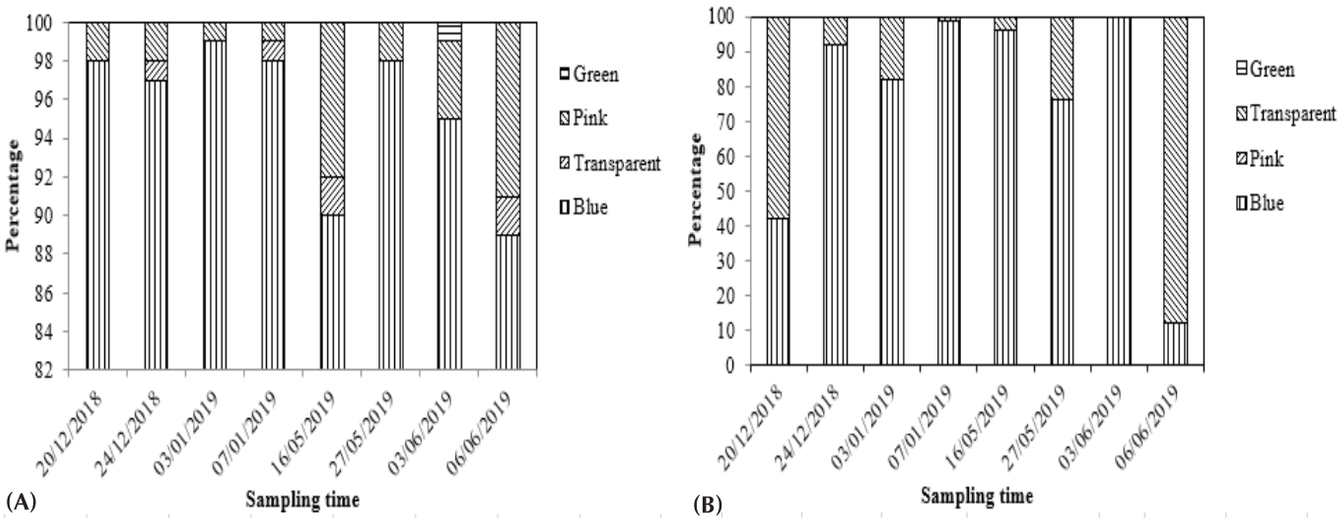

Fig. 9. Colour distribution of MiPs in the atmospheric fallout samples taken at Phuoc Hiep landfill for (A) fibres and (B) fragments.

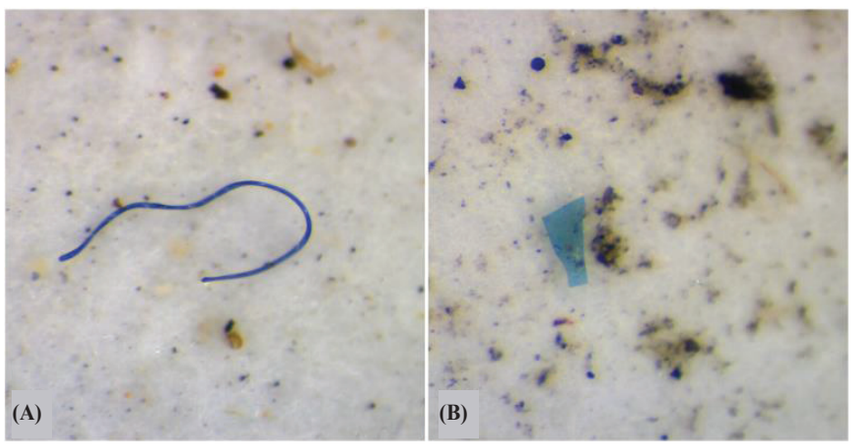

Fig. 10. An example of a microplastic (under stereomicroscope) from the sample collected at the Phuoc Hiep landfill in the form of (A) fibre and (B) fragment.

among all the samples. The microplastic fibres and fragments found in the sample collected from the Phuoc Hiep landfill under a stereomicroscope is shown in Fig. 10.

Comparing the results obtained from this study to the MiPs on the surface water of the Saigon river [16], there may be some similarities in terms of size range and colour distribution of MiPs found in the atmospheric fallout. Further study should be carried out to determine if any correlation in MiPs size and colour exists.

Conclusions

This study reported a significant amount of MiPs found in atmospheric fallout at the Phuoc Hiep landfill, Cu Chi, HCMC. In particular, the results showed that the concentration of MiPs in the atmospheric fallout at Phuoc Hiep landfill were 1,801.2 items $m^{-2}d^{-1}$ and 913 items $m^{-2}d^{-1}$ in dry and rainy seasons, respectively. Physical characteristics such as shape, colour, and size of the microplastic particles were also clarified and discussed. Future work aimed at providing more data on MiP accumulation in the atmosphere needs to be considered and implemented throughout the world. Besides, scanning electron microscope and Fourier-transform infrared spectroscopy should be carried out in further studies for surface texture and chemical composition analyses of atmospheric microplastics.

ACKNOWLEDGEMENTS

This research is funded by University of Technology, Vietnam National University, Ho Chi Minh city, under grant number To-MTTN-2018-11.

The authors declare that there is no conflict of interest regarding the publication of this article.

REFERENCES

[1] PlasticsEurope (2018), *Annual Review 2017-2018*.

[2] T. Stanton, M. Johnson, P. Nathanail, W. MacNaughtan, R.L. Gomes (2019), "Freshwater and airborne textile fibre populations are dominated by 'natural', not microplastic, fibres", *Science of The Total Environment*, **666**, pp.377-389.

[3] UNEP (2016), *Marine Plastic Debris and Microplastics - Global Lessons and Research to Inspire Action and Guide Policy change*, United Nations Environment Programme, Nairobi.

[4] N.B. Hartmann, T. Huffer, R.C. Thompson, M. Hassellov, A. Verschoor, A.E. Daugaard, S. Rist, T. Karlsson, N. Brennholt, M. Cole, M.P. Herrling, M.C. Hess, N.P. Ivleva, A.L. Lusher, M. Wagner (2019), "Are we speaking the same language? Recommendations for a definition and categorization framework for plastic debris", *Environ. Sci. Technol.*, **53**, pp.1039-1047.

[5] A. Cózar, F. Echevarría, J.I González-Gordillo, X. Irigoien, B. Úbeda, R. Dris, J. Gasperi, M. Saad, C. Mirande, B. Tassin (2016), "Synthetic fibers in atmospheric fallout: a source of microplastics in the environment?", *Mar. Pollut. Bull.*, **104**, pp.290-293.

[6] R. Sussarellu, M. Suquet, Y. Thomas, C. Lambert, C. Fabioux, M.E.J. Pernet, N. Le Goïc, V. Quillien, C. Mingant, Y. Epelboin, C. Corporeau, J. Guyomarch, J. Robbens, I. Paul-Pont, P. Soudant, A. Huvet (2016), "Oyster reproduction is affected by exposure to polystyrene microplastics", *PNAS*, **113**, pp.2430-2435.

[7] B. Ma, W. Xue, C. Hu, H. Liu, J. Qu, L. Li (2019), "Characteristics of MiPs removal via coagulation and ultrafiltration during drinking water treatment", *Chemical Engineering Journal*, **359**, pp.159-167.

[8] J.C. Prata (2018), "Airborne microplastics: consequences to human health?", *Environmental Pollution*, **234**, pp.115-126.

[9] L. Zhu, H. Wang, B. Chen, X. Sun, K. Qu & B. Xia (2019), "Microplastic ingestion in deep-sea fish from the South China sea", *Science of The Total Environment*, DOI:10.1016/j.scitotenv.2019.04.380.

[10] J. Zhao, W. Ran, J. Teng, Y. Liu, H. Liu, X. Yin, Q. Wang (2018), "Microplastic pollution in sediments from the Bohai sea and the Yellow sea, China", *Science of The Total Environment*, **640-641**, pp.637-645.

[11] R.C. Thompson, Y. Olsen, R.P. Mitchell, A. Davis, S.J. Rowland, A.W.G. John, A.E. Russell (2004), "Lost at sea: where is all the plastic?", *Science*, **304(5672)**, DOI: 10.1126/science.1094559.

[12] L.M. Rios Mendoza & M. Balcer (2018), "Microplastics in freshwater environments: a review of quantification assessment", *TrAC Trends in Analytical Chemistry*, DOI:10.1016/j.trac.2018.10.020.

[13] D. Eerkes-Medrano, R.C. Thompson, D.C Aldridge (2015), "Microplastics in freshwater systems: a review of the emerging threats, identification of knowledge gaps and prioritisation of research needs", *Water Research*, **75**, pp.63-82.

[14] A. McCormick, T.J. Hoellein, S.A. Mason, J. Schluep and J.J. Kelly (2014), "Microplastic is an abundant and distinct microbial habitat in an urban river", *Environ. Sci. Technol.*, **48**, pp.11863-11871.

[15] C.J. Moore (2008), "Synthetic polymers in the marine environment: a rapidly increasing, long-term threat", *Environ. Res.*, **108(2)**, pp.131-139.

[16] L. Lahens, E. Strady, T.C. Kieu-Le, R. Dris, K. Boukerma, E. Rinnert, J. Gaspéri, B. Tassin (2018), "Macroplastic and microplastic contamination assessment of a tropical river (Saigon river, Vietnam) transversed by a developing megacity", *Environmental Pollution*, **236**, pp.661-671.

[17] J. Gasperi, S.L. Wright, R. Dris, F. Collard, C. Mandin, M. Guerrouache, B. Tassin, et al. (2018), "Microplastics in air: are we breathing it in?", *Environmental Science & Health*, **1**, pp.1-5.

[18] R. Dris, J. Gasperi, V. Rocher, M. Saad, N. Renault, B. Tassin (2015), "Microplastic contamination in an urban area: a case study in Greater Paris", *Environmental Chemistry*, **12(5)**, pp.592-599.

[19] L. Cai, J. Wang, J. Peng, Z. Tan, Z. Zhan, X. Tan, Q. Chen (2018), "Characteristic of microplastics in the atmospheric fallout from Dongguan city, China: preliminary research and first evidence", *Environ. Sci. Pollut. Res.*, **24**, pp.24928-24935.

[20] R. Dris, J. Gasperi, C. Mirande, C. Mandin, M. Guerrouache, V. Langlois, B. Tassin (2016), "A first overview of textile fibers, including microplastics, in indoor and outdoor environments", *Environ. Pollut.*, **221**, pp.453-458.

[21] S. Allen, D. Allen, V.R. Phoenix, Le Roux, P.D. Jiménez, A. Simonneau, S. Binet, D. Galop (2019), "Atmospheric transport and deposition of microplastics in a remote mountain catchment", *Nature Geoscience*, **12**, pp.339-344.

[22] N.S. Truong Tran, T.C. Kieu Le, E. Strady, Q.V. Tran, M.T. Le Thi, Q.T. Thuong (2019), "Extraction of the anthropogenic fibers in the atmospheric fallout in Ho Chi Minh city", *Journal of Science*, **16**, pp.17-24.

[23] F. Norén (2007), *Small Plastic Particles in Coastal Swedish Waters*, http://www.kimointernational.org/WebData/Files/Small%20plastic%20particles%20in%20Swedish%20West%20Coast%20Waters.pdf [Verified 14 April 2015].

[24] H-Y. Kwak, J. Ko, S. Lee, C-H. Joh (2017), "Identifying the correlation between rainfall, traffic flow performance and air pollution concentration in Seoul using a path analysis", *Transportation Research Procedia*, **25**, pp.3552-3563.

DOI: 10.31276/VJSTE.62(3).90-96

A study on the effects of sea level rise on mangrove ecosystem in Giao Thuy district, Nam Dinh province

Van Doanh Vu*, Hong Tinh Pham, Thi Thu Trang Bui

Hanoi University of Natural Resources and Environment

Received 16 January 2020; accepted 10 April 2020

Abstract:

Climate change and sea level rise (SLR) have greatly affected the coastal land use of the Nam Dinh province. It has especially impacted the mangrove forests in coastal plain areas. According to the monitoring data from management units, saline intrusion due to SLR tends to expand in scope, affecting and reducing the area of mangrove ecosystems. From this situation, it can be seen that the impact assessment and estimation of economic loss in coastal provinces such as Nam Dinh is incredibly necessary to help the localities proactively respond to climate change and SLR, which is in line with the national target program on climate change. This research, which uses methods of evaluating economic values, aims to quantitatively assess the extent of damage caused by SLR on an area of mangrove forests in Giao Thuy district, Nam Dinh province. The valuation of these impacts will provide a basis for scientists, research institutions, and localities to proactively mitigate and adapt to climate change. Research results show the damage of climate change and SLR to the coastal mangrove forests in Giao Thuy and the risk to agricultural land use in the Nghia Hung and Hai Hau districts. These results also provide warning of the potential damage caused by SLR to dike and irrigation systems in the coastal districts of the Nam Dinh province, which follow Xuan Truong, Giao Thuy, Hai Hau, and Nghia Hung.

Keywords: **climate change, mangrove ecosystem, SLR.**

Classification number: **5.2**

Introduction

Currently, the mangrove forests in the Giao Thuy district and Nam Dinh province are known for their direct use values such as firewood supply, forest products, marine fishing, and beekeeping for honey, medicinal plants, and ornamental creatures, etc. Their indirect use values include supporting aquaculture activities, carbon accumulation (CO_2), and the prevention and mitigation of natural disasters. Some non-use values are those related to biodiversity. However, these values will no longer be available if the mangrove area is reduced. In recent years, along with the increase in temperature, extreme climates and extreme phenomena have caused a marked increase in the heat from the sun, very cold and damaging weather, heavy rain, and storms in the Nam Dinh province. Together with SLR and saline intrusion, a great impact on the inhabited area and quality of the mangrove forests in the coastal areas of Nam Dinh province, especially in the Giao Thuy district, are occurring.

In coastal plain areas such as the Nam Dinh province, SLR has a great influence on coastal land use. This is especially true for agricultural land, among which mangroves are one of the groups most sensitive to the impact of climate change and SLR. In 2013, the area of inundated land in the province was 34,020 ha and was mostly concentrated in the coastal districts of Nghia Hung, Giao Thuy, and Hai Hau (Institute of Environmental Hydrology and Climate Change, 2013) [1]. According to the estimates from the Ministry of Natural Resources and Environment - MONRE (2016), if the SLR is 100 cm, over 60% of the coastal districts such as Hai Hau, Giao Thuy, and Nghia Hung in the Nam Dinh province are at risk of flooding [2]. Saline intrusion tends to expand its influence in terms of scope. According to the actual measurement data from the Centre for Environmental Resources Monitoring and Analysis, Nam Dinh Department of Natural Resources and Environment, on December 21st 2014, the salinity of the Red river measured at the mouth of Tai sluice gate in the Xuan Tan commune, Xuan Truong

*Corresponding author: Email: doanh2002vn@gmail.com

(19 km from the sea) was 2.6‰. The salinity in the Ninh Co river, at Tan Ly wharf, Nghia Son commune, Nghia Hung (20 km from the sea) was 3‰ and in the Day river, at boat wharf 10, Nghia Son commune, Nghia Hung (28 km from the sea) was 0.2‰ [1].

A geological study by Miyagi (1998) shows that habitat change in the mangroves depends on the rate of change of SLR. When the rate of SLR is greater than the limit of the peat accumulation rate, mangroves will be submerged in seawater and will die [3]. Research by Thi Kim Cuc Nguyen, et al. (2012) [4] and Gilman, et al. (2007) [5] also show that depending on regional topographic conditions and the degree of change in water level, mangroves may decline or expand.

Recently, when the Warsaw International Mechanism for Loss and Damage associated with Climate Change Impacts was established in 2013 and the Paris Agreement on Climate Change was adopted in 2015, the impact of climate change and SLR on coastal and mangrove forest areas have been increasingly studied both in Viet Nam and around the world.

In order to quantitatively assess the extent of SLR damage to mangroves, this study focuses on calculating the economic losses of mangrove forests caused by SLR in Giao Thuy district, Nam Dinh province in 2020, 2030, 2040, and 2050 corresponding to SLRs of 12, 18, 24, and 32 cm (RCP6.0 scenario) based on the map of "Nam Dinh land use planning till 2020" [2]. These research results will provide a basis for researchers, organizations, and localities to take a proactive and appropriate response concerning forest protection measures in the context of climate change.

Study data and methods

Data

Secondary data collection: this research used the data and documents from the 2010-2016 Nam Dinh Statistical Yearbook from the General Statistics Office, the 2016 scenario of climate change and SLR for Vietnam (MONRE), and related studies on the economic value of the affected subjects.

Primary data: data and documents (on affected areas of mangrove forests, damage levels, etc.) are obtained from field surveys, community consultations, and expert consultations with the use of the Delphi method.

Study methods

Field survey and community consultation: in order to support the assessment of SLR impacts on mangroves, the research team conducted a field survey to adjust the SLR impact map of the Giao Thuy district. At the same time, questionnaires for field survey and community consultation were developed, which involved households participating in livelihood activities related to planting and harvesting mangrove forests.

Delphi method: in order to determine mangroves' use value groups that are likely to be affected by SLR and to select the level of damage, the Delphi method was applied with two rounds to consult experts who are officers of state management agencies at all levels and scientists and experts from agencies such as managers of the Department of Agriculture and Rural Development; Department of Natural Resources and Environment of Nam Dinh and Division of Agriculture and Rural Development of Giao Thuy district, Nam Dinh province; lecturers at Hanoi University of Natural Resources and Environment, and experts from the Institute of Meteorology, Hydrology and Climate Change.

Method of SLR impact mapping: in this study, the research team inherited the method of developing flooding risk maps according to climate change and SLR scenarios for Vietnam by MONRE (2016) to map the impact of SLR on the Giao Thuy district in 2050. The map was also adjusted according to the field survey findings. Because only the map of "Land Use Planning to 2020" is of the most practical significance, this study assumes that land use in the Nam Dinh province would follow the Land Use Planning and Land Use Status in 2050, which doesn't show much change compared to 2020. Therefore, the land use status in 2050 in the Nam Dinh province in this calculation is determined according to "Land use planning for Nam Dinh province until 2020" [6] combined with field survey data.

In the context of increasing SLR and saline intrusion in coastal districts of Nam Dinh province and in order to make a plan for medium and long-term SLRs, our study selected the 2050 SLR scenario of 32 cm for Nam Dinh province corresponding to the high average scenario RCP6.0 to determine the area of affected mangroves.

Method of valuation of economic values: using statistics yearbook data, research works related to the affected subjects to estimate the average value in 2010 of the specific subjects is given in Table 1. The total economic value (TEV) formula by Bolt [7] (2005), Pearce (1990), and Barbier's, et al. methodologies [8] for calculating losses due to SLR were used.

Table 1. Method of valuing economic values of mangroves

Affected subjects	Valuation method	Used data
Direct use values		
Mangrove area with ecotourism value	Travel Cost Method - TCM	Findings in the thesis of Dinh Duc Truong (2010) "Assessing the economic value for wetland management - applied in the wetlands of Ba Lat river mouth, Nam Dinh province" show the value was determined to be 2.4 billion VND/year [9].
Mangrove area with value of bee-keeping for honey	Market price method	Study findings of Dinh Duc Truong (2010): 0.6 million VND/ha/ year [9].
Indirect use value		
Mangrove area with value of ecological support for aquaculture activities	Use production function model (Cobb-Douglas function) to determine the optimal effectiveness of the objective function.	Study findings of Dinh Duc Truong: 16.5 million/ha/year [9].
Mangrove area with value of carbon accumulation/absorption	Use market price method	Research by Tateda (2005), in which the estimation of carbon absorption value of mangroves was carried out in some mangrove areas of Southeast Asia including Xuan Thuy area showed a cumulative capacity of 2.5 tons/ha/year of the mangroves in this area [10].
Mangrove area with value of natural disaster impact mitigation (storms, SLR)	Use method of Avoided Cost - AC	Results of the "Study on seadyke protection value of mangrove forest in Xuan Thuy - Nam Dinh" by Tan Phuong Vu, Thi Thu Ha Tran: the value of mangroves in impact mitigation is estimated to be 633,000 VND/ha/year for seadyke repair and maintenance [11].
Non-use values		
The loss of mangrove area results in non-use values such as biodiversity conservation	Use Contingent Valuation Method - CVM	The results from the thesis "Assessing the economic value for wetland management - applied in the wetlands of Ba Lat river mouth, Nam Dinh province" Giao Thuy district: the value is 399 million VND/year [9].

Study results

Process for valuation of economic losses of mangroves due to climate change and SLR

A database has been built, expert opinions have been collected, and field surveys and community consultations have been conducted to develop a process of assessing the economic losses of mangrove forests under the impacts of climate change and SLR. There are seven main steps shown in Fig. 1 and outlined below [12]:

(1) Select an appropriate SLR scenario

(2) Develop flood risk maps according to different SLRs under the scenario

(3) Develop a map of climate change and SLR impacts on mangrove forests

(4) Adjust the map of climate change and SLR impacts on mangrove forests

(5) Determine the area of affected mangroves and the use values of mangroves

(6) Calculate and determine the damage value of mangroves

(7) Demonstrate damage assessment results on the map of climate change and SLR impacts.

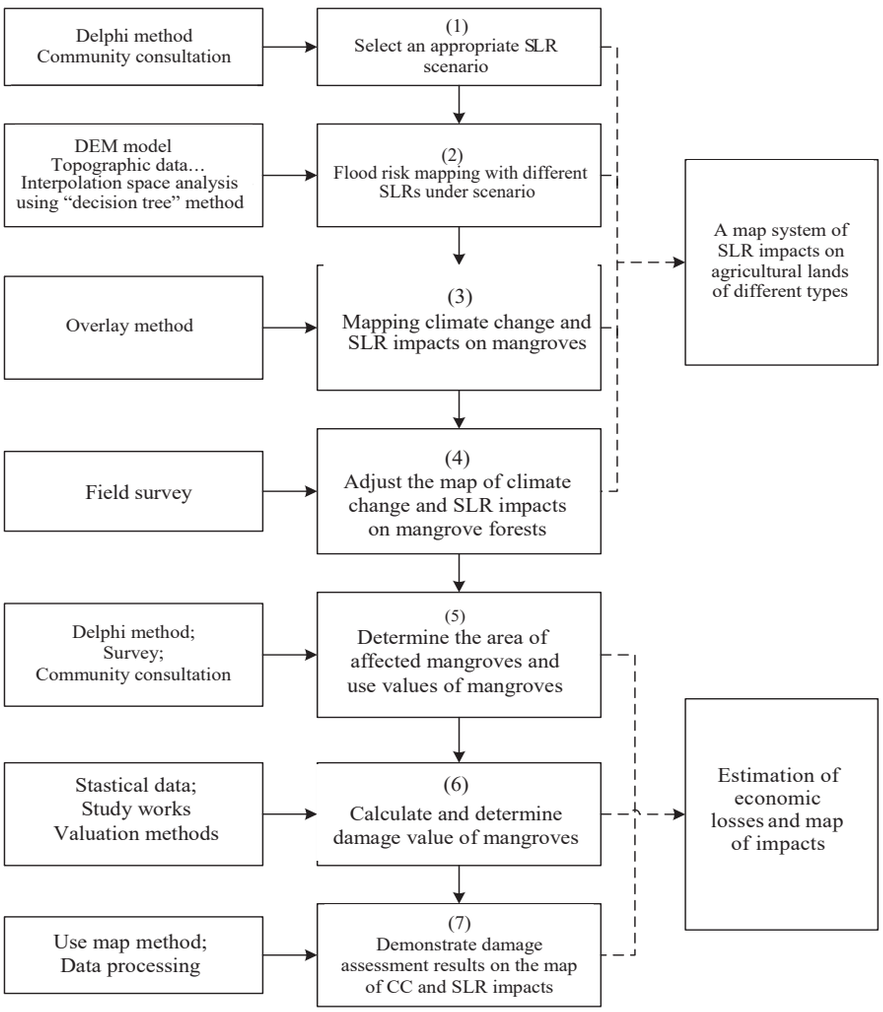

Fig. 1. Study process of economic loss valuation of mangroves under the impacts of climate change and SLR.

Building the map of climate change and SLR impacts on mangrove forests

Using the map "Land use planning for Nam Dinh province to 2020" along with the timelines for calculation under the flood risk scenario of SLRs, the research team built a map of flood risk impact on mangrove forests due to climate change and SLRs for the Giao Thuy district.

The map of the SLR-induced flood risk impact on mangroves based on the map "Nam Dinh land use planning to 2020" for years with corresponding SLRs of 12, 18, 24, and 32 cm (2020-2050) was used to map the flood risk impacts caused by SLRs on mangroves in Giao Thuy district. The area of mangroves affected by SLRs is shown in Table 1.

There are two typical maps below based on the "Land use planning till 2020" map for the year 2030 (Fig. 2) and 2050 (Fig. 3) with the affected mangrove forest area.

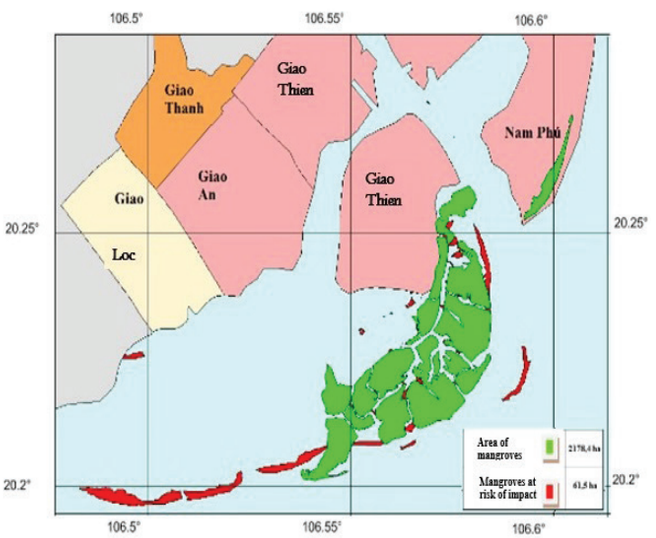

Fig. 2. Predicted mangrove area change in Ba Lat river mouth, Giao Thuy district under the impact of climate change in 2030.

From the forecast map of the affected mangrove ecosystem at Ba Lat mouth, Giao Thuy district, the change in the area of mangroves has been determined as shown in Table 2.

Table 2. Area of mangroves affected by climate change and SLR in Giao Thuy from 2020 to 2050 according to the map of land use planning 2020.

Mangroves at risk of impact	Map based total area of mangroves (ha)	Mangrove area affected by SLR over time (ha)			
		2020 (12 cm)	*2030* (18 cm)	*2040* (24 cm)	*2050* (32 cm)
Based on the planning map 2020	2,178.4	22.1	61.5	104.1	176.1

Table 2 lists the area of mangroves affected by SLR in the Giao Thuy district from 2020-2050 (based on the map titled "Nam Dinh land use planning to 2020"). Also shown in Table 2 is the gradual increase in the total area of mangroves affected by SLR from 2020 to 2050, ranging from 1.3% to 9.3% of the district's natural land area.

Fig. 2 shows the map of the SLR impacts on the use of agricultural land in 2030 with an inundation level of 18 cm according to map "Nam Dinh land use planning to 2020". Figure 3 shows the map of the mangrove area in Xuan Thuy area at risk of impact in 2050 with a SLR of 32 cm.

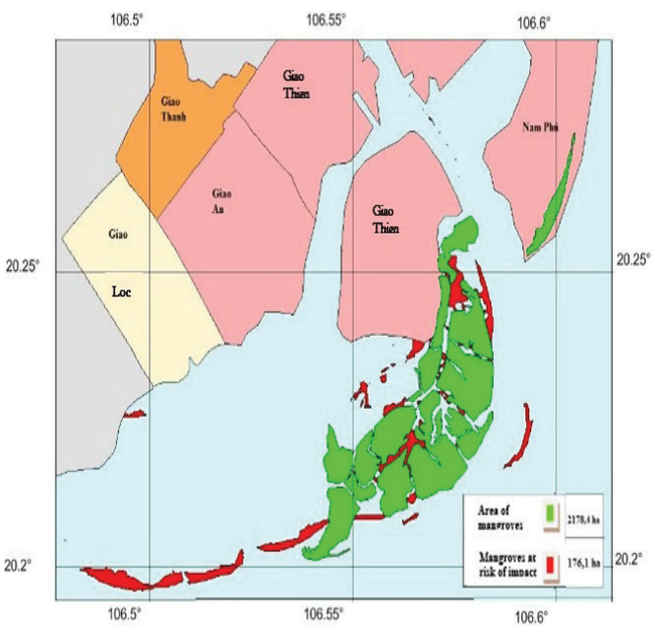

Fig. 3. Mangrove area in Ba Lat mouth, Giao Thuy district affected by climate change in 2050.

Valuation of economic losses of mangroves in Giao Thuy district

The establishment of the formula for calculating economic losses of mangroves in Giao Thuy district, Nam Dinh province is based on the formula system of Bolt (2005) and Pearce (1990). From the process shown in Fig. 1, the following equation, Eq. (1), was developed to evaluate economic losses of the studied mangroves caused by climate change and SLR:

$$TEV = UV + NUV = DUV + IUV + OV + EV + BV \quad (1)$$

where TEV is the total economic value; UV is the use value; NUV is the non-use value; DUV is the direct use value; IUV is the indirect use value; OV is the option value; EV is the existence value; and BV is the bequest value. Further, DUV = $(\sum Q_i \times P_i)$/year, where Q_i is annual average quantity of product *i* and P_i is the price of product *i*, and IUV = (∑replacement cost)/year = (∑preventive cost)/year = (∑travel cost)/year.

The formula system for valuation from Barbier [1] was used as well.

The level of loss, K, according to joint Circular No 43/2015/TTLT- BNNPTNT-BKHDT, was determined using the same expert method for the period of 2020-2040 and 2040-2050:

$$TH_{RNM} = \sum(S \times G) \times K \quad (2)$$

where TH_{RNM} is the economic loss of mangrove caused by SLR in one area; S is the area of mangroves affected by climate change and SLR; G is the mean economic value of one area unit of mangroves; and K is the level of loss.

Applying Eq. (2):

- S: was determined based on the impact map, Table 2, and especially the study of the map "Land use planning till 2020".

- G: was calculated by processing the data collected from statistic yearbooks and research works published in Nam Dinh, as shown in Table 3.

The survey method was used to determine the average economic value of the subjects that are affected by climate

change and SLR. Collected data regarding the temperature, rainfall, humidity, etc, according to the Nam Dinh statistical yearbook was used, and reference to the valuation works related to the affected subjects including group of wetlands, dike systems, and salt prevention facilities.

The selection of the discount factor (r) that makes the value similar to that of 2010 was carefully considered because in Vietnam the comparative price is a statistic that is widely used to estimate the average economic value of the mangrove forest.

Based on community and expert consultation results combined with the Delphi method with 2 rounds to identify those affected by SLR, the study has identified the losses due to SLR with the use value of mangrove forests as follows:

Table 3. Average economic value of mangroves affected by climate change and SLR in Giao Thuy district.

Affected subjects	Economic value loss according to the price of 2010 (million VND)
Loss in mangrove area with direct, indirect use and non-use values	+ Ecotourism: 2.4 billion VND/year=2,400 (million/ha) + Bee keeping for honey: 0.6 million VND/ha/year + Ecological support for aquaculture activities: 16.51 million VND/year (at the time of the year 2008)→ converted equivalent to the price of 2010: $16.51x(1+0.08)^2 = 19.3$ million/ha + carbon absorption/accumulation: 2.5 tons/ha/year→ equivalent to: 2.5x5x20,000=250,000 VND/ha/year= 0.25 million/ha + Natural disaster impact mitigation (storms, SLR): 633,000 VND/ha/year = 0.633 million/ha + Biodiversity conservation: 399 million VND/ha/year => Total value: 2,400+0.6+19.3 +0.25+0.633+399=2,819.7 (million VND)

- K: estimated following Circular 43 and Delphi method with different levels of loss [13].

+ Mangrove ecosystem loss in the phase 2020-2040: K = 0.2

+ Mangrove ecosystem loss in the phase 2040-2050: K = 0.4

Based on the area of agricultural land affected by SLR on maps of land use such as the map of planning to 2020, from Table 2, it can be seen that there is an increased risk to the mangrove forest area in the Giao Thuy district being affected by climate change and SLR. For instance, in 2020, at an inundation level of 12 cm, the flooded area will be about 22.1 ha. In 2050, the respective figures will be 32 cm and 176.1 ha. Table 4 is formed based on the Eq. (2) above and Table 2 on the area of mangroves affected by climate change and SLR. Table 3 is formed based on the average economic value of the mangrove forests in the Giao Thuy district. Table 4 shows economic loss of the mangroves in the Giao Thuy district due to the impacts of climate change and SLR from 2020 to 2050 according to different land use approaches.

The results show that the affected mangrove forest area will be proportional to the economic losses and both will continuously increase from 2020 to 2050. With the two coefficients of K in the period 2020-2030 and 2040-2050 being 0.2 and 0.4, respectively, the results are as follows:

With the approach of no-intervention, if land use is as planned in the 2020 planning map, and if the SLR is 12 cm, the economic loss value in 2020 will be 12,463.1 million VND, increasing to 34,682.3 million VND in 2030 and the maximum value of losses in 2050 will be 198,619.7 million VND, equivalent to 176.1 ha of forest lost when the SLRs to 32 cm.

Table 4. Economic loss of mangroves in Giao Thuy district under impacts of climate change and SLR from 2020 to 2050.

Mangroves in Xuan Thuy affected by climate change and SLR	Mangrove area (S) affected by SLR over time (ha)				Average value (G) per 1 ha (million VND comparative price of 2010)	Loss level K		Estimated economic loss over years (million VND)			
	2020	*2030*	*2040*	*2050*				*2020*	*2030*	*2040*	*2050*
	(12 cm)	*(18 cm)*	*(24 cm)*	*(32 cm)*							
Based on planning map of 2020	22.1	61.5	104.1	176.1	2,819.7	0.2	0.4	12,463.1	34,682.3	117,412.3	198,619.7

Source: Land use planning for Nam Dinh province till 2020.

Conclusions

This study has assessed the economic loss of mangrove forests due to SLR in the Giao Thuy district, Nam Dinh province, from 2020 to 2050. The results show that the impacts of SLR on the mangroves is increasing over time, even with no human intervention.

In addition to the assessment of the damage of climate change and SLR in the Giao Thuy district, this study also showed the risk of impacts on agricultural land use in Nghia Hung and Hai Hau, which are also coastal districts of Nam Dinh province.

This study's results also warns of the damage of SLR to dike systems and irrigation systems in the coastal districts including Xuan Truong, Giao Thuy, Hai Hau, and Nghia Hung.

Valuation of economic loss caused by climate change and SLR in the mangrove area in the Giao Thuy district of Nam Dinh is aimed to limit the damage of SLR. The locality should assign importance to the maintenance and restoration of the coastal mangrove forests, especially in Xuan Thuy National Park. The district also needs to pay attention to the spontaneous conversion of the aquaculture model to limit the impacts on mangrove forests. There should be projects and research topics on conservation and development of mangroves, with sustainable models of aquaculture combined with mangrove planting or new planting and supplementary planting in the areas where mangrove forests are being degraded.

The authors declare that there is no conflict of interest regarding the publication of this article.

REFERENCES

[1] Institute of Hydrology, Environment and Climate Change (2013), *Report on Irrigation Planning of Nam Dinh Province till 2020.*

[2] MONRE (2016), *Climate Change and SLR Scenario for Vietnam.*

[3] T.E. Miyagi (1998), *Mangrove Habitat Dynamics and Sea-Level Change,* Tohoku University.

[4] Thi Kim Cuc Nguyen, Van Dat Tran (2012), "Study the adaptability of the coastal mangrove ecosystem under the impact of SLR in the Red river delta", *Science and Technology Magazine of Irrigation and Environment*, **37**, pp.45-52.

[5] Gilman Eric, Joanna Ellison, Richard Coleman (2007), *Assessment of Mangrove Response to Projected Relative Sea-Level Rise and Recent Historical Reconstruction of Shoreline Position.*

[6] People's Committee of Nam Dinh Province (2009), *Synthesis Report on Socio-Economic Development Master Plan of Nam Dinh Province till 2020.*

[7] Bolt Katherine, Giovanni Ruta, Maria Sarraf (2005), *Estimating the Cost of Environmental Degradation: a Training Manual in English, French and Arabic*, Report Nº 106 Environmental Department Papers, Environmental Economic Series, World Bank, Washington.

[8] E.B. Barbier, M. Acreman and D. Knowler (1997), *Economic Valuation of Wetlands: a Guide for Policy Market and Planners*.

[9] Duc Truong Dinh (2010), *Evaluation of Economic Value for Wetland Management - Applied in the Wetlands of Ba Lat River, Nam Dinh Province*, Doctoral dissertation.

[10] Y. Tateda (2005), "Estimation of CO_2 sequenstration rate by mangrove ecosystems", *CRIEFP News*, **361**, pp.1-3.

[11] Tan Phuong Vu, Thi Thu Ha Tran (2009), "Study on the sea dykes protection value of mangrove forests in Xuan Thuy - Nam Dinh", *Magazine of Agriculture and Rural Development*, **17**, pp.68-70.

[12] Van Doanh Vu, Ha Phong Doan, Quyet Thang Vu (2016), "Research on methods of assessing the impacts of SLR in some coastal districts in Nam Dinh province", *Magazine of Natural Resources and Environment*, **10(240)**, pp.19-22.

[13] Ministry of Agriculture and Rural Development, Ministry of Planning and Investment (2015), *Circular 43/2015/TTLT-BNNPTNT-BKHDT Joint Circular Guiding the Statistical Analysis and Assessment of Damages Caused by Natural Disasters.*

Vietnam Journal of Science, Technology and Engineering (VJSTE): Manuscript Template

General Instructions on using this template and submitting a manuscript to VJSTE: Thank you for preparing a manuscript for submission to VJSTE. Using this template, or following the guidelines below, will help us in processing your paper. Our goal is to be able to identify each section of your manuscript so that we can accurately record the title, authors, abstract, etc. and also be able to enrich it by including reference links and an accurate layout.

You can submit your paper at http://vietnamscience.vn

So that we can identify the parts of your paper, and even if you do not use our template, please begin each section with the specific key words listed below. Please do not use paragraph breaks in the title, author list, or abstract.

Title

Authors

Affiliations

Abstract

One Sentence Summary

Main Text

Acknowledgements

References

Several of these headings are optional, for example, not all papers will include a one-sentence summary, figures or tables.

Please use the .docx format (all version after Word 2007).

More specific formatting instructions are provided in the actual template, which follows.

Title: How to Format a Science Paper (replace with your real title)

Authors: The author list should be one single paragraph (no breaks). Authors should be listed by first name or initial followed by last name and separated by commas. Use superscript numbers to link affiliations, and symbols *†‡ for author notes. For example, X. Jones[1]*, P. Smith[1,2]

Affiliations:

[1]Affiliations should be preceded by superscript numbers corresponding to the author list, and each affiliation should end with a period.

[2]Each affiliation should be a separate paragraph.

*Correspondence to: include the email addresses or telephone number of the corresponding author(s). Please use the asterisk (*) symbol for the corresponding author information.

Abstract: The abstract should be about 100-150 words, and organized in this structure: An opening sentence that sets the question that you address and is comprehensible to the general reader, background content specific to this study, results, and a concluding sentence. It should be one paragraph only.

One Sentence Summary: A brief summary of the main result of your paper, without excessive jargon and less than 150 characters.

Main Text: In general, this should include a brief (1-2 paragraph) introduction, followed by a statement of the specific scope of the study, followed by results and then interpretations. Please avoid statements of future work or claims of priority, and avoid repeating the conclusions at the end.

All of the Figures and Tables should be cited in order (which should be cited as, for example, figure S1, and table S1). You can include page breaks if you would like to place the figures within the text.

Subheads: These can be included in Research Articles or Reviews and should be brief.

Equations can be included. We do not recommend using the native Word 2007, 2008, 2010 or 2011 equation editor. This can in some cases produce less reliable MathML, the online markup language we use, which may result in display errors. Instead, use the legacy equation editor in word (Insert menu; select insert object; select word equation) or use Mathtype (recommended). If you enter equations in simple LaTeX, check that they will convert accurately (Word 2007 and higher can convert simple LaTeX equations).

Fig. #: (Begin each figure caption with a label, "**Fig. 1.**" for example, as a new paragraph.).

Fig. 1. The figure caption should begin with an overall descriptive statement of the figure followed by additional text. They should be immediately after each figure. Figure parts are indicated with capital letters (**A**). If you prefer, you can place both the actual figures and captions logically through the text near where they are cited rather than at the end of the file (but not both). If a paragraph in the main text begins with the name of a figure, write out "Figure" in full (e.g., <para>"Figure 1 shows….").

Fig. 2. You can place graphics above each equation as part of this file.

Table #: (Begin each table caption with a label "**Table 1.**", etc.) as a new paragraph.

Table 1. Start this caption with a short description of your table. Format tables using the Word Table commands and structures. Do not create tables using spaces or tabs characters.

Acknowledgments: The acknowledgments should include a statement about where the data reported in the paper are presented, archived, or available. If in an archive, include the accession number or a placeholder for it. Please also include relevant funding information such as grant numbers and funding agencies. You can also include a statement of author contributions here. The acknowledgements can be multiple paragraphs.

References:

References should be cited in bracket with a number [1]. Multiple reference citations are separated by commas [2, 3] or if a series, dashes [4-6].

References are listed in numerical order, and in the same order in which they are cited in text. The reference list should include all and only those references you have cited in the text. The reference list appears at the end of the paper.

Please include the above heading "References".

Please do not mix in references with explanatory notes.

The reference consist of: Family name(s) and initials of all authors (year of publication), "Titles of journal articles" (optional), *Title of journal, book or other publication*, **volume(number)**, page numbers.

Example of a reference list:

[1] T. Binzoni, T.S. Leung, D. Boggett, D.T. Delpy (2002), "A new near infrared laser-Doppler flowmeter for deep tissue perfusion monitoring", *MAGMA*, **14,** pp.74-75.

[2] T. Binzoni, T.S. Leung, D. Boggett, D.T. Delpy (2003), "Non-invasive laser Doppler perfusion measurements of large tissue volumes and human skeletal muscle blood RMS velocity", *Phys. Med. Biol.*, **48(1)**, pp.2527-2549.

ISSN 2525-2461

Vietnam Journal of Science, Technology and Engineering

SEPTEMBER 2020 • VOLUME 62 NUMBER 3

EDITORIAL OFFICE

113 Tran Duy Hung Str., Cau Giay Dist., Hanoi

Tel: (84.24) 39436793; Fax: (84.24) 39436794

Email: khcnvn@most.gov.vn

Website: vietnamscience.vn

PUBLICATION LICENCE

No.1153/GP-BTTTT 26th July 2011

No.2528/GP-BTTTT 26th December 2012

No.592/GP-BTTTT 28th December 2016